

POLITECNICO DI TORINO

Corso di Laurea Magistrale
in Ingegneria Aerospaziale

Tesi di Laurea Magistrale

Development of a load module for prognostics of electromechanical actuators



Relatori

prof. Matteo Davide Lorenzo Dalla Vedova

prof. Paolo Maggiore

ing. Pier Carlo Berri

ing. Alessandro Aimasso

Candidato

Michele Drivio

Anno Accademico 2021-2022

Abstract

The objective of this thesis is the realisation of a load module to be integrated with the actuation module and the braking module already present on a test bench, previously realised by the Politecnico di Torino. The test bench reproduces the operation of an electromechanical servomechanism, typically used to move secondary control surfaces, and it is this type of control surface that will be simulated. The load module must reproduce an external load at the end of the transmission of the electromechanical actuator to which the control surface is subjected. A typical example of a reproduced load is the aerodynamic forces that hinder the movement of the surface during flight. A system of pulleys, ropes and springs has been designed, specially realised through design in the Solidworks environment and production by means of the technique must Fused Deposition Modelling (FDM) of the components. The system designed in this way applies a torque to the gearbox of the brushless motor installed on the test bench through the spring recall forces. The operation of the load module was verified through a series of step tests, from which it can be seen that the torque generated by the two springs is proportional to the rotation of the gearbox. Subsequently, the gearbox was sensed through optical fibre sensors with FBG Bragg gratings in order to verify its function for prognostic analysis by comparing their response to the load induced by the load module with the strain readings from the strain gauges installed in the proximity of the FBG Bragg gratings.

Contents

List of Figures	5
List of Tables	9
1 Introduction	10
1.1 Flight controls System	11
1.1.1 Primary Flight Controls	13
1.1.2 Secondary Flight Controls	14
1.2 Servomechanisms	15
1.2.1 Hydromechanical Servomechanisms	15
1.2.2 Electrohydraulic Servomechanisms	16
1.2.3 Electrohydrostatic Servomechanisms	19
1.2.4 Electromechanical Servomechanisms	21
1.3 Prognostic and Health Management (PHM)	23
2 Test bench	25
2.1 Actuation module	26
2.1.1 Motor PMSM	26
2.1.2 Power Module	30
2.1.3 Control Unit	31
2.1.4 Microbox PC	32
2.1.5 Convertitor	33
2.1.6 Planetary Gearbox	33
2.1.7 Encoder	35
2.2 Brake module	37

2.3	Transmission System	39
2.4	Test Bench Overview	41
3	Load module	43
3.1	Gearbox guide	44
3.2	Pulley system	45
3.3	Mover	48
3.4	Acquisition system	51
3.5	Complete test bench Overview	53
4	Springs	56
4.1	Design	57
4.1.1	Force applied by single spring	57
4.1.2	Maximum elongation	57
4.1.3	Spring stiffness	58
4.1.4	Material	58
4.1.5	Geometric characteristics	59
5	Optical fibre sensors	65
5.1	Structure	66
5.2	Fiber Bragg Grating FBG	70
5.3	Photo-Thermal-Elastic Equation	71
5.4	Interrogator	73
6	Optical fibre installation	76
6.1	Choice of installation point	76
6.2	Installation procedure for optical fibres	77
6.3	Installation problems	82
7	Strain gauge installation	83
7.1	Structure of the strain gauge	83
7.2	Strain gauge operation	84
7.2.1	Strain-to-resistance relationship	84
7.2.2	Electrical resistance voltage relationship	85
7.2.3	Gage factor	86

7.3	Installation procedure for strain gauges	86
8	Trials carried out	89
8.1	Load module validation tests	89
8.2	Tests for the evaluation of optical fibres	90
8.3	Procedure for performing tests	91
8.3.1	Preparation of the test bench	92
8.3.2	Data Acquisition	93
8.4	Programmes used for testing	94
8.4.1	SmatSoft	94
8.4.2	Matlab & Arduino	95
8.4.3	Catman	95
9	Load module validation	96
9.1	Recall forces	96
9.2	Applied torque	98
9.3	Comparison of different test series	100
9.4	Linearisation and evaluation of relative error	101
10	Evaluation of FBG as prognostic sensors	104
10.1	Optical fibre and strain gauge response to step command	104
10.1.1	Optical fibre	105
10.1.2	Strain gauges	106
10.2	Synchronisation	107
10.3	Deformation-wavelength relationship	109
10.3.1	Sensors in position 1 and 4	110
10.3.2	Sensors in position 2 and 3	111
10.4	Deformation reconstruction with FBG	113
10.4.1	Pearson correlation	114
11	Driven current detection	117
12	Future analyses	120

A CAD	123
A.1 Pulley system components	123
A.2 Mover components	125
B Load module test	127
B.1 Second series of tests	127
B.2 Third series of tests	128
C FBG and SG test	131
C.1 30 deg intensity step control	131
C.2 40 deg intensity step control	133
C.3 50 deg intensity step control	134
C.4 70 deg intensity step control	136
C.5 80 deg intensity step control	137

List of Figures

1.1	Response to impulsive disturbance	12
1.2	Control surfaces of a conventional aircraft	12
1.3	Schematisation of a hydromechanical servomechanism	15
1.4	Electrohydraulic Servomechanisms scheme [15]	16
1.5	Flapper nozzle valve	17
1.6	Jet pipe valve	18
1.7	DDV valve	19
1.8	Electrohydrostatic Servomechanisms scheme [15]	20
1.9	Electromechanical Servomechanisms scheme	21
1.10	Electromechanical Servomechanisms classification	22
1.11	Prognostic and Health Management scheme [5]	23
2.1	Photo of the test bench	25
2.2	SIMOTICS S 1FK7060-2AC71-1CG0 [16]	27
2.3	Engine characteristics curves [16]	27
2.4	PM240-2 power module	30
2.5	CU310-2 PN control unit	31
2.6	SIMATIC IPC427E Microbox PC	32
2.7	Convertitor from 220V DC to 24V DC	33
2.8	Planetary Gearbox [7]	34
2.9	Planetary Gearbox scheme	35
2.10	Optical Incremental Encoder	37
2.11	Brake Module CAD	38
2.12	Transmission System CAD	39

2.13	Test bench summary diagram	42
3.1	CAD of the test bench	43
3.2	Gearbox guide CAD	45
3.3	CAD of the profile support	46
3.4	CAD of the pulley system	47
3.5	Pulley system supports	48
3.6	Mover	49
3.7	Inclined pulley support	51
3.8	Acquisition system scheme	52
3.9	Test bench with load module summary diagram	53
3.10	Photo of complete test bench	54
3.11	Photo of the acquisition system	54
3.12	Photo of pulley system	55
4.1	Forces on a single coil	59
4.2	Maximum acceptable spring diameter D	61
4.3	Number of turns as a function of spring stiffness	63
4.4	Length as a function of spring stiffness	63
5.1	Structure of the optical fibre	67
5.2	Classification of optical fibres	68
5.3	L: the phenomenon of refraction with $\theta_1 < \theta_c$; C: the phenomenon of refraction with $\theta_1 = \theta_c$; R: the phenomenon of refraction with $\theta_1 > \theta_c$	68
5.4	optical fibre acceptance cone	69
5.5	Effect of excessive optical fibre curvature	70
5.6	Bragg grating FBG	71
5.7	SmasrtScan interrogator	74
6.1	FBG installation point	77
6.2	CAD of the gearbox negative	78
6.3	First glue point of application	79
6.4	Adhesion of the optical fibre to the gearbox surface	80
6.5	Top view of the gearbox with optical fibres installed	81

6.6	Wavelength variation during installation	82
7.1	Photos and structure of the strain gauge [14]	83
7.2	Whearstone bridge	85
7.3	Installation point for optical fibres and strain gauges	87
7.4	Photo Optical Fibre and Strain Gauge 1 and 2	88
7.5	Photo Optical Fibre and Strain Gauge 3 and 4	88
8.1	Steps carried out in the six tests for load module validation	89
8.2	Steps carried out in the six tests for FBG evaluation	90
8.3	Schematisation of components used during tests	91
9.1	Response of spring 1 to step command	97
9.2	Response of spring 2 to step command	97
9.3	Torque generated by the two recall forces	98
9.4	Torque applied to the gearbox as spring elongation	99
9.5	Torque applied for three different test series	100
9.6	Linearised torque	101
9.7	Uncertainty in torque calculation with the approximate straight line	103
10.1	Optical fibre response to step command	105
10.2	Strain gauge response to step command	106
10.3	Synchronised strain gauge and optical fibre response to step command	108
10.4	Focus on the transitional phase	108
10.5	Sensor approximation lines in position 1 and 4	110
10.6	Sensor approximation lines in position 2 and 3	112
10.7	Comparison of deformation measured by strain gauges and optical fibres at position 1 and 4	113
10.8	Zooming in during the transitional phase Zooming in during the transitional phase	114
10.9	Pearson index choice points	115
10.10	Comparison of strain measured by strain gauges and fibre optics at selected points for Pearson's index	116
11.1	Response of sensors 1 and 4 to 30 deg step command	117

11.2	Trend of commanded current, wavelength and strain in the last test instants	118
11.3	FFT of commanded current signals, wavelength and deformation . .	119
A.1	Aluminium profile	123
A.2	Single pulley support	123
A.3	Support for pair of pulleys	124
A.4	Support for the aluminium profile	124
A.5	Pulley	124
A.6	Support for pair of pulleys	125
A.7	Support for the aluminium profile	125
A.8	Pulley	126

List of Tables

2.1	Engine engineering data	28
2.2	Engine Optimum Operating point	29
2.3	Engine Mechanical Data	29
2.4	Engine physical constants	29
2.5	Engine Limiting Data	30
2.6	Blocksize PM240-2 Input	30
2.7	Blocksize PM240-2 Output	31
2.8	SIMATIC IPC427E Microbox PC Basic Data	32
2.9	SIMATIC IPC427E Microbox PC ports	33
2.10	Planetary Gearbox Data	35
2.11	ORDER CODE ENCODER	36
2.12	Encoder Environmental Data	36
2.13	Encoder Materials Data	37
2.14	Encoder Mechanical Data	37
2.15	Encoder Electrical Data	37
2.16	Characteristics of motor and brake sprockets	40
4.1	Physical properties	59
4.2	Chemical Composition	59
5.1	Measurement and Processing	75
5.2	Mechanical, Environmental and Electrical	75
9.1	Relative error committed in each test	102

Chapter 1

Introduction

Aeronautics is one of the most modern areas of engineering, particularly the design of heavier-than-air aircraft. The first aircraft, belonging to this category, to be able to lift off from the ground was the Flyer of brothers Orville and Wilbur Wright on 17 December 1903. They are credited with the invention of the first rudimentary flight controls capable of adjusting pitch, yaw, and roll. The great development of aeronautics began in the 1920s and is due to research carried out during the First World War. This period saw the introduction of secondary control surfaces such as flaps, airbrakes and spoilers. The primary flight controls used were of the reversible type, characterised by direct power transmission between the pilot and the surface by hand. Around the 1950s, further technological progress due to the Second World War at the same time as the birth of civil aviation led to the emergence of larger aircraft. Due to their large size, which entailed high powers involved that could not be matched by human hand power, hydraulically powered flight controls were developed during this period. In the 1970s, technological development in the fields of electronics and computers led to the automation of the aircraft by reducing the pilot's tasks, which is the main source of error in aviation. Aircraft automation is achieved through control systems capable of stabilising the aircraft's attitude and monitoring the proper functioning of on-board systems. In the following decade, reversible flight controls began to be replaced with fly-by-wire and fly-by-light controls. The trend over the years has been to

make the aircraft more and more electronic and autonomous, through greater electrification of the aircraft involving a total or partial replacement of the hydraulic and pneumatic systems. Nowadays, we speak of 'More Electric' or 'All Electric' aircraft. This type of aircraft brings with it many advantages due to the reduction of systems and consequently of different components, leading to a reduction in operating costs and aircraft weight. In addition, continuous monitoring of the system through diagnostic and prognostic algorithms ensures optimised maintenance, further reducing costs. Finally, fuel consumption and emission levels are reduced due to reduced air bleed from the compressor stages.

1.1 Flight controls System

The evolution of control surfaces over the last century has led to modern aircraft being equipped with sophisticated Flight Control Systems (FCS) that must guarantee high manoeuvrability and control during the different phases of flight. FCS manages the trajectory and attitude of the aircraft, locally modifying the aerodynamic forces through a localised and continuously variable modification of the shape of the aircraft's control surfaces. Flight controls system must satisfy different requirements in order to ensure a high level of safety. In particular, they must be reliable, instinctive, sensitive and stable.

- The *reliability* of a system is a measure of the probability that the system will not fail, i.e. will not deviate from its nominal behaviour in a given period of time.
- The *Instinctivity* or speed of response is a fundamental requirement for primary flight controls. In fact, after receiving the pilot's input, the system has to respond to this input in a specific time interval δt .
- The *Sensitivity* of the control, which must ensure that the movement of the moving surface is as proportional to the input provided.
- The system must also be *stable* when reaching or remaining in the desired position under the influence of a disturbance.

The response to the command or disturbance must attenuate the residual oscillations within a certain time frame Δt within an amplitude band δ , which is expressed as a percentage of the maximum amplitude due to the command or disturbance, as shown in the figure 1.1 [12].

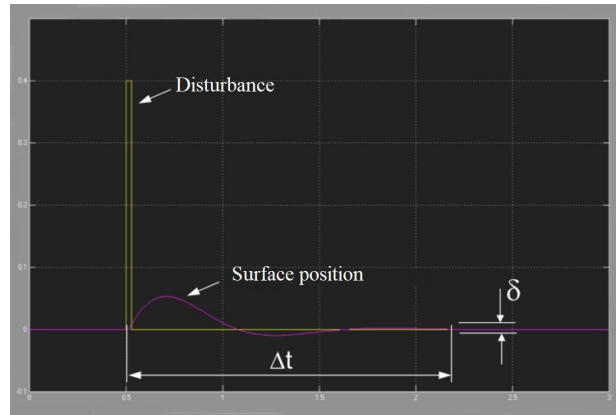


Figure 1.1. Response to impulsive disturbance

Flight controls can be divided into:

- Primary flight controls
- Secondary flight controls

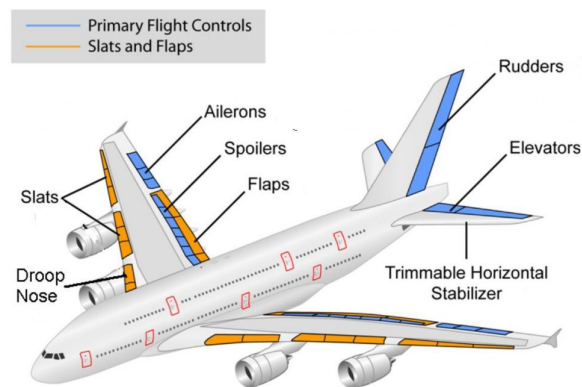


Figure 1.2. Control surfaces of a conventional aircraft

1.1.1 Primary Flight Controls

The primary flight controls, highlighted in blue in the figure 1.2, modify the attitude and consequently the trajectory of the aircraft by generating moments around the aircraft's barycentric axes. In conventional aircraft, the control surfaces used for this task are:

- **Ailerons**

The ailerons are located on the trailing edge near the wing tip, ensuring a higher contribution for the same surface area. They generate a rolling moment through an anti-symmetrical actuation of the surfaces.

- **Elevator**

The elevator is located on the trailing edge of the horizontal tail, the surfaces through symmetrical actuation generate an aerodynamic moment around the Y axis which is called pitching moment.

- **Rudder**

The rudder, located on the trailing edge of the vertical tail, generates an aerodynamic moment around the Y axis this is known as the yawing moment.

Depending on the characteristics of the aircraft such as the speeds involved, the size and consequently the weight of the aircraft, there are two different possible architectures for the primary flight controls. The type of architecture to be used depends mainly on the force required to overcome the hinge moment in order to actuate the moving surface. If this force is in the order of magnitude manageable by a pilot, a *reversible flight control architecture* is used, while an *augmented control architecture* is chosen.

Reversible architecture can only be used for small aircraft for which the pilot's muscular strength is manageable. In particular, if the architecture is composed of highly rigid elements such as rods and levers, it is called rigid, otherwise it is called flexible if it is characterised by flexible elements such as ropes and pulleys. For large aircraft, it is not possible to use a rigid architecture because of the high forces involved, which can be handled by an augmented architecture using hydraulic or electric servomechanisms.

The pilot sends an input which is transformed into either a mechanical, optical or electrical signal which reaches the servomechanism that drives the moving surface in an amplified but proportional way to the input. In this architecture, the pilot does not have a physical connection with the moving surface, so in order to guarantee the pilot the same sensation of effort that he would have with a reversible architecture, an artificial sensitivity device is used.

1.1.2 Secondary Flight Controls

Secondary flight controls, unlike primary controls, have an on-off actuation or a limited number of possible positions. They are only actuated during specific phases of flight by modifying the macroscopic characteristics of the aircraft such as the lift C_l and drag coefficient C_d . In a conventional aircraft, the secondary flight controls are those highlighted in orange in the figure 1.2:

- **Flaps**

The flaps, part of the HLD high-lift device, are installed on the trailing edge of the wing, close to the fuselage. They are operated symmetrically, modifying the curvature of the airfoil, which increases the maximum lift coefficient C_{Lmax} and the induced resistance and reduces the stall angle.

- **Slats**

Slats, part of the HLD high-lift devices, are located on the leading edge of the wing. They are activated symmetrically by determining the creation of a gap that connects the upper and lower zones of the airfoil, allowing the air to flow upwards, increasing its stall angle, and therefore also the value of the maximum obtainable lift coefficient, without however determining appreciable variations in the incidence of zero lift.

- **Spoilers**

Spoilers are located on the upper surface of the wing and have two different functions. If operated on a half-wing, the effect produced adds to the primary flight control due to the ailerons, increasing the roll moment generated. If activated symmetrically, they take over the function of the aerobrake, increasing resistance and reducing the lift of the aircraft.

1.2 Servomechanisms

In the previous section, we analysed the moving surfaces that manage the trajectory and attitude of the aircraft. In this section, we will discuss the servomechanisms necessary for the movement of these mobile surfaces. The servomechanism, or more generally the actuation system, must detect the input from the pilot or autopilot and calculate the current position of the control surface. The difference between the current position and the desired position is the error, which is reduced by appropriate control laws that determine how much variation is required to reach the desired position. The point at which the error is zero is the desired position of the control surface. Most of the servomechanisms used in aeronautics use control laws based on the position variable and are therefore called position servomechanisms. The possible types of servomechanisms are described below.

1.2.1 Hydromechanical Servomechanisms

The first of the servomechanisms designed is the hydromechanical servomechanism, which was installed on the first aircraft with an augmented architecture. In this type of servomechanism, shown in the figure 1.3 [11], a physical control law is implemented through a mechanical transmission. The high simplicity of physical control laws does not allow the modification of the input signal after it has been sent all commands will be executed by the servomechanism without any control filter on possible pilot errors.

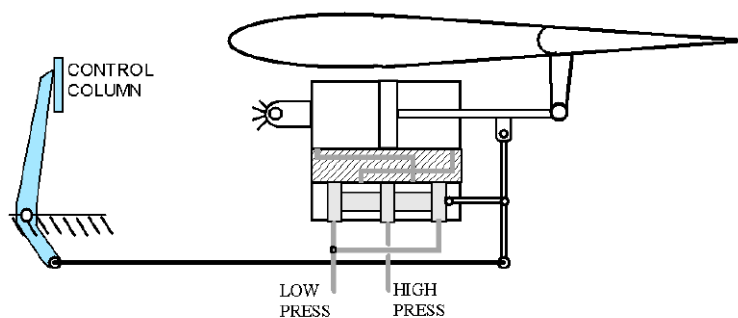


Figure 1.3. Schematisation of a hydromechanical servomechanism

The pilot, or autopilot, sends an input that reaches the servo valve through a mechanical transmission consisting of small ropes or rods. Pressurised oil enters one of the two chambers of the actuator and, generating a force, pushes the piston, causing the control surface to move. At the same time, in the other chamber, oil flows out of a return path of the servo-valve: this deters the rotation of a rod around a centre of instantaneous rotation that closes the servo-valve. The closure is complete when the spool has returned to its original position, preventing oil from flowing into the two chambers. This new position of equilibrium determines the achievement of the desired position.

1.2.2 Electrohydraulic Servomechanisms

High reliability and performance make electrohydraulic servomechanisms one of the most advanced choices for installation in modern aircraft today. Again, the power used to move the control surface is hydraulic, which is converted into mechanical power through the actuator.

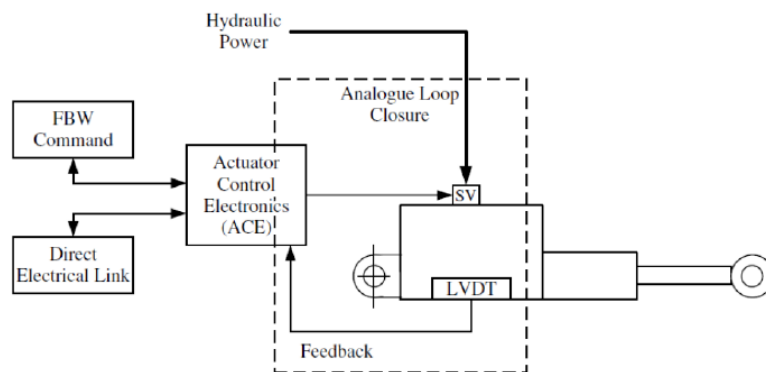


Figure 1.4. Electrohydraulic Servomechanisms scheme [15]

The main difference with hydromechanical servomechanisms consists in the method of command transmission. In the former, described above, it is done mechanically, whereas, in the case of electro-hydraulic servomechanisms, it is done electrically. The pilot's command is generated through the movement of the cloche, which in this case gives origin to an electrical signal proportional to the movement itself. The input to be sent to the servomechanism is determined by means of

an error-based control law, which is calculated by comparing the current position read by the position sensors on the aircraft and the position desired by the pilot's command.

Depending on the hydraulic flow rate to be managed, the complexity of the servo-valve will vary. The simplest ones, which manage a flow rate of fewer than 90 gallons per minute, have two stages: the first is a low-power electromechanical one of around 1 or 2 W and the second mechanical one is called a high-power main valve of around 10 kW. Valves handling flow rates greater than 90 gallons per minute may have three to four stages, where the stages following the first are all mechanical and are capable of higher and higher powers.

Flapper nozzle servo-valve

Let us look specifically at the simplest electro-hydraulic called flapper nozzle.

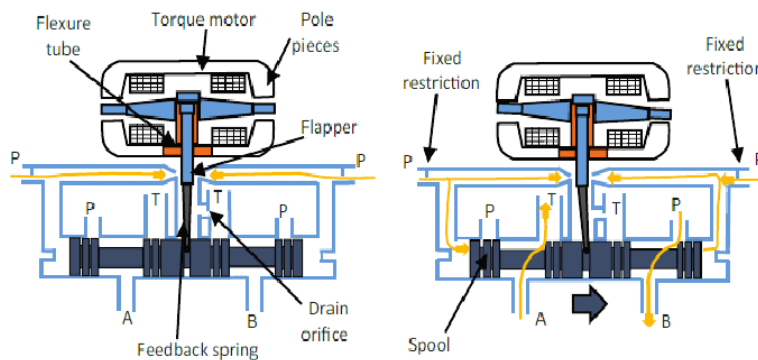


Figure 1.5. Flapper nozzle valve

The signal sent by the control unit reaches the first stage, which is characterised by a torque motor. The electrical flow inside the coils of the torque motor causes the generation of a magnetic field. The interaction between the permanent magnets of the torque motor and the magnetic field generated by the coils leads to the generation of a driving torque that rotates the torque motor itself to which the flapper is connected. The latter, depending on the direction of rotation, will tend to approach one of the two nozzles, causing a pressure difference between the two ports. The differential pressure thus generated determines a force on the spool in

the opposite direction to the movement of the flapper. The sliding of the spool determines the opening of the hydraulic lines connecting the servo-valve to the jack and at the same time brings the flapper back to its centred position thanks to the feedback spring. Pressurised oil flows into the jack chamber causing movement of the actuator and consequently of the control surface to the desired position. When the difference between the desired and the actual position is zero, the servo-valve will no longer receive any electrical input from the control unit, which results in the interruption of the electrical flow and consequently the cancellation of the magnetic field generated by the coils, which will no longer lead to the emergence of the drive torque on the torque motor, due to the interaction of the two magnetic fields. Due to the effect of the feedback spring, the flapper moves closer to the opposite nozzle, causing a differential pressure and a shift of the opposite spool to the previous one, allowing the spool to return to its centred position, closing the oil passage. The shift of the slider also returns the flapper to the centred position, thanks to the action of the feedback spring.

Jet pipe servo-valve

The flapper nozzle, due to their high complexity which leads to a greater possibility of malfunctioning, such as the clogging of one of the two nozzles, has led to the decision to develop valves with a similar operating principle but with increased reliability, we are talking about Jet-pipe valves.

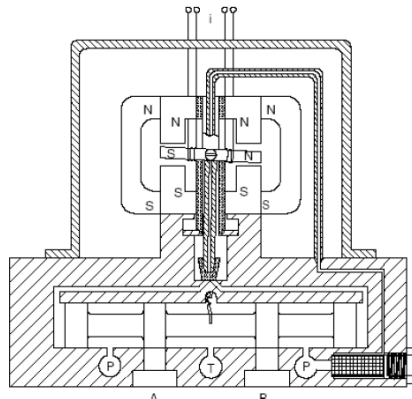


Figure 1.6. Jet pipe valve

In this case, the driving torque does not act on the flapper but on a central flexible pipe, inside of which is pressurised oil, which allows the jet to be directed through the channel. If the driving torque is non-zero, the jet will not be symmetrical, generating a differential pressure that will determine the movement of the slider; the translation of the slider brings the jet back to a centred position, thanks to the feedback spring, and this causes the opening of the channels that allow the oil to enter the ram chamber, determining the movement of the actuator and consequently of the control surface.

DDV servo-valve

A final, more innovative solution is the DDV valve. In this case, the electrical signal is supplied to a solenoid, which generates a magnetic field that determines the movement of the spool and the consequent opening of the hydraulic ways that allow oil to enter the jack chamber. This system allows the actuator to be controlled without the use of servopressure, ensuring greater valve precision. However, the high inertia of the solenoid results in a slower response of the servo-valve, which is why this system has not yet found much use in aeronautical applications.

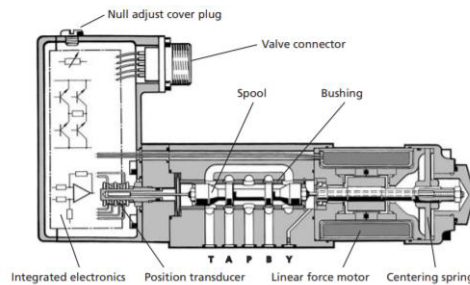


Figure 1.7. DDV valve

1.2.3 Electrohydrostatic Servomechanisms

In new aircraft that aspire to a More Electric philosophy, electro-hydrostatic servomechanisms are installed. This type of servomechanism does not require a connection to the hydraulic system, as the primary power source is almost exclusively

electrical. This makes it possible to reduce the importance of the hydraulic system on board the aircraft, and from this it follows that with the same reliability and performance, the complexity of the aircraft is reduced and consequently the maintenance costs necessary to keep it in service. In fact, the inconveniences of hydraulic disconnections from the aircraft and the complications associated with draining the system during reinstallation do not occur during maintenance operations. In addition, given the high weight of the hydraulic system, its reduction or complete elimination leads to a reduction in fuel consumption during flight.

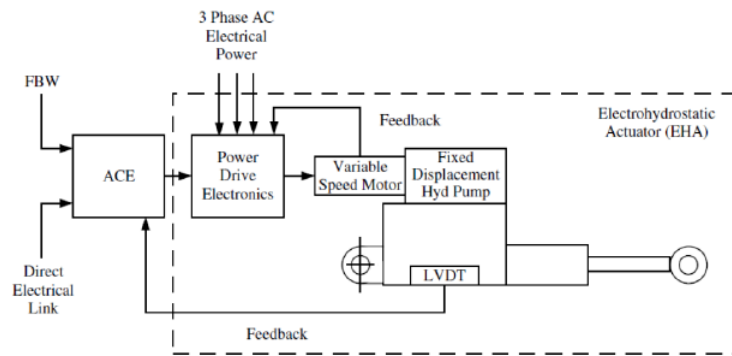


Figure 1.8. Electrohydrostatic Servomechanisms scheme [15]

The command provided by the pilot arrives at the servomechanical control electronics called ACE, where the position error is calculated from the difference between the current position estimated by the position transducers, coming from the LVDT, and the position desired by the pilot. The error signal thus calculated after being amplified and appropriately filtered from noise is sent to the control unit to generate the input signal. The Power Drive Electronics (PDE) receives a three-phase AC power supply and, based on the feedback signal from the variable speed motor, adjusts the required power. This motor activates a hydraulic pump with constant displacement, which allows the pressurised oil from the servo-valve to enter the chamber of the piston jack, which determines the movement of the control surface. The advantage of this architecture is that the system can be treated as a hydraulic actuator, due to its operating principle, even though it is not physically connected to the hydraulic system.

1.2.4 Electromechanical Servomechanisms

The last type of servomechanisms we will discuss are electromechanical servomechanisms. These, like the electro-hydrostatic servomechanisms, follow the More Electric philosophy; in fact, they do not involve the use of hydraulics. The mechanical power required to move the control surface is generated by an electric motor connected to a gearbox that transforms electrical power into mechanical power.

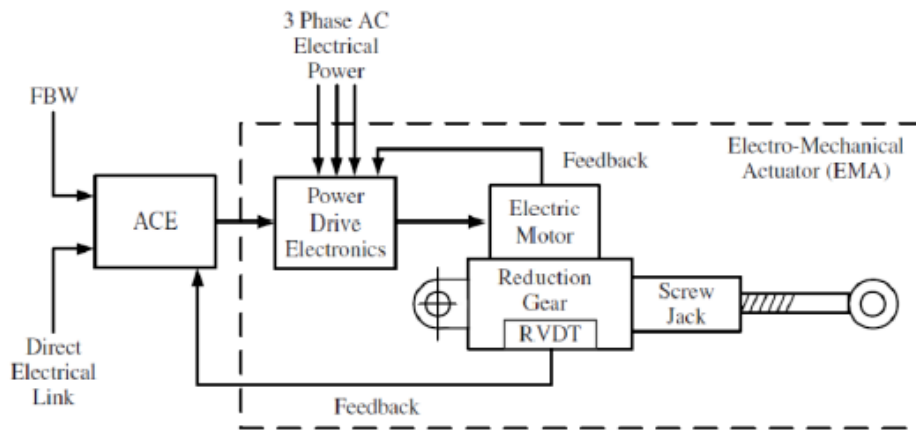


Figure 1.9. Electromechanical Servomechanisms scheme

The principle of operation is very similar to the electro-hydrostatic servomechanism. The pilot command reaches ACE which calculates the error as the difference between the desired position and the actual position provided in feedback from the LVDT. The error, being a low intensity signal, must be amplified and filtered from noise, after which it reaches the PDE, which receives the three-phase AC power supply to regulate the power supply to the electric motor in order to obtain the desired position.

Electromechanical servomechanisms require a gearbox, this is due to the characteristics of the electric motors and users to which they are normally connected. In fact, the rotational speed of the motor output shaft is very high, and consequently, since power is the product of torque and speed, very high power is needed to guarantee the torque required by the user. Furthermore, torque is related to the size of the motor. Large dimensions and excessive weights, as is well known,

have always been the historical enemies of aeronautical engineering, so speed reducers are used to contain them and succeed in guaranteeing the torque needed by the user. In this way, the high speed at the output shaft is reduced, bringing it within the requirements of the regulations, approximately 50-60 rpm per second for the primary flight controls and 5-6 degrees per second for the secondary ones, while still managing to guarantee the torque requirements. Electromechanical servomechanisms can be divided into two groups:

- **Linear**

Which allow the conversion from rotary to linear motion; either through a reduction stage connected to the motor these are called gear drives or through a direct connection to the conversion device, these are called direct drives.

- **Rotators**

Which supply the user with a rotary motion specially reduced in speed by a reduction stage.

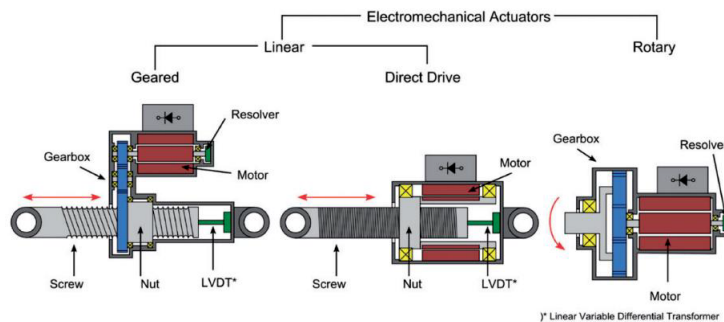


Figure 1.10. Electromechanical Servomechanisms classification

The advantages of this type of architecture stem from the elimination of the hydraulic system, which leads to a reduction in system weight and complexity, resulting in lower fuel and maintenance costs. However, the failure modes affecting electromechanical servomechanisms are not yet fully known, so the reliability that these systems can guarantee is still insufficient to make them suitable for primary flight control applications. One of the major problems, which does not allow their use for primary flight controls, is maintaining a fixed position under the action

of an applied load, as this would require a power supply of the same phases, which would lead to overheating of the windings and the insulating material used, a problem that can be overcome by using an irreversible transmission system. However, this would prevent the moving surface from floating in the event of a failure of the servomechanism. This is why today they are only used for retracting and retracting the landing gear and for operating the secondary control surfaces.

1.3 Prognostic and Health Management (PHM)

Prognostic and Health Management (PHM) is an innovative design philosophy that involves real-time data analysis to perform fault diagnostics and prognostics. The PHM philosophy, by analysing the actual state of the system through a diagnostic analysis and an assessment of the remaining useful life RUL, allows for a better organisation of maintenance interventions, which will be targeted at the actual state of failure, thus avoiding unnecessary maintenance checks. In contrast to previous design philosophies such as Safe Life, Fail Safe and Damage Tolerance in which maintenance interventions are scheduled after a specific period of time, which may vary depending on the chosen design philosophy, without having the certainty that the component undergoing maintenance control will actually fail, leading to an increase in maintenance costs.



Figure 1.11. Prognostic and Health Management scheme [5]

Prognostic and diagnostic algorithms are at the heart of the PHM philosophy. The algorithms developed use information on the health of the system or individual components in real time to prevent possible common faults and the propagation of a single fault to other components. Real-time monitoring allows faults to be identified in real time so that the right countermeasures can be taken to minimise their consequences through decision-making processes developed to improve reliability, safety and maintainability. This significantly reduces system maintenance costs. The PHM philosophy can be divided into five different phases:

1. Monitoring data acquisition

Collection of data from systems and individual components to be subsequently processed by diagnostic and prognostic algorithms.

2. Monitoring data processing

Processing of previously acquired data, after noise filtering. In this phase, the export of system characteristics and its health status through time and frequency domain analysis takes place.

3. Fault detection

Comparison of the actual system status with the nominal status; if there is an excessive discrepancy between the two data, the system sends a warning message confirming the detection of a fault or anomaly.

4. Fault diagnostics

After detecting the fault it is isolated, the next step is to quantify the severity of the fault according to its consequences and to identify the failure mode.

5. Decision of the maintenance activity to be carried out

Choosing the correct maintenance procedure to follow among different alternatives, through a trade-off on the advantages and disadvantages of possible maintenance activities based on the information obtained from the diagnostic and prognostic algorithms.

Chapter 2

Test bench

In order to simulate the operation of a secondary control surface, the Politecnico di Torino has over the years developed a test bench capable of reproducing the operation of an electromechanical actuator. The aim of this thesis is to complete the bench by implementing a new module called the load module. The load module adds to the test bench the possibility of simulating the effect of an external load on the transmission end. The load simulated in this way can represent various physical phenomena affecting the operation of the actuator such as an aerodynamic load on the transmission, friction phenomena, etc.

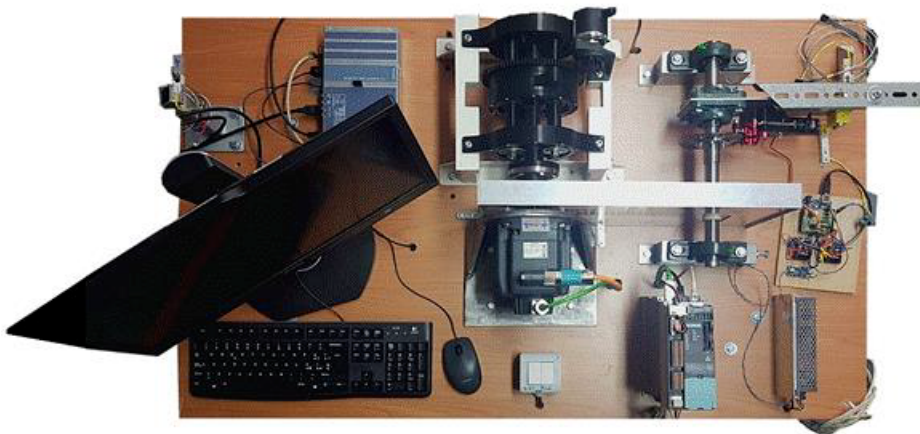


Figure 2.1. Photo of the test bench

Before explaining the design and operation of the load module developed in this thesis, let us first analyse the bench in its starting condition by describing its operation and components. The bench can be divided into three modules:

- Actuation module
- Brake module
- Transmission System

The actuation module and the braking module are the heart of the test bench, the transmission system links the two modules together. The test bench in the laboratory was already able to simulate the behaviour of the actuator both under nominal conditions and in the presence of losses due to gear tooth backlash and internal friction forces.

2.1 Actuation module

The actuation module consists of a planetary gearbox and various electronic components produced by Siemens, such as the Microbox PC, the Control Unit and the Power Module, which allow the Sinamics S120 PMSM motor to be controlled as desired. Appropriate software supplied by Siemens, specifically *TIA portal* and *Starter*, allows a position or speed command to be given to the motor, and the control unit manages the power to be supplied to the motor through the inverter.

2.1.1 Motor PMSM

The motor installed on the test bench is the Permanent Magnet Synchronous Motor, SIMOTICS S 1FK7060-2AC71-1CG0 developed by Siemens. The motor interfaces with the other components through mechanical or electrical signal connections. The output shaft of the motor is mechanically connected to the planetary gearbox through a flexible coupling and to the braking system through the transmission system. A sprocket on the motor shaft supports the chain that connects the actuation module to the brake module. Finally, the motor is fixed to the test bench on a steel support. Signal connections allow the motor to communicate

with the control unit and the inverter by sending the feedback signals required to control the motor.



Figure 2.2. SIMOTICS S 1FK7060-2AC71-1CG0 [16]

This type of motor has various limitations due to temperature, electromagnetism or mechanical factors. The characteristic curves are shown in the figure 2.3.

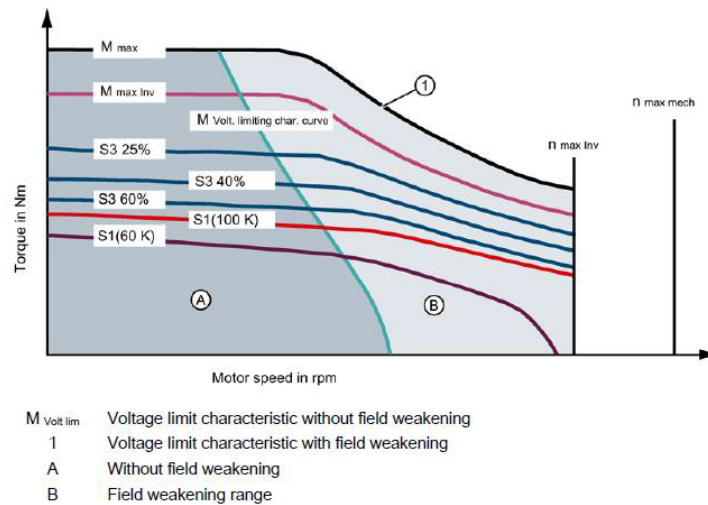


Figure 2.3. Engine characteristics curves [16]

- **Thermal factors**

There is no external cooling system, the heat being dissipated through the

external surface of the motor. The temperature tends to rise because of losses due to friction, current or no-load losses. 1FK7 motors can work up to an average winding temperature of 145 °C. The S1 curve represents the limit of continuous operation of the motor, which corresponds to use according to thermal class F (155 °C). Similarly, curve S1(60K) represents the operating limit of the continuous motor, which corresponds to use according to the lower thermal class B (130 °C). The curves S3 25%, S3 40%, S3 60% and M_{max} indicate the limits in periodic intermittent service, where the percentage is in relation to the maximum torque. In these regions a higher load can be applied, depending on the duration of the active phase, with a cycle time of 10 min and an overtemperature of 100 K.

- **Mechanical factors**

The speed limits, $n_{max_{mech}}$ indicates the mechanical speed limit, related to the centrifugal forces of the rotor and the life of the bearings. The speed limit $n_{max_{inv}}$ indicates the electrical speed limit, related to the drive voltage and/or its maximum frequency.

The main characteristics of the motor are shown in tables below 2.1,2.2,2.3, 2.4 and 2.5 [16]:

Engineering Data	
Rated speed (100 K)	2000 rpm
Number of poles	8
Rated torque (100 K)	5.3 Nm
Rated current	3.0 A
Static torque (60 K)	5.00 Nm
Static torque (100 K)	6.0 Nm
Stall current (60 K)	2.55 A
Stall current (100 K)	3.15 A
Moment of inertia	7.700 kg cm ²
Efficiency	90.00

Table 2.1. Engine engineering data

Optimum Operating point	
Optimum Speed	2000 rpm
Optimum Power	1.1 kW

Table 2.2. Engine Optimum Operating point

Mechanical Data	
Motor type	Permanent-magnet synchronous motor
Shaft height	63
Cooling	Natural cooling
Radial runout tolerance	0.040 mm
Concentricity tolerance	0.10 mm
Axial runout tolerance	0.10 mm
Vibration severity grade	Grade A
Connector size	1
Temperature monitoring	Pt1000 temperature sensor
Electrical connectors	Connectors for signals and power
Holding brake	without holding brake
Shaft extension	Plain shaft
Encoder system	Encoder AM24DQI: 24 bits + 12 bits multi-turn
Degree of protection	IP64

Table 2.3. Engine Mechanical Data

Physical constants	
Torque constant	1.1 Nm/A
Voltage constant at 20° C	121.0 V/1000min ⁻¹
Winding resistance at 20° C	2.75 Ω
Rotating field inductance	30.5 mH
Electrical time constant	11.10 ms
Mechanical time constant	1.75 ms
Thermal time constant	30 min
Shaft torsional stiffness	40500 Nm/rad
Net weight of the motor	7.1 kg

Table 2.4. Engine physical constants

Limiting Data	
Max permissible speed (mech.)	7200 rpm
Max permissible speed (inverter)	4750 rpm
Maximum torque	18.0 Nm
Maximum current	10.7 A

Table 2.5. Engine Limiting Data

2.1.2 Power Module

The Blocksize PM240-2 power module, also manufactured by Siemens, is installed on the test bench. It executes the commands sent by the control unit and powers the motor windings, essentially acting as an inverter. It is connected to the control unit via the PM-IF interface and to the electric motor through a DRIVE CliQ power cable. It is powered by a three-phase voltage of 380 V. The following tables 2.6 and 2.7 show the main characteristics [18]:



Figure 2.4. PM240-2 power module

Input	
Number of phases	3 AC
Line Voltage	380 - 480 V \pm 10
Line frequency	47 - 63 Hz
Rated current (LO)	39.90 A
Rated current (HO)	36.00 A

Table 2.6. Blocksize PM240-2 Input

Output	
Number of phases	3 AC
Rated voltage	400 V
Rated current (LO)	32.00 A
Rated current (HO)	26.00 A
Max. output current	52.00 A
Rated power IEC 400V (LO)	15.00 kW
Rated power NEC 480V (LO)	20.00 hp
Rated power IEC 400V (HO)	11.00 kW
Rated power NEC 480V (HO)	15.00 hpkW
Pulse frequency	4 kHz
Output frequency for vector control	0 - 200 Hz
Output frequency for V/f control	0 - 550 Hz

Table 2.7. Blocksize PM240-2 Output

2.1.3 Control Unit

A CU310-2 PN control unit, also manufactured by Siemens, is installed on the test bench. It sends commands according to a specific control law to the power module described above. It is powered at 24 V AC and is connected to the motor through a DRIVE CliQ cable and to the PLC and PC through an Ethernet cable. It receives position signals from the Encoder, installed on the planetary gearbox, and exchanges data with the Arduino board. It send a trigger signal that is used to synchronise the data coming from the Arduino with that coming from the motor. The control unit can perform open and closed loop control functions of the drive depending on what is controlled by the SIMATIC microbox PC.



Figure 2.5. CU310-2 PN control unit

2.1.4 Microbox PC

The test bench is equipped with a PLC (Programmable Logic Controller), also manufactured by Siemens, specifically the SIMATIC IPC427E Microbox PC. The purpose of the PLC is to provide a sinusoidal command, characterised by an amplitude and phase set in order to carry out an analysis of the frequency response. It allows the impementation of even the simplest commands such as steps and ramps. It allows measurement and control of operations, with the possibility of implementing control techniques, implemented with codes in C or C++ language or with controller/WinCC RT Advanced software. The following table 2.8 and 2.9 shows the main features [17]:



Figure 2.6. SIMATIC IPC427E Microbox PC

Basic Data	
Power supply	24 V DC (-20%/+20%) max. 4 A
Processor	Intel® Core™ i3-6102E Processor
Main Memory	16 GB DDR4-SDRAM SODIMM
Operative System	Windows Embedded Standard 7 SP1, 64 bit
SSD	HD graphic onboard
Installation	DIN rail, wall mounting or vertical mountig
Free slots for expansion cards	Up to 2 × PCIe cards

Table 2.8. SIMATIC IPC427E Microbox PC Basic Data

Ports	
Serial	COM1 / COM2
USB ports	4x USB V3.0 (high current)
Ethernet ports	3x Gbit Ethernet
Keyboard, mouse	Connected via external USB port
Graphics	2 x DisplayPort DPP

Table 2.9. SIMATIC IPC427E Microbox PC ports

2.1.5 Convertitor

The components on the test bench require a different supply voltage, so a converter has been installed to switch from 220 V DC to 24 V DC. This is used to supply the PLC with 24 V DC and is connected to a second converter to further reduce the voltage to 6 V DC to supply the servomotor of the brake module. Inside the box containing the Arduino is a second converter that converts the current from 24 V DC to 5 V DC to power the encoder.



Figure 2.7. Convertitor from 220V DC to 24V DC

2.1.6 Planetary Gearbox

A planetary gearbox is installed on the test bench, connected to the motor shaft by an elastic coupling. It was produced by the Polytechnic of Turin using the Fused Deposition Modelling technique. Due to the production technique used, the gearbox cannot reach high speeds, but at the same time, it allowed faster production and was specific to the studies to be carried out. The main characteristic

of this component is its high transmission ratio, which guarantees a reduction in the angular speed of the motor shaft and consequently an increase in the torque produced by the electric motor. The gearbox is installed on the bench through a dedicated steel alloy support, on which the two end crowns with internal toothing are fixed.

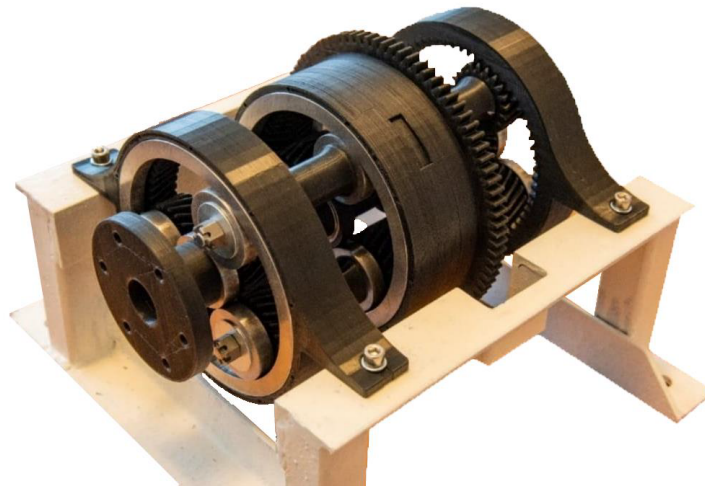


Figure 2.8. Planetary Gearbox [7]

Structurally, the gearbox consists of four shafts and three internal gears. The output shaft of the motor turns the gearbox's central shaft, which is called a sun gear, which consists of three spacers and two gear wheels with a fixed specular number of teeth. This gear rotates the three external shafts, called planetary gears, each of which consists of two terminal satellites, which belong to a first planetary stage, and a central satellite, which belongs to a second planetary stage, i.e. the output stage. The central wheels have a double helix toothing, while those at the ends have specular angle toothing to ensure greater support for axial loads. In addition, this gear configuration allows four shafts to support themselves without the need for bearings. In the table 2.10 below there are the most significant data of the planetary gearbox, the figure 2.9 shows a scheme of the gearbox [7]:

disc, i.e. in correspondence of a transparent zone. If the photodetector receives the signal, it generates a logic signal of 1, otherwise it returns 0. The encoder generates two waveforms called A and B specially squared and shifted by 90°. The A or B wave is used to derive the relative displacement while using both waves in quadrature to derive the direction of rotation. If "A" follows "B", for example, the disc rotates clockwise. If "B" follows "A", then the disc rotates anti-clockwise. A third channel, called Z, calculates the assumed position from a zero reference position, obtained by resetting the sensor at the start of the test, and sends a signal each time a complete revolution of the disc is made. Tables 2.11, 2.12, 2.13, 2.14 and 2.15 contains the characteristic data of the model used [2].

ORDER CODE ENCODER		
Name	Code	Meaning
Model	TSW581HS	Bidirectional + index
Assembly	M2	M2 spring type
Pulse rate	5000	5000
Power Supply	5	5V ± 5%
Output frequency	V	From 0 a-up to 300 kHz
Protection Degree	K4	IP64 (EN60529)
Shaft	B127	12.7 mm of diameter
Electrical connection	PL10	Radial cable gland with cable 1m long
Output Circuits	PP2-5	Push-Pull 5V output only

Table 2.11. ORDER CODE ENCODER

Encoder Environmental Specifications	
Operation temperature range	-10°C ÷ +70°C
Storage temperature range	-30°C ÷ +85°C
Relative humidity	98% RH without condensing
Vibrations	10 g (from 10 up to 2000 Hz)
Shock	20g (for 11 ms)

Table 2.12. Encoder Environmental Data

Encoder Materials	
Flange	Non corroding Aluminium
Housing	Polyamid 6 (PA6)
Shaft	Stainless steel

Table 2.13. Encoder Materials Data

Encoder Mechanical specifications	
Shaft rotation Speed	6000 RPM continuous
Starting torque at 25°C	-0.025 Nm
Bearings life	5 *10 ⁹ revolutions (minimum)
Moment of inertia	40 g cm ²
Weight	0.25 Kg

Table 2.14. Encoder Mechanical Data

Encoder Electrical Specifications	
Synchronous index output	Default on channel A;A+B optional
Supply Current without load	150 mA max
Protection	Short circuit protection

Table 2.15. Encoder Electrical Data



Figure 2.10. Optical Incremental Encoder

2.2 Brake module

The test bench simulates the performance of an actuator connected to a control surface. For this purpose, it is necessary to reproduce the internal friction acting on the control surface during flight. The task of reproducing these loads falls to the braking module, which applies a braking torque to the electric motor.

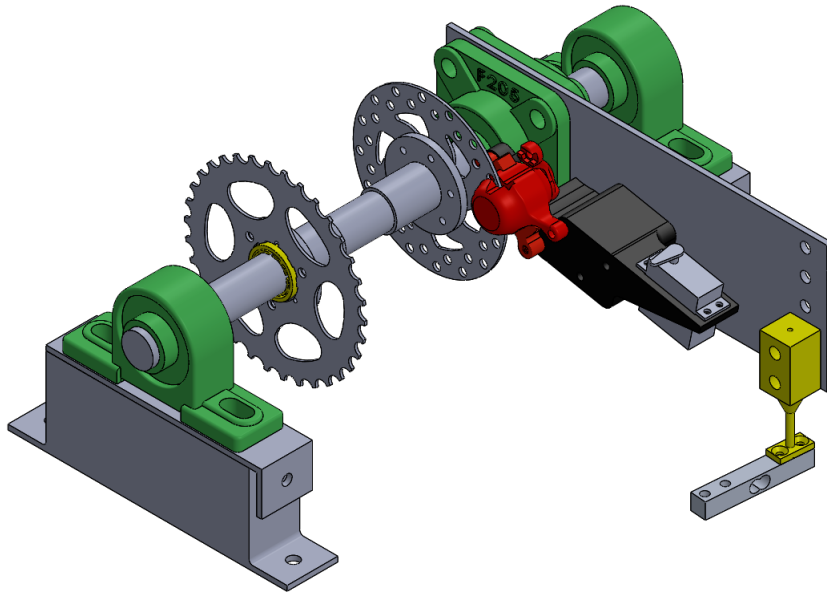


Figure 2.11. Brake Module CAD

The brake module is characterized by the brake shaft, made of alloy steel, positioned parallel to the electric motor. The shaft is installed on two standard self-aligning bearings, located at the ends, which guarantee rotation and alignment within a minimum tolerance. The shaft is equipped with two supports: the first allows the positioning of the brake disc while the second houses the sprocket of the transmission chain that connects the actuation module to the braking module. The alignment of these two elements is ensured by two specially designed rings. The brake disc has a perforated surface, with the holes at a constant distance, which allows more efficient heat dissipation. In the proximity of the disc, between the two self-aligning bearings, there is a metal plate that supports a joint specially designed in Solidworks and produced using Fused Deposition Modelling (FDM) additive manufacturing technology. It performs a dual function: first as a support for the braking system's caliper and the servomotor through a steel cable connected to a turnbuckle, and second to transmit the loads to the load cell beneath it. The brake system caliper and servomotor, as already mentioned, are connected by means of the tie rod, which allows the braking module to be actuated according to the following principle; the rotation of the servomotor in contact with the brake

disc generates friction and decelerates the brake shaft; stopping the rotation of the servomotor, the tie rod releases the brake caliper lever, so the magnetic pads move away from the brake disc, canceling the friction. The load produced reaches the metal plate, transferring it to the load cell, on which a strain gauge is installed to measure the force to which the load cell is subjected through a change in the internal resistance of the sensor, which will determine a change in the voltage read by the Arduino board to which the load cell is connected. Having thus known the force by multiplying it by the arm corresponding to the distance between the point of application of the load and the axis of rotation of the brake shaft, we obtain the value of the braking torque generated by the braking module.

2.3 Transmission System

The interaction between the actuation module and the brake module described above is essential for the proper performance of the test bench. The two modules are connected to each other by a chain transmission system consisting of a roller chain and two toothed wheels, one installed on the drive shaft and the other on the brake shaft respectively.



Figure 2.12. Transmission System CAD

The chain transmits mechanical power between the two sprockets, transferring rotary motion from one shaft to the other. Specifically, the driving torque generated by the actuation module is transmitted to the brake module inducing shaft rotation. In the same way, the braking torque generated is transmitted to the drive shaft by generating deceleration. It should be noted that the braking torque is transmitted to the motor output shaft and not to the gearbox. This is due to the production method used for the gearbox, which would not be able to withstand such high loads, which would result in its damage. For this reason, it was decided

to apply the torque to the motor output shaft and not to the gearbox.

Analyzing the transmission system in detail, the chain is a classic chain used in cycling and has two types of links, an external one and an internal one that alternates with each other. The external links consist of two outer plates held together by pins that pass through the bushings of the internal links, while the internal links consist of two internal plates held together by two sleeves or bushings on which two rollers rotate. This type of chain guarantees a reduction in friction, which will be greater if the chain has appropriate lubrication, resulting in less wear and better performance. Below a summary in table 2.16 about the characteristics of the sprockets used on the test bench is reported.

Sprockets	
Diameter motor sprocket	14.2
Teeth number motor sprocket	34
Diameter brake sprocket	9
Teeth number brake sprocket	23

Table 2.16. Characteristics of motor and brake sprockets

Knowing the geometric characteristics of the two gearwheels, it is possible to calculate the transmission ratio realised by this system, which is 1.48. Having noted the transmission ratio of the system, it can be seen that the rotational speed of the braking shaft is lower than the speed of the drive shaft, in contrast to the torque, which is higher. Specifically, a transmission ratio of 1.48 can be explained with the following example: for the wheel connected to the braking module to complete one complete revolution, the wheel connected to the drive module must complete 1.48 revolutions, i.e. 48% more revolutions. The decision to use a non-uniform gear ratio is not accidental, but is due to the need to always operate the brake under operating conditions, i.e. generating a braking torque of between 20 and 30 Nm. This torque would be higher than the motor stall torque of 6 Nm, and would force the brake to work in a range lower than the operational one, with a consequent increase in random errors which would compromise the repeatability of the tests. The optimum point was found with a gear ratio of 1.48, with which the actuation module would feel a lower braking torque than that actually produced, not stalling, and at the same time the brake module would work at its operating

point.

The transmission by a chain, in addition to guaranteeing the above-mentioned advantages, also makes it possible to act on a chain tensioner, present on the test bench, varying the tension level of the chain in order to introduce more or less backlash between the two sprockets. The tension is regulated through an M8 screw inserted on the side surface of the tensioner, which consists of an L-shaped steel plate resting on the supports of the two self-aligning bearings of the brake shaft. By decreasing the tension on the chain, more backlash can be introduced between the two sprockets, which leads to a delay in the transmission of drive torque and braking torque. Conversely, an increase in tension leads to a reduction in a backlash resulting in faster system response. Backlash in the drive system can be used to introduce into the test bench simulation of the delay due to on-board systems in the aircraft.

2.4 Test Bench Overview

After describing the individual components, which are already present on the test bench, and explaining the functions they perform, an overview of the test bench is shown in the figure 2.13.

The diagram shows the components of the actuation module in yellow, the transmission system in red and the components of the braking module in blue. The different connections between the components are also highlighted: in black are the mechanical connections, in dotted black the Ethernet connections, in orange the data connections and in red the power connections. On the inverter and the first converter, there are arrows without connections, which correspond to an external power supply to the test bench.

The test bench in the laboratory was already able to simulate the behaviour of the actuator both under nominal conditions and in the presence of losses due to gear tooth backlash and internal friction forces. Losses due to backlash are reproduced by means of the position micro-mover, which allows the wheel, connected to the incremental encoder, to come into contact with the gear, allowing its position to be assessed. Losses due to internal friction are simulated through the braking module as explained above.

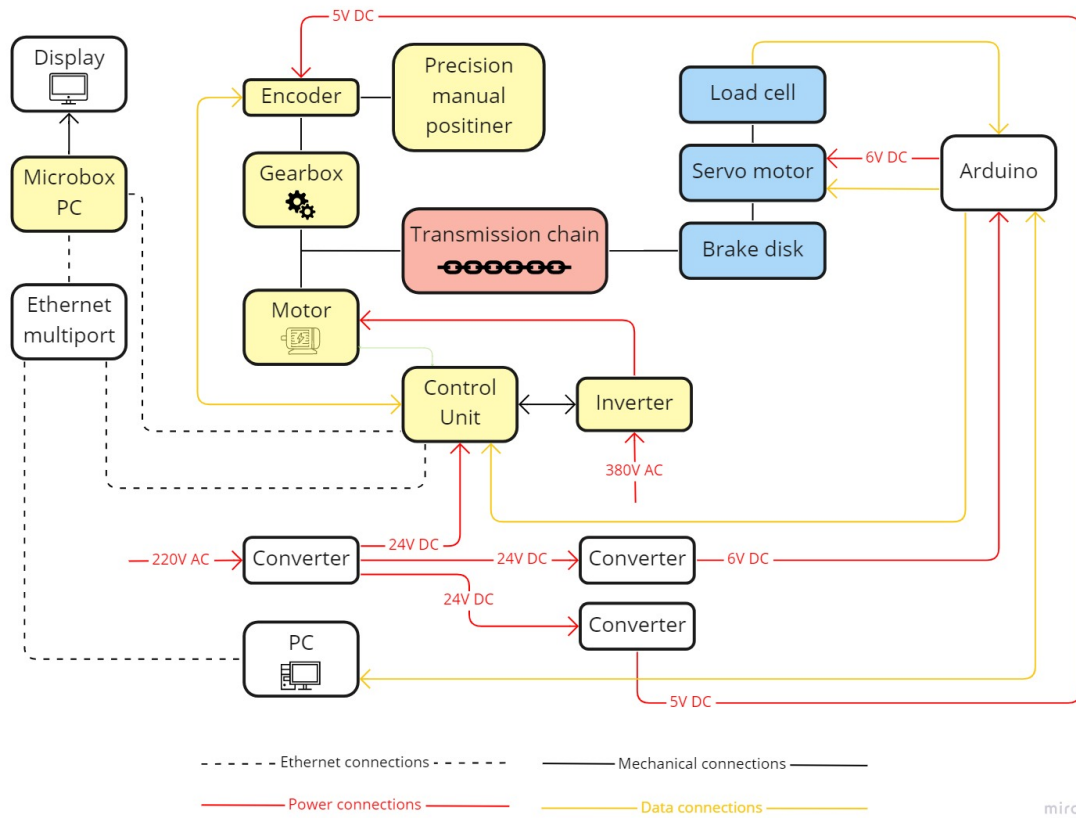


Figure 2.13. Test bench summary diagram

Chapter 3

Load module

As mentioned above, the aim of this thesis is to complete the test bench, described in the previous chapter, by introducing a system capable of reproducing the external loads at the end of the electromechanical actuator transmission. The loads simulated can be, for example, the aerodynamic forces, which are typically the loads that stress the control surface during the various flight phases, and with this aim in mind, the load module that forms the third module on the test bench was constructed. The figure 3.1 shows the CAD of the load module's main parts:

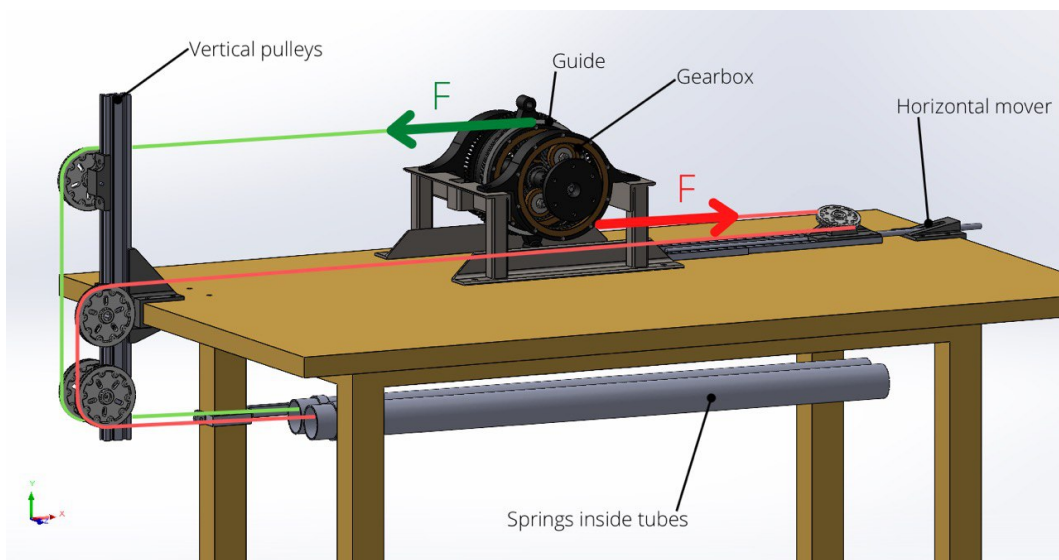


Figure 3.1. CAD of the test bench

To simulate the external load, a torque must be applied to the gearbox, which is connected to the electric motor. In order to generate the desired torque, a complex system of ropes, pulleys and springs was designed. The load module utilises the torque generated by the electric motor, which rotates the gearbox on the surface of which are two hooks offset 180 degrees from each other. A rope is connected to each hook, which is brought to a state of tension by the rotation of the gearbox, which is transmitted by a pulley system to the spring. The spring generates a return force, which is transmitted back to the gearbox by the pulleys and the rope. Using a pair of springs will generate a torque given by the pullback forces multiplied by the arm equal to the radius of the gearbox guide. For reasons of space, the springs have been placed below the test bench and for safety reasons placed inside a 2.5 m long PVC tube. The protective tube not only performs a safety function but also allows the load to be discharged through the table. To do this, the tube has been divided into two sections, the first one metre long so that one end coincides with the legs of the table where there is a plywood board, which is necessary to hold the tubes in position and to discharge the forces involved. The tubes are attached to the plywood board through the external connection . The second 1.5 m long section provides the spring with the space it needs to reach its maximum elongation. The other end of the spring is connected via a small rope to load cells, which are in turn connected to an Arduino, which allow the elastic return force generated by the spring to be evaluated.

3.1 Gearbox guide

The figure 3.2 shows the gearbox guide, around which the ropes connected to the gearbox hooks are wrapped. Designed in Solidworks environment and 3D printed using the Fused Deposition Modelling (FDM) technique. It is characterised by a U-shape, the width of which was chosen to ensure that the rope can be wound around the guide five times. The rope has a diameter of 0.8 mm, from which it follows that the width of the guide will be 4 mm. The guide performs a containment function for the ropes within a well-defined space to prevent them from being free to move on the test bench causing damage to the test bench. It was decided to have each rope wrapped with two turns around the guide to ensure enough rope

for the system when it is put into operation.



Figure 3.2. Gearbox guide CAD

3.2 Pulley system

The first subsystem of the load module is the pulley system. The pulley system is able to transmit the recall force generated by the springs on the gearbox. Looking at the test bench in the figure 3.1, one can see the pulley system on the left. The components that make it up are:

- An aluminium profile on which the supports with their respective pulleys are positioned.
- A support to fix the aluminium profile to the table on which the test bench is placed.
- Four pulleys.
- Two supports on which a single pulley can be mounted.
- A support on which two pulleys can be mounted .
- Eight shielded steel ball bearings with an inner diameter of 4 mm and an outer diameter of 13 mm.
- Three M4 threaded rods.
- Four M6 hexagon head screws 10 cm long and six pan head screws 2 cm long.

All components except the profile were designed in Solidworks and 3D printed using the Fused Deposition Modelling (FDM) technique. The CAD of the components designed in Solidworks for the pulley system can be found in appendix A.1. The profile is made fixed to the table through its support, shown in the figure 3.3.

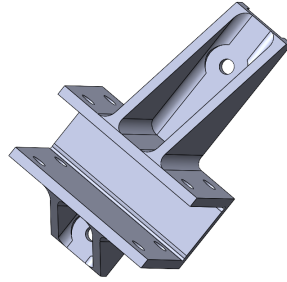


Figure 3.3. CAD of the profile support

The support has a C-shape that allows it to be fixed to the table with four M6 screws. The upper and lower faces are elongated. This shape is not accidental, it allows it to embrace the aluminium profile and to guarantee adequate load resistance thanks to the ribs placed in the direction in which the load is applied. It can be seen that the elongation is greater at the top than at the bottom, due to the type of loads to which the profile is subjected. In fact, the pulley placed higher up will have a greater arm and consequently a greater torque to compensate for the support, hence the need to have a greater elongation in that direction, to reinforce the support.

Connected to the profile are the three pulley supports, whose only degree of freedom is to slide along the axis of the profile. Once the appropriate position has been chosen, each support is fixed to the profile by means of two M6 pan head screws. The figure 3.4 shows the pulley system. Starting from the top, one can see the first and second supports where the first and second pulleys, respectively, indicated by the numbers in the figure, are connected. The pulleys are cantilever-mounted on an M4 threaded rod and two shielded bearings that allow them to rotate around the rod. The third support, the lowest in the figure, allows the installation of pulleys three and four simultaneously, also mounted cantilevered on

an M4 threaded rod and with two shielded bearings for each pulley. Each pulley has a throat diameter of 80 mm and performs a different function:

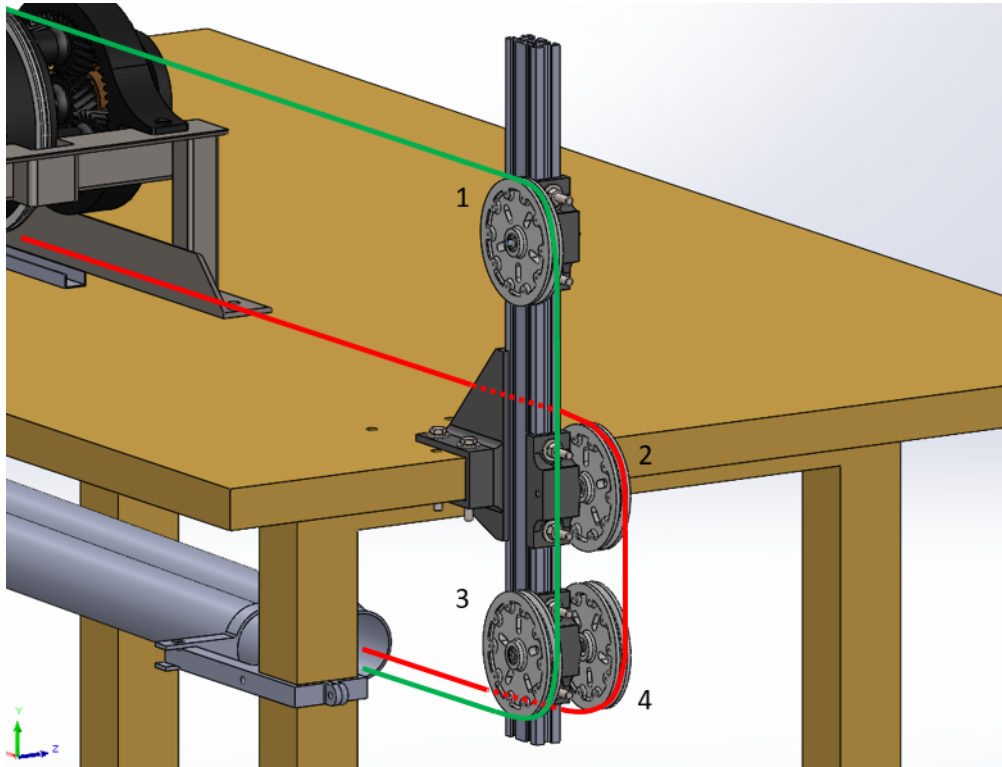


Figure 3.4. CAD of the pulley system

- **The first pulley**

The first pulley, placed higher up on the profile, sends the rope connected to one of the hooks of the gearbox downwards. The horizontal orientation of the pulley is crucial in determining the correct positioning of the profile on the test bench. This positioning is determined by the perfect alignment of the pulley throat with the gearbox guide. The vertical alignment of the pulley in relation to the gearbox guide is also important. It can be seen that if the pulley throat were vertically aligned with the gearbox guide, the direction of the rope tension would be tangent to the guide, generating a pure torque on the gearbox. Consequently, varying the height relative to the gearbox guide allows the inclination of the rope to be modified with a consequent change

in the direction of force application, thus adding a radial component to the gearbox.

- **The second pulley**

The second pulley, positioned at the height of the test bench floor, sends the rope connected to the 'mover' downwards. The mover will be analysed in detail in the following section.

- **The third and fourth pulleys**

The third and fourth pulleys, as already mentioned, are connected to the same support, positioned below the test bench support surface. The two pulleys pick up the two ropes, previously sent downwards by the other pulleys, in the parallel direction of the test bench support plane but below it. In addition, they give the ropes a 2-degree angle so that the rope can be aligned with the centre in the tubes in which the springs are placed.

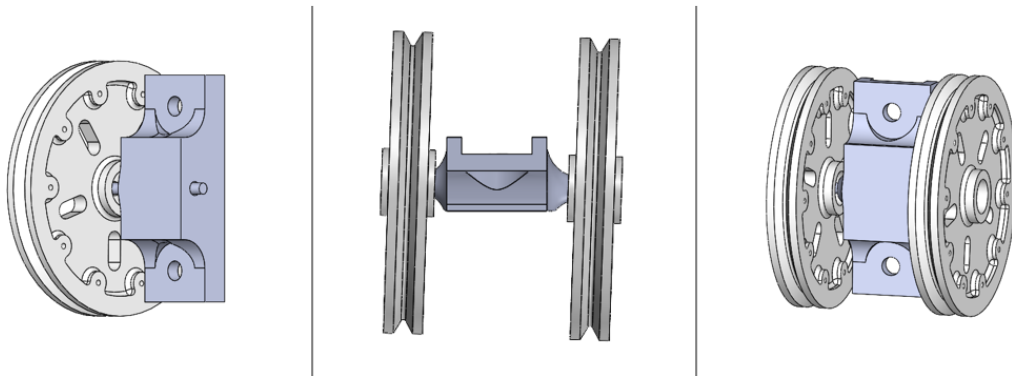


Figure 3.5. Pulley system supports

3.3 Mover

The second subsystem of the load module is the mover, illustrated in the figure 3.6. It is placed to the right of the gearbox and is characterised by the following components:

- A pulley with a smaller diameter than the pulleys installed on the previous subsystem.
- An inclined support for the pulley .
- An M4 threaded rod.
- Two shielded steel ball bearings with an inner diameter of 4 mm and an outer diameter of 13 mm.
- A pair of guides to guarantee the sliding of the support.
- A C-shaped support to secure the subsystem to the end of the test bench.
- An M8 threaded rod.
- A flyer.
- Four M6 hexagon head screws 10 cm long and four M4 screws 1 cm long.

Also in this case, all components were designed in Solidworks and 3D printed using the Fused Deposition Modelling (FDM) technique. All CADs related to the mover components are shown in the appendix A.2.

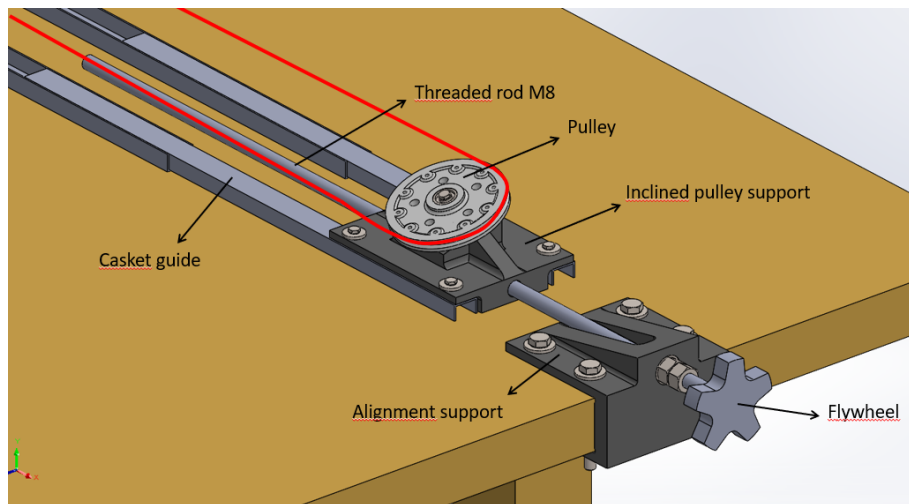


Figure 3.6. Mover

- The main function performed by the mover is to send the rope connected to the second hook of the gearbox, previously rolled around the guide, back to the pulley system. To do this, the rope is sent back from the pulley at an angle of 19 degrees. The inclination is provided by the support to which the pulley is connected via an M4 threaded rod and two shielded bearings, which allow it to rotate around the rod. The inclination is indispensable for returning the rope. In fact, to reach the pulley system, the rope must pass below the braking module and the gearbox. Keeping the pulley in a horizontal position, the rope would be sent back in a direction parallel to the test bench support plane at a height equal to the distance between the guide groove of the gearbox and the test bench support plane. When being sent back towards the pulley system, the rope would have encountered various obstacles, such as the components of the braking module and the gearbox, which would have prevented it from reaching the opposite end of the test bench where the pulley system is located. To solve this problem, it was decided to incline the pulley by providing a tilt to its support. The pulley has a smaller diameter than the others installed on the profile. It can be seen that, if the pulley had been horizontal, its diameter would have been 56.44 mm, given by the distance between the center distance of the second pulley, shown in the figure 3.4, which receives the rope to be sent back and the gearbox guide from which the rope to be sent comes. By inclining it, the diameter of the pulley increases and is equal to this distance divided by the cosine of the angle of inclination of the pulley, the diameter will be 59.6 mm.
- The second function performed by the subsystem is to ensure the linear movement of the pulley placed on the support in a direction parallel to the test bench support plane, from this function derives the name subsystem mover. This movement adds a radial component to the forces applied to the gearbox. The radial component is provided by moving the pulley away from the gearbox, which causes an increase in tension on the rope, which will provide a preload to the spring connected to the tensioned rope, resulting in the emergence of the radial component. In order to move the pulley support closer or further away from the gearbox, it is placed on two guides so that the only degree of freedom of the system is to move in the direction of the

guide. Specifically, these are drawer guides, fixed to the table by means of two screws each. The support, shown in the figure 3.7, is drilled and crossed by an M8 threaded rod 50 cm long, at the end of which is a nut that fits into a special nut-shaped housing of the pulley support. The threaded rod is passed through a C-shaped aligning support fixed to the test bench support surface by means of four M6 screws to hold the rod in position. At the top end is a flyer, the rotation of which is translated into a linear displacement; this is possible because the system is always in tension. Specifically, with a clockwise rotation of the flyer the pulley will move away from the gearbox, loading the spring, while with a counterclockwise rotation the pulley will move closer to the gearbox, unloading the spring.

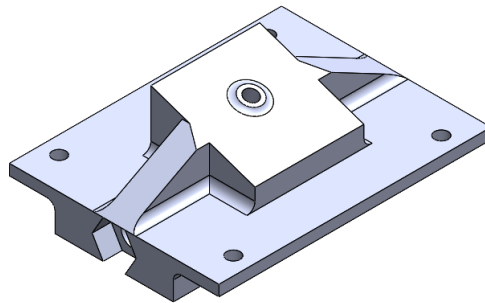


Figure 3.7. Inclined pulley support

3.4 Acquisition system

The acquisition system constitutes the final part of the test bench; it was already present in the test bench but has been modified to allow the connection of two more load cells. The components that make it up are:

- Two HX711 load cells.
- An Arduino UNO board.
- An interface board.

A summary diagram of the acquisition system is shown in the figure 3.8 below. The load cells used can measure a maximum load of up to 20 kg. Before installation, the load cells were appropriately calibrated using a special Arduino programme and calibration weights in the laboratory. The acquisition system performs the function of measuring the spring recall forces from which the torque applied to the gearbox can be derived. The load cells communicate with the Arduino Uno board in which a programme is implemented that can acquire the data from the load cells. Each spring put into traction by the rotation of the gearbox, induced by the motor, will apply a force to the load cells, which will register a voltage variation due to a change in the internal resistance of the strain gauge inside them. This voltage variation will be sent to the Arduino, which will convert the data into a force, communicating it through the serial port to the PC, where a Matlab programme is run to record the values coming from the Arduino, creating a Matlab data file containing the variation of the recall force of each spring over time.

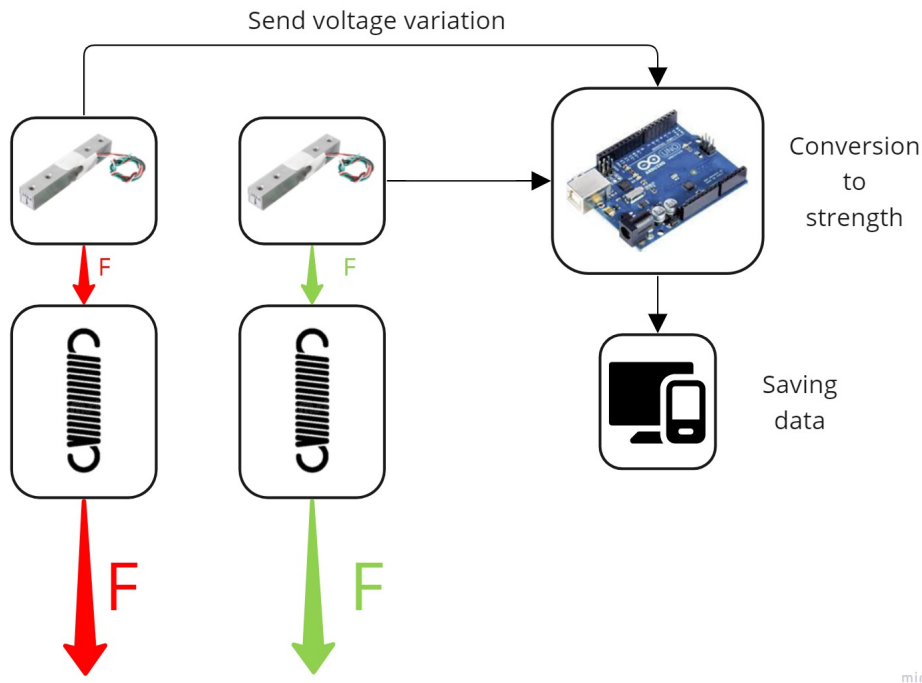


Figure 3.8. Acquisition system scheme

3.5 Complete test bench Overview

The figure 3.9 shows the diagram of the test bench with all three modules installed. In contrast to the figure 2.13, the load module is shown in green.

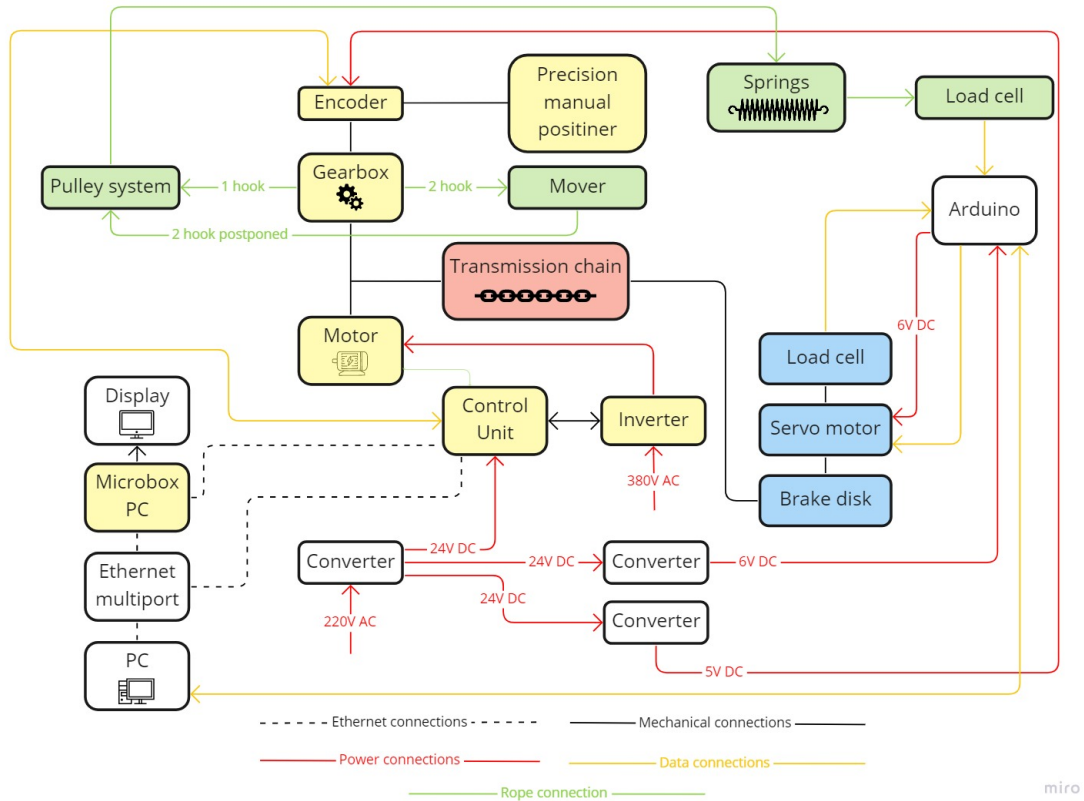


Figure 3.9. Test bench with load module summary diagram

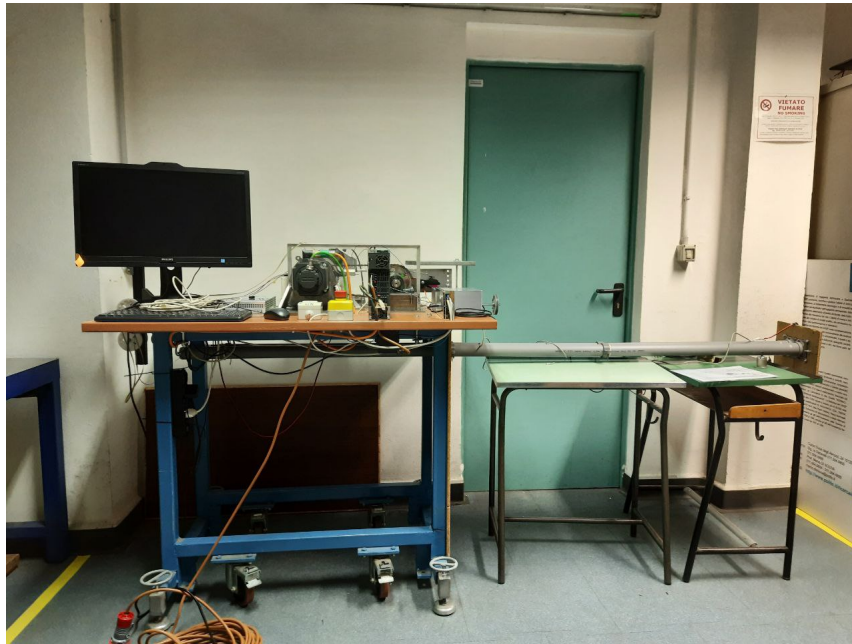


Figure 3.10. Photo of complete test bench



Figure 3.11. Photo of the acquisition system



Figure 3.12. Photo of pulley system

Chapter 4

Springs

Springs are the central element of the load module, allowing the torque to be applied to the gearbox to simulate the effect of an external load on the transmission end. Springs are mechanical elements, capable of absorbing considerable amounts of energy before reaching critical stresses that cause them to break. They are typically used for the following purposes:

- Shock attenuation.
- Reduction or accentuation of vibrations.
- Control of mechanical parts.
- Energy storage.
- Applying proportional forces.

With regard to the development of the load modulus, the choice was made to use springs to generate the torque, exploiting their property of applying a force proportional to their elongation with respect to the equilibrium condition. In particular, the choice fell on tensile coil springs. Tension coil springs consist of several helical coils and have a high resistance to the axial stresses to which they are typically subjected.

4.1 Design

4.1.1 Force applied by single spring

The design started with the maximum applicable torque on the gearbox of 12 Nm as the only design parameter. This value is derived from previous analyses carried out when the gearbox was validated. Knowing the gearbox guide diameter of 0.16 m, and since the torque is generated by the interaction of the return forces produced by the two springs, the maximum return force that can be generated by the single spring without inducing damage to the gearbox is obtained as follows:

$$F_{MAX} = \frac{C_{MAX}}{2r} = 75Nm \quad (4.1)$$

C_{MAX} corresponds to the maximum applicable torque on the gearbox, r to the radius of the gearbox guide and the whole is halved to obtain the contribution of the single spring. For safety reasons, it was decided to increase the force by 7%, considering 80 Nm as the maximum force that can be applied by each individual spring.

4.1.2 Maximum elongation

A second design parameter is the maximum elongation that the spring can generate without entering the plastic field. This parameter corresponds to the difference between the length of the spring in the condition of maximum elongation L_{MAX} and the condition at rest L_0 . Knowing the radius of the gearbox guide r , it is possible to calculate the wire needed to complete one revolution around the gearbox, which corresponds to the circumference of the gearbox guide c .

$$c = 2\pi r = 0.5m \quad (4.2)$$

It was decided to roll the rope a maximum of 2.5 times around the gearbox guide, thus ensuring an adequate wire length for the load module. In fact, a greater elongation allows for a greater window of applicable forces. Hence, the maximum elongation ΔL of the spring corresponds to 1.3 m.

4.1.3 Spring stiffness

Knowing the maximum applicable force F_{MAX} of the individual spring and its maximum elongation ΔL , it is possible to calculate the spring's stiffness K_{design} determined by the following relationship:

$$K_{design} = \frac{F_{MAX}}{\Delta L} = 0.0615 N/mm \quad (4.3)$$

4.1.4 Material

The next step in spring design is to define the geometric characteristics: the wire diameter d and the spring diameter D , which depend on the forces it must withstand and the material chosen. The choice of material is decisive for the design. Steel is the ideal material for spring construction, presenting an elastic deformation without any plastic alteration, which is due to a high yield strength. An increase in the yield strength can be achieved by performing a hardening and tempering treatment on the steel. Hardening and tempering is a heat treatment used to obtain high hardness and strength in steel. It consists of three different processes: austenitising, hardening and tempering, in order to maintain a tempered martensite or bainite structure. Tempering offers several advantages:

- Heavy-loaded parts can achieve an optimal combination of high strength, solidity and, if possible, temperature resistance.
- Such parts may be lighter and stiffer as a result of the increased strength.
- Workpieces requiring grinding with low roughness acquire the desired machinability.

Another indispensable characteristic of a spring steel is high hardenability. The type of grain determines its characteristics. In order to achieve higher elasticity and a high yield strength, spring steels must have a fine grain in order to be less sensitive to overheating. They must also have a high tensile strength and fatigue strength, but the heat treatments required to obtain these characteristics inevitably reduce their toughness. For the design of the spring, *carbon steel - EN 10270-1 class SM* was chosen, which has the following physical properties and chemical composition shown in the tables 4.1 4.2 [1]:

Physical properties	
Density ρ	7.85 Kg/dm ³
Young's module E	206 KN/mm ²
Shear modulus G	81.5 KN/mm ²
Tensile strength σ_R	1630-1830 N/mm ²

Table 4.1. Physical properties

Chemical Composition	
C	0.35-1
Si	0.10-0.30
Mn	0.50-1.20
P	max 0.035
S	max 0.035
Cu	max 0.20

Table 4.2. Chemical Composition

4.1.5 Geometric characteristics

Spring diameter D and wire diameter d

Once the material has been chosen, the stresses and moments to which each individual coil of the spring is subjected are analysed. Specifically, each coil, as shown in the figure 4.1 [4], must resist a normal force F_N , a shear force F_T , a bending moment M_f and a twisting moment M_t , which are calculated through the following relationships:

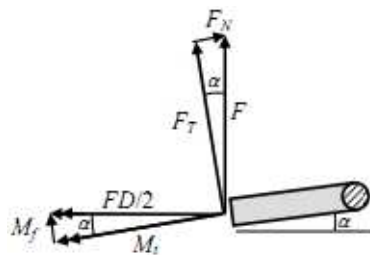


Figure 4.1. Forces on a single coil

$$F_N = F \sin \alpha \quad F_T = F \cos \alpha \quad (4.4)$$

$$M_f = \frac{FD}{2} \sin \alpha \quad M_t = \frac{FD}{2} \cos \alpha \quad (4.5)$$

Assuming we design the spring with all coils in contact, it follows that the pitch between one coil and the next will be equal to half the diameter of the wire, from which the angle of the alpha pitch will be small enough to consider: F_N and M_f null, $F_T = F$ and $M_t = FD/2$. The shear at the most stressed point will be given by the contribution of the shear force and the twisting moment according to the following relationship [19]:

$$\tau = \frac{qFDd}{4I_p} + \frac{F}{A} \quad (4.6)$$

q is the torsion factor for circular cross-sections and I_p is the polar moment of inertia, which for a spring is equal to $I_p = \pi d^4/32$. In our present case, the relationship becomes as follows:

$$\tau = \frac{8FD}{\pi d^3} + \frac{4F}{\pi d^2} \quad (4.7)$$

The Von Mises criterion also known as the maximum energy criterion. As its name implies, it is an energy criterion, with which it is possible to calculate the maximum stresses a material can resist depending on its characteristics before reaching failure or entering the plastic field respectively if we consider the stress at break σ_R or the yield stress $\sigma_{0.2}$ of the material. In our case, by considering the stress at break, it is possible to calculate the maximum shear force the spring can resist before breaking.

$$\sigma_R = \sqrt{\sigma_z + 3\tau} \quad (4.8)$$

Only shear forces and bending moments act on the spring, so the previous equation is simplified as follows:

$$\tau = \frac{\sigma_R}{SF\sqrt{3}} \quad (4.9)$$

To take into account that the quantities involved are not deterministic, the nominal sigma of rupture σ_R is reduced by a factor SF called *safety factor*, in this case set equal to 2. Equalising the maximum tension, equation 4.7 , to the tension obtained from the Von Mises criterion, equation 4.9, we derive the relationship between the external diameter of the spring D and the diameter of the wire d. This relationship establishes the geometric characteristics D and d that enable the spring to resist the forces involved without breaking.

$$D = \frac{\sigma_R \pi d^3}{8\sqrt{3}SF * F} - \frac{d}{2} \quad (4.10)$$

Varying the wire diameter from 2 to 4 mm, typical values taken from the lettering for springs similar to the one we are interested for, produces the following graph in the figure 4.2.

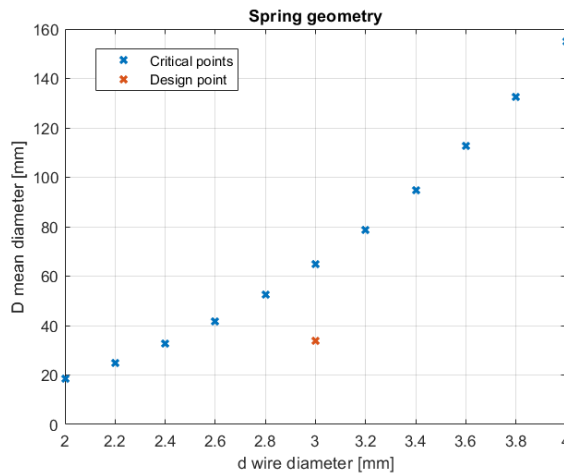


Figure 4.2. Maximum acceptable spring diameter D

The figure 4.2 shows in blue the pairs of critical points, corresponding to the wire diameter d and the spring diameter D. It can be seen that as the wire diameter d increases, the spring diameter increases; this is due to the fact that a thicker wire provides a higher breaking strength, allowing a less compact spring, which corresponds to a larger spring diameter D. All points below the critical points represent acceptable combinations of d and D, the point highlighted in red is the selected one corresponding to:

- Wire diameter d : 3 mm
- Spring diameter D : 34 mm

The spring diameter D is smaller than the critical spring diameter D for a wire with a diameter of 3 mm, which gives the spring greater strength and at the same time not too much encumbrance.

Number of coils n and length of spring at rest ΔL

The last design parameter to be determined is the length of the spring at rest L_0 , which can be calculated as a function of the wire diameter d and the number of coils n according to the following relationship:

$$L_0 = nd \tag{4.11}$$

The only unknown in the equation is the number of coils n of the spring, by setting the deformation energy equal to the work done by the force L_e we obtain the following relationship [19]:

$$K = \frac{Gd^4}{8D^3n} \tag{4.12}$$

Explaining n by inverse formula

$$n = \frac{Gd^4}{8D^3K} \tag{4.13}$$

By varying K from half the design value to twice the design value, where the design resistance value K_{design} has been calculated in the equation 4.3, it is possible to graph the change in the number of coils n and the resulting and rest length of the spring L_0 having fixed the geometric parameters d and D . The figure shows 4.3 in blue the number of coils n as the spring stiffness K varies, given the geometric parameters. It can be seen that for low stiffness values, a very high number of coils is required to guarantee the same geometry. Conversely, as the stiffness increases, the number of coils decreases, which is due to the fact that the spring's stiffness is inversely proportional to the number of coils.

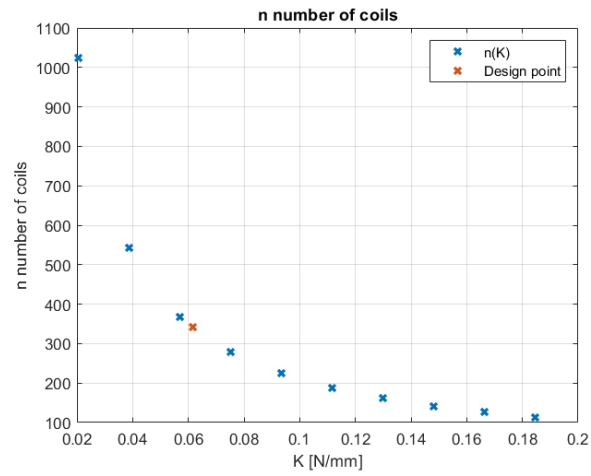


Figure 4.3. Number of turns as a function of spring stiffness

The figure shows 4.4 the length of the spring at rest L_0 as a function of spring stiffness K . The trend is the same as in the previous graph; this is due to the direct proportionality between the number of coils and the length of the spring as expressed in the equation 4.11. The points in red are those corresponding to the previously calculated stiffness coefficient K_{design} of 0.0615 N/mm required to obtain an elongation of 1.3 m by applying a force of 80 N.

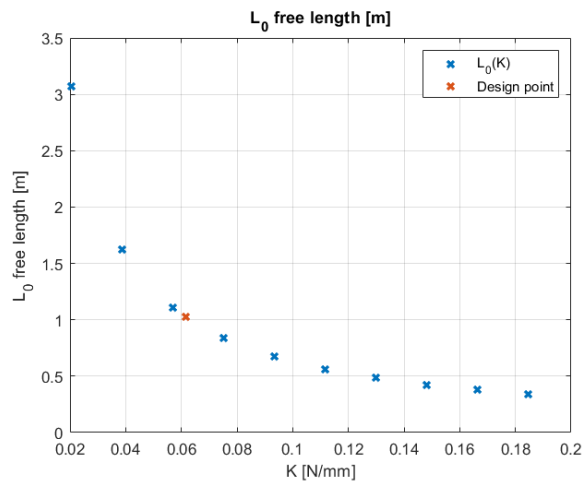


Figure 4.4. Length as a function of spring stiffness

The parameters thus obtained are:

- 342 Number of coils n
- 1.026 m Length of spring at rest L_0

Chapter 5

Optical fibre sensors

A second objective of this thesis is to verify the aerospace application of fibre optics as a sensor for prognostics and system health monitoring. To this end, the load module applies a torque to the gearbox to determine its structural deformations, which will be read by the optical fibre Bragg grating sensors, and by comparing their response with the response provided by more traditional sensors, such as strain gauges, it will be possible to validate their operation. Both types of sensors were installed on the gearbox of the electromechanical actuator reproduced by the test bench as described in the following chapters. Optical fibre sensors represent a new technology that is increasingly appearing in the world of sensors and in particular in the aerospace industry. They find their main application in complex systems, where traditional electrical sensors fail to meet the requirements. This type of sensor makes it possible to measure various physical and/or chemical properties of the materials on which they are installed. Their operating principle is based on the propagation of light within the optical fibre. An external perturbation of a chemical or physical nature can lead to a change in the propagation of light with respect to the nominal conditions, generating a change measurable by the sensor. Compared to more traditional sensor types, fibre optics can offer several advantages [10]:

- Immunity to electromagnetic interference
- The impossibility of conducting electricity

- The possibility of being deployed in hostile environments
- The significantly reduced volume and weight
- The possibility of detection in normally inaccessible places
- The ease of remote control and the possibility of integrating several sensors on the same optical fibre
- The possibility of use in chemical processes and biomedical instrumentation
- High sensitivity and accuracy during detection
- The dual function of transducer and information transport channel, being realised with standard optical fibres and, therefore, compatible with existing optical fibre systems

The use of fibre optics also brings disadvantages:

- They must be installed with high bending radius to avoid signal loss or accidental breakage
- Installation can be very expensive as it requires a team of experts
- Optical fibres are very delicate, requiring protection against mechanical stress

5.1 Structure

The structure of optical fibres, figure 5.1, are filaments of dielectric materials, typically glass or polymers, which allow light to propagate through them with extremely limited power losses. The innermost part is called *core* and has a size usually between 8 and 10 μm , while the outer part is called *cladding* and has a size of about 125 μm . These two parts make up the actual fibre, which would be too fragile and would be likely to break during use or installation. The fibres are coated with an additional structural protection made of synthetic material to ensure greater handling and strength. From a mechanical point of view, the fibre resists well under tensile stress as opposed to shear stress, which is more likely to cause it to break, which is why it is preferable to load it with axial loads.

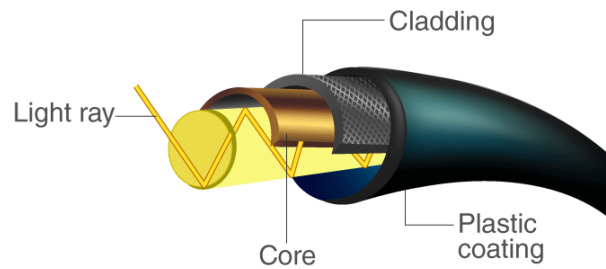


Figure 5.1. Structure of the optical fibre

The electromagnetic wave propagates within the fibre in different propagation modes depending on its geometry. The propagation modes denoted by m correspond to different propagation speeds. Optical fibres can be classified according to the way light propagates and the refractive indices within them:

- **Single-mode**

Light travels along the fibre without any reflection according to the fundamental mode $m=0$, providing a longer bandwidth than multimodal fibres that exploit reflection, which limits bandwidth. They are used for long-distance applications where low losses and high transmission rates are required.

- **Multimodal step-index**

The large diameter of the core has a uniform refractive index, which allows for many modes of propagation. The name step-index is due to the different refractive index of the core and cladding, which is slightly lower.

- **Multimodal with graduated index**

Developed to avoid the modal dispersion that characterises graded-index multimode fibres. The refractive index of the core varies with distance from the centre, while the refractive index of the cladding is kept constant.

As shown in the figure 5.2, light beams of different order in the multimode step-index fibre reach their final position at different times, whereas in the graded-index fibre they are forced to reach the same position at the same time, due to the variation of the refractive index of the core.

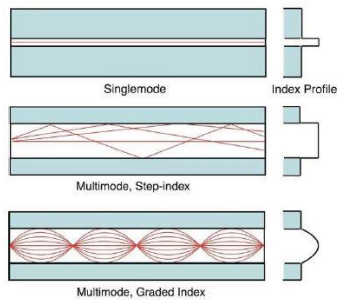


Figure 5.2. Classification of optical fibres

The transmission of the signal in the form of an electromagnetic wave is possible by modifying the refractive index n of the cladding, obtaining a discontinuity surface with respect to the core within which the electromagnetic wave remains confined due to the total reflection phenomenon. Optical fibre sensors use the phenomenon of total internal reflection to transmit the electromagnetic wave inside them. In particular, light rays passing between two surfaces with a refractive index undergo the physical phenomenon described by Snell's law [13]:

$$n_1 \sin \theta_1 = n_2 \sin \theta_2 \quad (5.1)$$

A light wave passing through the separating surface between two materials with refractive indices n_1 and n_2 changes its propagation direction according to the ratio of the refractive indices n of the two materials. If $n_2 > n_1$ the propagation direction approaches the surface normal, conversely the propagation direction moves away from the surface normal. Optic fibre sensors use a special case of Snell's law called total reflection.

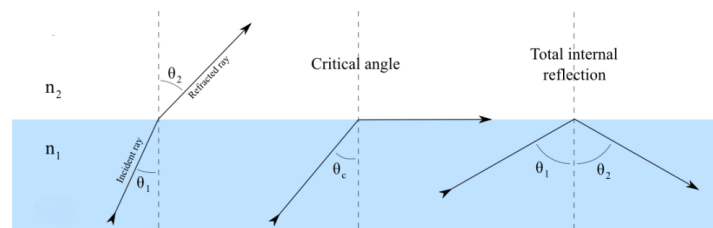


Figure 5.3. L: the phenomenon of refraction with $\theta_1 < \theta_c$; C: the phenomenon of refraction with $\theta_1 = \theta_c$; R: the phenomenon of refraction with $\theta_1 > \theta_c$

There is in fact, as shown in the figure 5.3, a limiting angle at which all light will be reflected, so if the ratio of the two indices of refraction is such that the angle θ_1 is always equal to or greater than θ_c , the phenomenon of total reflection will occur. The occurrence of this condition is essential for the correct functioning of a optical fibre sensor, as it keeps the electromagnetic wave always inside the core so that it can propagate through continuous reflections until it reaches the actual sensor called Fiber Bragg Grating (FBG), which we will discuss in detail later. Considering the light rays transmitted through the optical fibre, the acceptance angle θ_A is defined as the maximum angle of incidence that guarantees the occurrence of the total internal reflection phenomenon. The acceptance angle is calculated from the following relationship.

$$\theta_A = \sqrt{\frac{(n_2 - n_1)^2}{n_0}} \quad (5.2)$$

Where n_0 constitutes the index of refraction of the surface from which the optical beam originates. The set of all possible incident trajectories having an angle less than or equal to the acceptance angle, constitute the acceptance cone shown in the figure below.

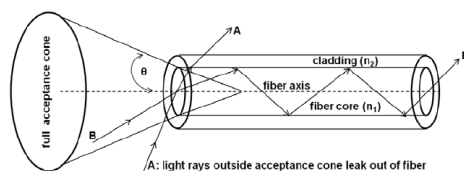


Figure 5.4. optical fibre acceptance cone

The maximum acceptance angle influences the signal losses both at the connection between the fibre and the acquirer and at the soldering areas of the fibre. In fact, in these critical areas, the slightest misalignment in the core of the two fibre portions generates disturbances in the signal which, if very pronounced, can compromise the entire sensor. Another type of signal loss can be generated by too small a bend radius, which results in a smaller angle of incidence than the critical one, causing a loss of power. For this reason, the fibre must be positioned during the installation phase so as not to create too sharp bends.

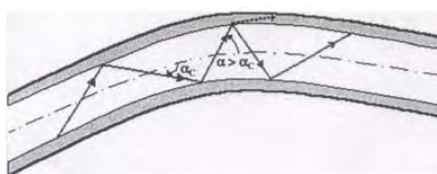


Figure 5.5. Effect of excessive optical fibre curvature

5.2 Fiber Bragg Grating FBG

The optical fibre is modified by inserting Fibre Bragg Grating FBG, a microstructure built into the core. Using a UV laser, the refractive index of a part of the optical fibre is permanently increased, producing a modulation according to the exposure pattern. The variation of the latter along the optical fibre opening produces a grating. The Fibre Bragg Grating will act as a filter by selecting specific wavelengths. The electromagnetic wave travelling within the core will be partially reflected at the refractive index changes. The maximum reflection will occur at the Bragg wavelength λ_B , which can be derived from the *fundamental Bragg equation*.

$$\lambda_B = 2n_{eff}\Lambda \quad (5.3)$$

This relationship links the effective refractive index n_{eff} with the fringe period Λ . Light rays add an additive contribution only for those wavelengths related to the grating pitch and a particular index of refraction. Hence, any change in the chemical or physical properties of the grating will lead to a change in the Bragg wavelength. The sensor allows the wavelengths distant from the Bragg wavelength to pass through, sending only those close to the Bragg wavelength back to the acquirer. As can be seen from the figure below 5.6, a change in the grating distance results in a change in the selected wavelength.

Therefore, by using different wavelengths, several FBG can be placed on the same optical fibre. Each FBG must be sufficiently distant from the next and characterised by different Bragg wavelengths. The maximum number of FBG that can be installed on a single fibre depends on the bandwidth that the generated laser of the acquirer is able to emit. Furthermore, the more accurate the acquirer is in determining the Bragg wavelength of each individual FBG, the more accurate

the sensor will be. Hence, the intensity of the sensor response depends on the length of the Bragg grating and thus on the number of refractive index variations within the grating. A second variable is the fringe spacing, which can be uniform or chirped.

- **Uniform fringe spacing**

Used in the optical fibres employed in this thesis, there is a constant distance between the interface fringes, so that only one wavelength is reflected, resulting in a narrow, symmetrical spectrum corresponding to the Bragg wavelength.

- **Chirped**

In contrast, chirped gratings have a different spacing between fringes and a change in the refractive index of the core, resulting in a broader reflection spectrum since reflection does not occur for a single wavelength.

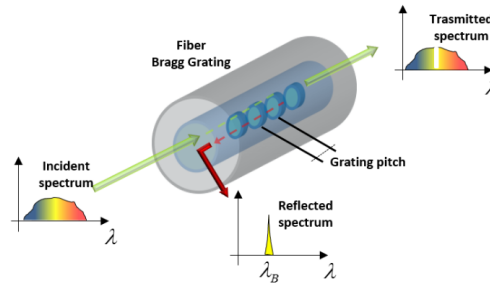


Figure 5.6. Bragg grating FBG

5.3 Photo-Thermal-Elastic Equation

Let's look in detail at the relationships that characterise optical fibres sensors with Bragg gratings. By differentiating the fundamental Bragg equation 5.3, the wavelength variation can be written as follows:

$$\frac{\Delta\lambda_B}{\lambda_B} = \frac{\Delta\Lambda}{\lambda} + \frac{\Delta n_{eff}}{n_{eff}} = \epsilon_1 + \frac{\Delta n_{eff}}{n_{eff}} \quad (5.4)$$

Where Δn_{eff} and $\Delta\Lambda$ represent respectively the variation of the effective refractive index and the variation in the pitch of the grating fringes, while ϵ_1 corresponds to the deformation undergone by the fibre along its main axis. It is possible to write the previous equation as the sum of three contributions:

$$\Delta\lambda_B = \Delta\lambda_B^\Lambda + \Delta\lambda_B^T + \Delta\lambda_B^\sigma \quad (5.5)$$

Analysing each contribution specifically:

- $\Delta\lambda_B^\Lambda$: the first term is the contribution given by the variation of the pitch between the fringes of the grating. Specifically it can be written as:

$$\Delta\lambda_B^\Lambda = \lambda_b \epsilon_1 = \lambda_b (\epsilon_1^\alpha + \epsilon_1^\sigma) = \lambda_b (\alpha \Delta T + \epsilon_1^\sigma) \quad (5.6)$$

ϵ is divided into two contributions the first ϵ_1^α due to thermal expansion the second ϵ_1^σ to applied stresses. A new term α appears, which corresponds to the coefficient of thermal expansion of the fibre.

- $\Delta\lambda_B^T$: Variation in the wavelength of the grating due to changes in the refractive index induced by thermal stress. This contribution can be rewritten as:

$$\Delta\lambda_B^T = \lambda_B \left(\frac{1}{n_{eff}} \frac{dn}{dT} \right) \quad (5.7)$$

- $\Delta\lambda_B^\sigma$: Variation in the wavelength of the grating due to changes in the refractive index induced by mechanical stress. This contribution can be rewritten as:

$$\Delta\lambda_B^\sigma = -\lambda_B \frac{n^2}{2} [p_{12}\epsilon_1 + (p_{11} + p_{12})\epsilon_2] \quad (5.8)$$

In particular, it is possible to rewrite the effective refractive index variation Δn_{eff} as:

$$\Delta n_{eff} = -\frac{n_{eff}^3}{2} [p_{12}\epsilon_1 + (p_{11} + p_{12})\epsilon_2 - \frac{2}{n_{eff}^3} \frac{dn}{dT} \Delta T] \quad (5.9)$$

The coefficients p_{11} and p_{12} are called the Pockel coefficients of the opto-elastic tensor and ϵ_2 and the sensor strain along the radial direction of the fibre. Substituting the three contributions yields the *photo-thermal elastic equation*:

$$\Delta\lambda_B = \lambda_B(\epsilon_1 - \frac{n_{eff}^2}{2}(p_{12}\epsilon_1 + (p_{11} + p_{12})\epsilon_2)) + \lambda_B(\alpha + \frac{1}{n_{eff}} \frac{dn}{dT})\Delta T \quad (5.10)$$

the equation is simplified by introducing the following constants:

- Photo-electric constant

$$p_e = \frac{n^2}{2}(p_{12} - \nu(p_{11} + p_{12})) \quad (5.11)$$

- Thermo-optical constant

$$\zeta = \frac{1}{n_{eff}} \frac{dn}{dT} \quad (5.12)$$

The photo-thermal elastic bond becomes:

$$\Delta\lambda_B = \lambda_B(1 - p_e)\epsilon_1 + \lambda_B(\alpha + \zeta)\Delta T \quad (5.13)$$

Through the introduction of two proportionality constants it becomes:

$$\Delta\lambda_B = K_\epsilon\epsilon + K_T\Delta T \quad (5.14)$$

It can be seen that the wavelength variation $\Delta\lambda_B$ of the Bragg grating is influenced by the mechanical strain ϵ and the thermal variation ΔT , so it follows that using this relationship it is possible, knowing the two constants, to use optical fibres as sensors to calculate the temperature variation or the mechanical strain through the inverse formula of the equation.

5.4 Interrogator

The acquisition system that allows the electromagnetic wave to be injected inside the fibre core and at the same time detect the wave reflected by the FBG gratings, which are present inside the optical fibre, through a spectrum analysis for peak monitoring is the optical interrogator. Depending on the light source, we can distinguish interrogators into two types, optical broadband interrogators and tunable laser optical interrogators:

- **Optical broadband interrogators**

These interrogators use a superluminescent LED called SLED, which emits a light signal through an optical circulator into the optical fibre containing the FBG. The optical circulator directs the signal reflected by the FBG into an optical bandpass filter that splits the spectrum components. Below the filter is a photodiode connected in turn to a transimpedance amplifier that covers the current proportional to the optical power at a given wavelength in analogue voltage. The analogue signal thus obtained is converted to digital to be stored or displayed in real time.

- **Optical laser tunable interrogators**

These interrogators have a variable wavelength within the spectrum. Unlike the previous ones, the electromagnetic wave, generally a laser is used, has a much narrower band so as to break up the wavelength range. This choice eliminates the need to filter the reflected signal, allowing it to be sent directly to the photodiode, connected as in the previous case to the transimpedance amplifier, which generates an analogue voltage signal that is converted into a digital signal by the converter.



Figure 5.7. SmasrtScan interrogator

Tunable laser interrogators have a very high signal-to-noise ratio, which is due to the fact that whatever the wavelength of interest, the source will always present maximum intensity. This thesis used the SmasrtScan interrogator produced by

Smartfibers, shown in the figure 5.7. SmartScan is an ultra-compact and robust interrogator for dynamic measurement of FBG sensors. This wavelength division multiplexing WDM instrument is based on an agile, tuneable laser source that enables high resolution interrogation at multi kHz frequencies. The high frequency scan rates allow oversampling and averaging to give extraordinary resolution. The following tables 5.1 and 5.2 show the characteristics of the interrogator [3]:

Measurement and Processing	
Wavelength Range	40 nm (1528 – 1568 nm)
Number of Optical Channels	4
Maximum Number of Sensors/Channel	16
Scan Frequency (all sensors active)	2.5 kHz
Max Scan Frequency (reduced wavelength)	25 kHz
Repeatability/Channel	< 1 pm
Wavelength Stability	< 5 pm over $T_{operative}$ range
Dynamic Range (optical attenuation NO loss)	27 dB
Dynamic Range (laser launch power minus)	37 dB
Gain Control	9 levels
Onboard Processing	For conversion and interface
Bragg Grating Full Width Half Maximum	Min > 0.2 nm

Table 5.1. Measurement and Processing

Mechanical, Environmental and Electrical	
Dimensions	140 x 115 x 85 mm
Weight	0.9 kg
Operating Temperature $T_{operative}$	-15 to +55 °C
Optional Increased Temperature Range	-20 to +60 °C
Comms Interface	Ethernet (UDP-IP)
Data Connector	< RJ45 standard
Data Logging (optional)	< To USB memory device
Power Connector	via mains adapter supplied
Optical Connector	FC/APC
Input Voltage	+9 to +36 VDC
Power Consumption	typ 7.5 W, max 8.5 W
EMC Certification	Per BS EN 61326 edition 2006

Table 5.2. Mechanical, Environmental and Electrical

Chapter 6

Optical fibre installation

6.1 Choice of installation point

The best way to choose the place to install a sensor is to previously carry out FEM structural analyses, identifying the most stressed areas of the component depending on the applied load. These zones will correspond to the points with the greatest deformations and thus the best point to position the sensor.

The gearbox, on which we want to install the sensors, being produced using the Fused Deposition Modelling (FDM) technique will be neither orthotropic nor isotropic. The high structural complexity of the gearbox makes an FEM structural analysis too difficult, which is why the installation point was chosen without the possibility of preliminary structural data.

The figure 6.1 shows the vertical view and the top view of the gearbox, red X's indicate the points where the FBG sensors have been placed within the optical fibre. The choice of installation points was not random. These four points, symmetrical to each other, were chosen because they correspond to the points at which the vicular reactions due to the torque generated by the springs are discharged onto the support to which the gearbox is fixed. Consequently, it is precisely at these points that the greatest forces and deformations will occur. At the same time, it is important to avoid placing the FBG Bragg grating too close to the screw; in fact, the screw hole could affect the deformations detected by the sensor and compromise the results.

A second reason for choosing these installation points is due to the geometry of the chosen point itself. Optical fibres are normally mounted on flat surfaces that guarantee easier installation and an optimal operating environment by working only in tension. In this case, we specifically wanted to install them on a concave surface in order to be able to evaluate their response, in particular by observing their operation when subjected to compression and not only to tension. The downside of installing the fibres on such a surface is that it will not be possible to use traditional installation procedures, but a procedure specifically created for the gearbox under consideration was used.

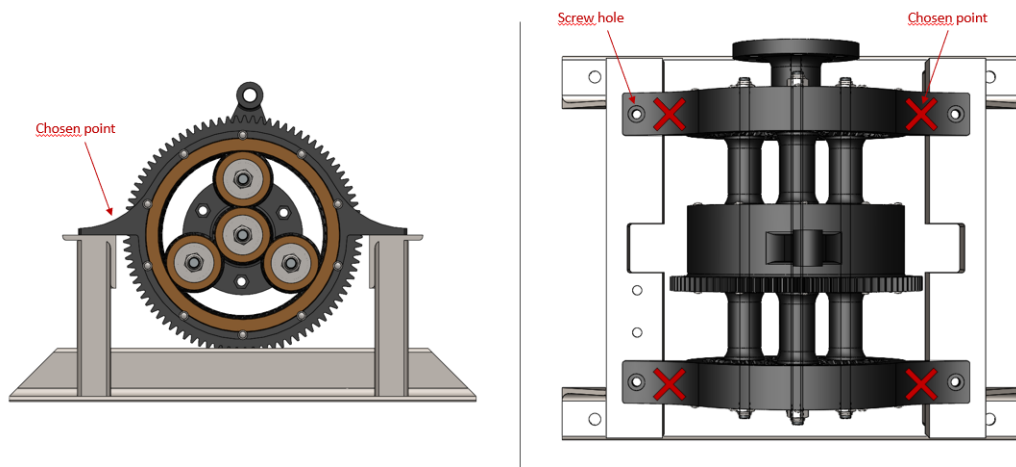


Figure 6.1. FBG installation point

6.2 Installation procedure for optical fibres

Before discussing the fibre installation procedure, it is necessary to analyse the preparation phase. The fibre as produced by the manufacturer is still too fragile, so it has been strengthened by means of a heat-shrink, which will not cover the entire optical fibre but only the part that goes from the connector to the beginning of the gearbox support. The heat-shrink will increase the mechanical strength and manageability of the fibre, in the section that would otherwise have remained uncovered, preventing accidental breakage.

As the fibres were too long, they were shortened by making a cut so that the end of the fibre coincides with the end of the gearbox support.

The conventional installation procedure involves fixing the optical fibre at one end to the specimen, typically a flat or similar surface. The optical fibre is placed in traction by means of a linear mover, the initial traction serves to prevent the fibre from working in a compressive field in fact if accurately pre-tensioned a compression will result in a reduction in tension, pre-tensioning simply causes the fibre to work in a tensile field.

Due to the complexity of the surface of the gearbox, it is not possible to use a mover to pull it, given the large size, and if the fibre is placed in tension it will tend to detach from the surface. For this reason, the negative of the concave surface shown in the figure 6.2 was designed in Solidworks and printed using the Fused Deposition Modelling (FDM). It can be seen that the negative has a curvature equal to the concave surface of the gearbox and a hole to allow the passage of the screw securing the gearbox to its support during fibre installation. In addition, it has a triangular structure to facilitate the operator's grip and allow him to apply the correct pressure. The underside has channels where the fibre is to be inserted to reduce shear stresses, which are the most critical and could lead to fibre breakage.



Figure 6.2. CAD of the gearbox negative

The procedure developed for mounting optical fibres with a Bragg grating on the gearbox of an electromechanical servomechanism includes the following 9 points:

1. Cleaning the installation surface

Properly clean the surface prepared for bonding in order to remove dust, debris and plastic fragments that make the surface uneven. These could affect the accuracy of the results or if large in size stress the fibre in shear.

2. Interrogator connection and sensor function check

Connect the fibre to the interrogator via the connector and the interrogator to the PC via Ethernet cable. Check the correct functioning of the FBG Bragg grating through the SmatFiber software.

3. Fixing optical fibre ends

Glue the end of the fibre to the gearbox at the point shown in the figure 6.3 using a cyanoacrylate-based glue. Wait for 60 seconds. To speed up the waiting time required for the cyanoacrylate to cure, an accelerator was used.

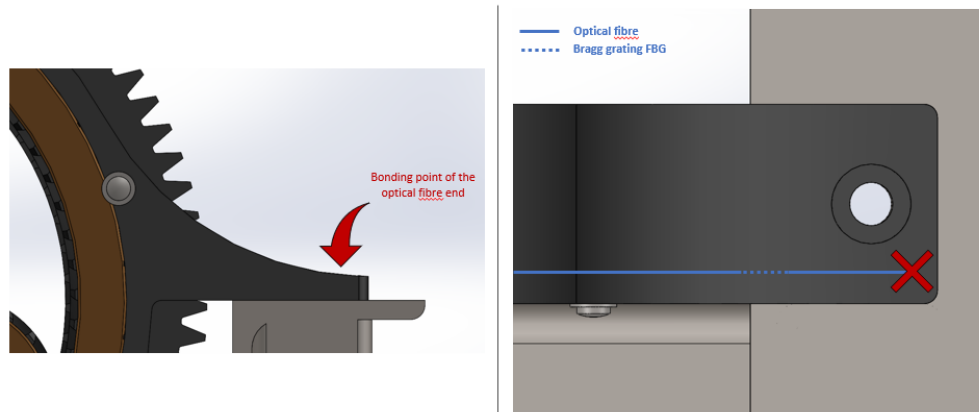


Figure 6.3. First glue point of application

4. Preparation of negative

Preparation of the negative by using an interface material between the gearbox surface and the negative contact surface. This interface surface does not guarantee the adhesion of the cyanoacrylate, allowing the necessary pressure to be exerted on the gearbox through the negative without the latter sticking to the gearbox. Thus allowing the separation of the two components.

5. Pretensioning the optical fibre

Manual pre-tensioning of the optical fibre. This operation is very delicate as the operator must apply force exclusively in an axial way, trying to avoid the generation of shear stresses that can lead to fibre breakage.

6. Tension evaluation

Real-time evaluation of the tension applied to the fibre by comparing the nominal λ_B of the Bragg grating with the wavelength value λ_B^* displayed on the PC through the interrogator. Continue tensioning until the fibre is tensioned to 2 nm. Tension T must be maintained until the end of the installation phase.

7. Glue arrangement

Arrangement of the cyanoacrylate glue on the gearbox surface at the point chosen for the FBG Bragg grating.

8. Pressure application

Application of the accelerant on the interface surface on the negative of the gearbox to speed up the curing of the cyanoacrylate and simultaneous application of pressure P on the fibre through the negative of the gearbox so that the Bragg grating is completely immersed in the cyanoacrylate layer and in contact with the concave surface of the gearbox. The procedure is schematically illustrated in the figure 6.4 and must be maintained for about 5 minutes to be sure that the glue is actually dry.

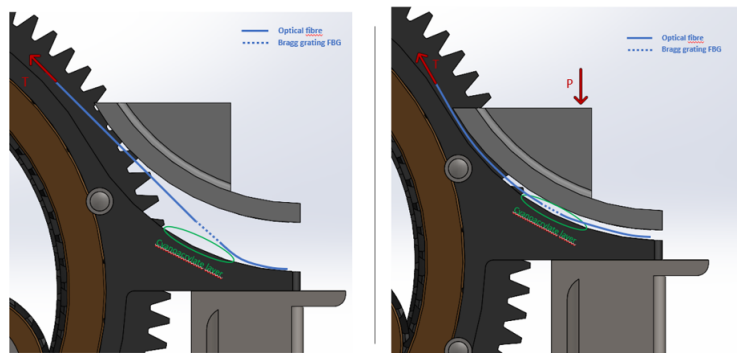


Figure 6.4. Adhesion of the optical fibre to the gearbox surface

9. Removing the negative

Removing the negative of the reducer from the surface and verifying the effective operation of the Bragg grating.

For all four installed Bragg gratings, one for each mounting point of the gearbox on the holder, the installation procedure just described was performed. The four sensors are mounted on three different optical fibres, two having a single Bragg grating per fibre and the third having two Bragg gratings 24 cm apart. The choice stems from the possibility to compare the operation of the fibre with two Bragg gratings with the other two having only one grating per fibre. The figure 6.5 shows the gearbox with the optical fibres installed, in the picture you can also see the strain gauges, which will be discussed in the next chapter.

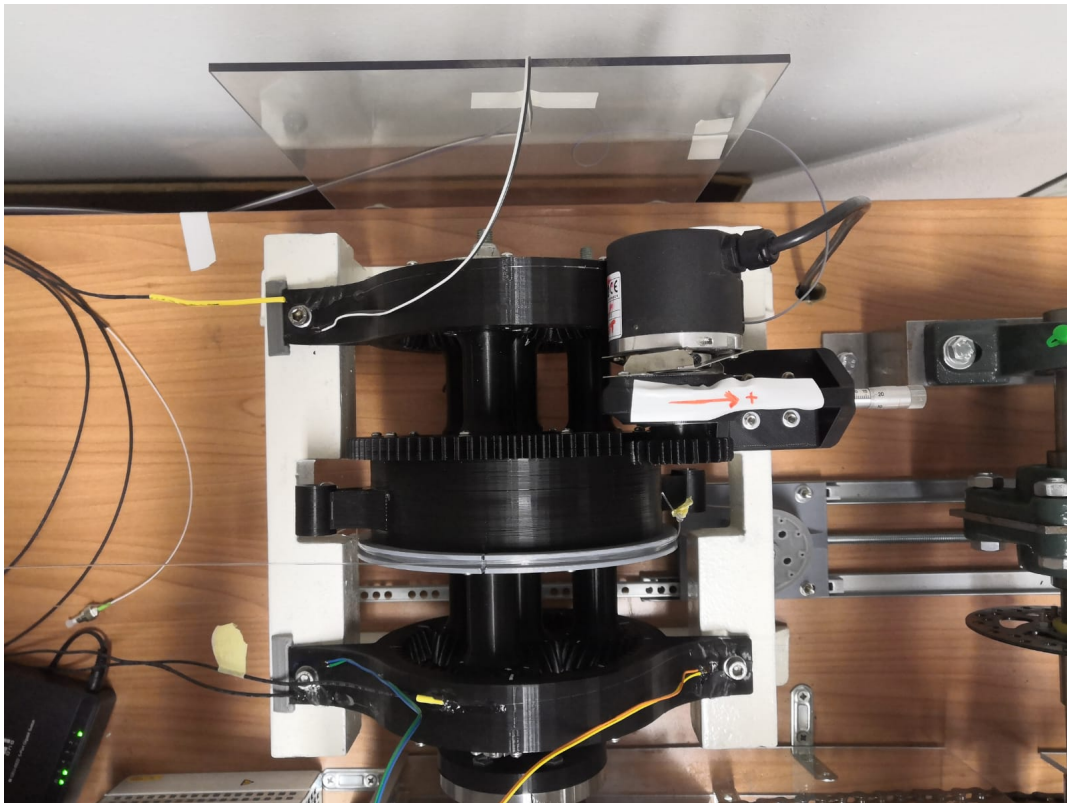


Figure 6.5. Top view of the gearbox with optical fibres installed

6.3 Installation problems

The installation procedure brings with it several problems due to the tensioning and fragility of the optical fibres. Not all installed Bragg gratings show the same pre-tensioning, some are not pre-tensioned at all. This is not due to an ineffective procedure, but to the adhesion of the fibre to the gearbox surface and the curing of the cyanoacrylate glue. The figure 6.6 shows the graph of the wavelength variation of the fibre during the installation phase.

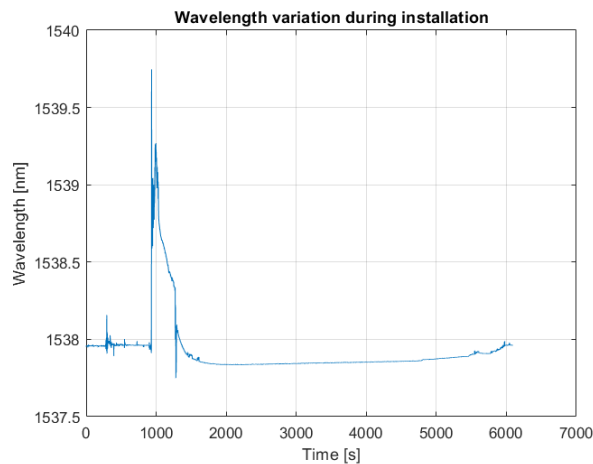


Figure 6.6. Wavelength variation during installation

The graph shows the installation of one of the fibres in which the procedure brought the worst results with almost no pre-tensioning. It can be seen that there is a peak due to manual tensioning, which causes the wavelength to have a delta of about 2 nm. After 300 seconds, there is a rapid decay in wavelength due to the release of the fibre by the operator. From this point onwards, the wavelength tends to decrease over time until it settles at a new value. This is due to the curing phase of the glue, which is not yet completely solidified and does not keep the fibre in the desired position, resulting in a loss of tension. This problem can be overcome by using a glue with a shorter curing time, which will guarantee a more effective retention of the tension provided manually by the operator.

Chapter 7

Strain gauge installation

7.1 Structure of the strain gauge

The second type of sensor installed on the concave surface of the gearbox are strain gauges, which are required to validate the use of optical fibre Bragg gratings as sensors. The strain gauge is glued to the surface of a component whose deformations are to be monitored; the measurement is made through a change in electrical resistance, proportional to the deformations, measured by a computer. The strain response is instantaneous, which allows the strain gauge to be used in both static and dynamic fields, and to analyse frequencies even higher than thousands of Hertz.

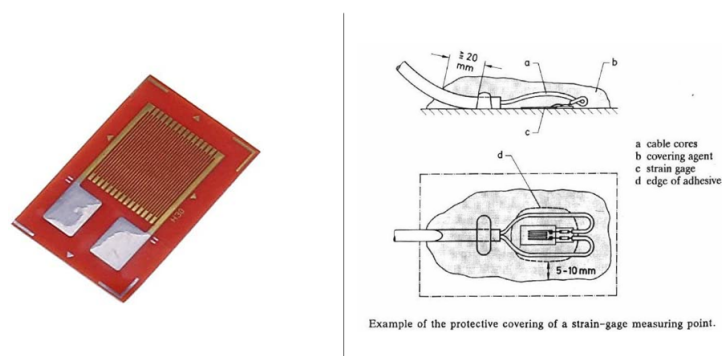


Figure 7.1. Photos and structure of the strain gauge [14]

The structure of the strain gauge, shown in the figure 7.1, is characterised by a grid of laminated metal glued onto a support of polymeric material. The grid ends with two terminals called pads, which allow communication with the computer by means of cables specially soldered to the pads.

7.2 Strain gauge operation

The functioning of the strain gauge can be explained through two different relationships, the first linking electrical resistance to strain and the second linking the change in electrical resistance to the voltage that will then be read by the computer.

7.2.1 Strain-to-resistance relationship

Subjecting a threadlike conductor, such as the strain gauge laminate, to tensile stress results in an increase in its electrical resistance proportional to the force applied, which is dependent on the following relationship:

$$R = \frac{\rho l}{A} \quad (7.1)$$

ρ is the resistivity of the material, l the length of the conductor and A the cross-sectional area. Differentiating the previous equation gives:

$$\frac{\Delta R}{R} = \frac{\Delta \rho}{\rho} + \frac{\Delta l}{l} - \frac{\Delta A}{A} \quad (7.2)$$

Considering a conductor with a square cross-section:

$$\frac{\Delta A}{A} = 2\epsilon_t \quad (7.3)$$

For a conductor subjected to a uniaxial stress state, stressed only in the longitudinal direction, the transverse strain ϵ_t can be rewritten as a function of the Poisson modulus ν and the longitudinal strain ϵ_l . From these considerations, substituting the above equation:

$$\frac{\Delta A}{A} = -2\nu\epsilon_l \quad (7.4)$$

Substituting this result into the equation 7.2:

$$\frac{\Delta R}{R} = \frac{\Delta\rho}{\rho} + (1 + 2\nu)\epsilon_l \quad (7.5)$$

The equation shows that by making the strain gauge integral with the surface, it is possible to relate the strain to the change in relative resistance.

7.2.2 Electrical resistance voltage relationship

In order to be able to read the small variations in resistance of the strain gauge, it is necessary to use a circuit capable of amplifying the signal; the simplest circuit that performs this task is the Whearstone bridge shown in the figure 7.2:

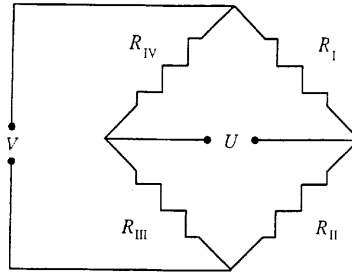


Figure 7.2. Whearstone bridge

This circuit, by reading the potential difference called, unbalance U , allows the resistance change to be measured. In particular for strain gauges with a calibration factor K , the link between unbalance U and supply voltage V is defined by:

$$U = V \frac{K}{4} \epsilon_{tot} \quad (7.6)$$

We can distinguish three different cases:

- U imbalance is zero the bridge is in equilibrium, there are no defomations
- U imbalance is doubled, there are two equal deformations on the opposite lines

- The signal is null, there are two equal deformations on adjacent lines

The signal provided by the bridge is very low because the deformations do not induce a high resistance change. To be read by the acquisition system, it must be amplified.

7.2.3 Gage factor

Typically, the sensitivity of the sensor is $1 \frac{\mu m}{m}$. There is a parameter, called the Gage factor, which allows the sensitivity of the strain gauge to be expressed by relating the relative change in resistance to the strain value

$$GF = \frac{\Delta R/R}{\Delta l/l} \quad (7.7)$$

The gage factor depends on the strain gauge material, typically having a value between 2 and 4.

7.3 Installation procedure for strain gauges

Unlike fibre optics, strain gauges can be mounted on the concave surface of the gearbox using the traditional installation technique, which involves the following 9 points:

1. Cleaning the gearbox surface chosen for installation.
2. Take the strain gauge out of the package using tweezers and place it on the tape.
3. Place the tape with the strain gauge of the chosen position on the gearbox surface.
4. Lift half of the adhesive tape until the strain gauge rotates 180 degrees and place the cyanoacrylate glue on the back of the strain gauge.
5. Apply light pressure to the strain gauge to allow adhesion to the surface. Hold the position long enough for the glue to set.

6. Cleaning the extensometer terminals.
7. Soldering of cables to the strain gauge terminals using a tin-based alloy.
8. Application of a polyurethane-based protective coating to make the strain gauge and the wires soldered to the terminals more resistant.
9. Connection of cables to the port required for the strain gauge to communicate with the computer.

The choice of strain gauge positioning is strongly influenced by the previous choice made for fibre optics. To obtain the same measurement with both strain gauges and optical fibres, in order to be able to compare the result, the two sensors must be mounted in the same place. Ideally, the best choice would be to place them one on top of the other, but as the optical fibre is immersed inside the cyanoacrylate-based glue, installing the strain gauge on top of this would have led to an error in the results due to the fouling of the strain gauges generated by the glue state underneath. For this reason, it was decided, as shown in the figure 7.3, to position the strain gauges on the same transverse axis as the optical fibres in order to obtain more comparable results.

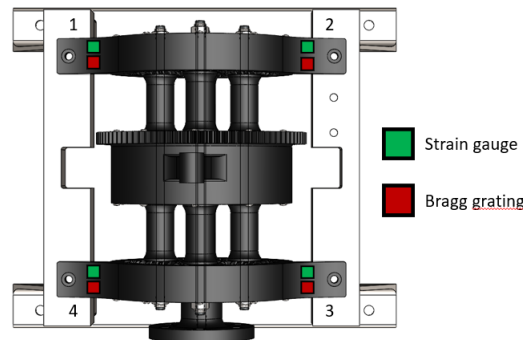


Figure 7.3. Installation point for optical fibres and strain gauges

Unfortunately, it was not possible in all cases to install the strain gauges in the ideal position. In fact, strain gauge 3 was positioned closer to the screw hole, which was a compulsory choice as there is a layer of glue in the optimum position, which would have compromised the results more. Strain gauge 2 was also installed on

a different transverse axis, specifically lower down, than the corresponding Bragg grating, due to a procedural error. For these reasons, strain gauges 2 and 3 do not provide as accurate data as strain gauges 1 and 4, which will be discussed in more detail in the chapter on the analysis of the results. The figures 7.4 and 7.5 show the installation locations of the strain gauges and Bragg gratings.

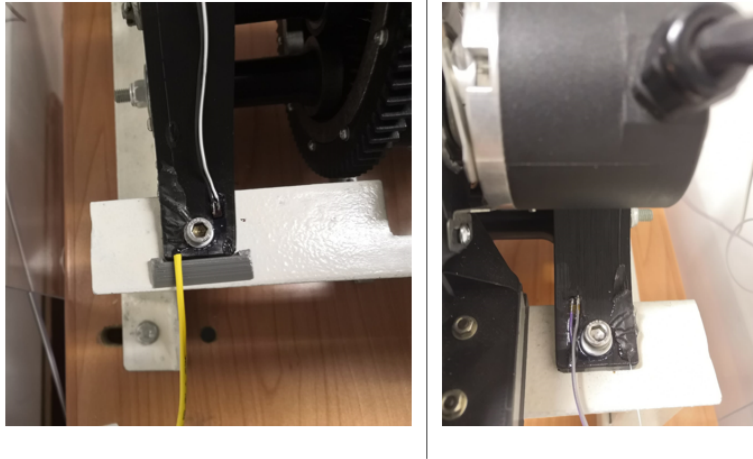


Figure 7.4. Photo Optical Fibre and Strain Gauge 1 and 2

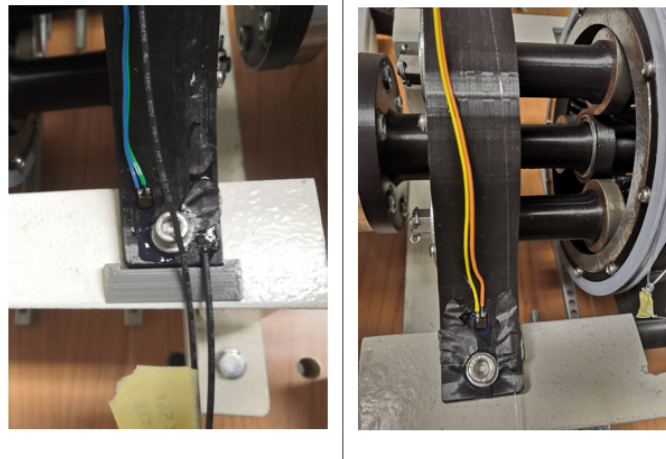


Figure 7.5. Photo Optical Fibre and Strain Gauge 3 and 4

Chapter 8

Trials carried out

8.1 Load module validation tests

The motor installed on the test bench is capable of following different commands, starting with the simplest commands such as a step, passing through more complex commands such as a ramp or a sinusoidal signal, up to a complete customisation of the command by establishing 31 characteristic points that form the signal to be followed. In order to verify the correct operation of the load module, which must be able to apply a torque to the gearbox that is proportional to the rotation controlled by the motor on the gearbox itself, a series of six step commands were applied. The figure 8.1 shows in sequence the commands given for the different tests:

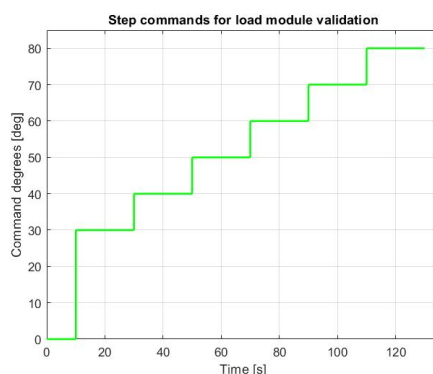


Figure 8.1. Steps carried out in the six tests for load module validation

As can be seen from the graph, each test, which is characterised by a single command, involves a step lasting 20 seconds. In particular, the first step has an amplitude of 30 degrees and the next five have a constant amplitude of 10 deg, so starting from a reference position chosen as zero, the sum of the six tests led to a final position of 80 deg. In order to validate the load module, a large number of points is required, which is why the set of six tests was repeated three times.

8.2 Tests for the evaluation of optical fibres

Subsequently, tests were carried out with the optical fibre sensors with Bragg grating and the strain gauges installed on the gearbox in order to obtain the data required to evaluate the operation of the optical fibre as a prognostic type sensor. In particular, it was decided to carry out a series of six steps with different amplitudes, increasing the amplitude between one command and the next by 10 deg, so starting from a first step with an amplitude of 30 deg, a maximum step of 80 deg was reached. The figure 8.2 shows in sequence the commands given for the different tests.

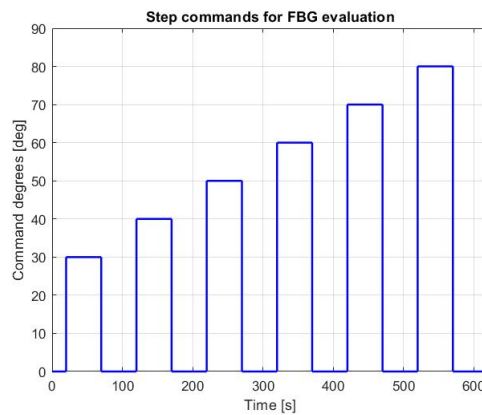


Figure 8.2. Steps carried out in the six tests for FBG evaluation

Each test is characterised by an initial phase known as the load phase, in which a positive step command is imposed on the motor which induces a rotation in the gearbox, resulting in an increase in tension in the load module caused by the springs deviating from their equilibrium condition, thus allowing torque to be

applied to the gearbox. This condition is maintained for an interval long enough for the oscillations caused by the transient to stabilise. The second phase of the control is known as the unloading phase, in which a step of the same amplitude as the load phase is imposed but with the opposite sign. This returns the load modulus to its initial equilibrium condition, ready to perform the next test. This procedure is repeated for each test.

8.3 Procedure for performing tests

Having chosen the type of command to be given to the motor, everything necessary to carry out the tests was established. In this sub-chapter, the procedure carried out for FBG evaluation will be analysed because it is the most complete and complex. In contrast to the validation of the load module, which only involves the acquisition of load cell data and the application of the step command as explained in points 5 and 11 of the data acquisition procedure below.

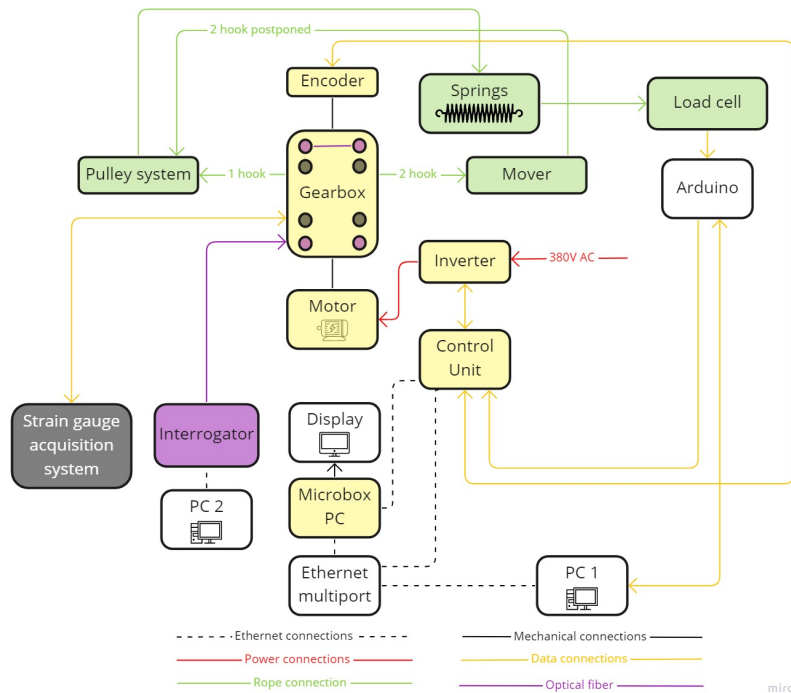


Figure 8.3. Schematisation of components used during tests

The figure shows 8.3 a simplified test bench diagram in which the components not used in the tests, such as the micro-mover for imparting backlash on the gearbox teeth and the braking module, have been eliminated. Since no internal friction phenomenon is applied in these tests. Instead, some components such as the converter were not included to streamline the scheme.

Strain gauges are shown in grey and the optical fibres in purple. In particular, it can be seen that in the optical fibres at the rear of the gearbox, the Bragg gratings are connected to each other as part of a single optical fibre, unlike the remaining two, which are installed on two separate optical fibres. The two acquisition systems the interrogator and the control unit are present to acquire the strain gauge and fibre optic data respectively. In addition, it can be seen that there are two PCs, PC1 connected to the Arduino and the multi-port Ethernet which allows commands to be given through an Ethernet connection and data to be read from the Arduino through the serial port. While PC2 allows the data supplied by the interrogator to be acquired through an Ethernet connection.

The test execution procedure was divided into two stages, the first of which consisted of six steps to prepare the test bench and the second of which involved data acquisition consisting of twelve steps.

8.3.1 Preparation of the test bench

Before carrying out the test, the test bench must be prepared by connecting all components with the appropriate connections and supplying power to the bench:

1. Power on the Microbox PC PLC and CU control unit.
2. Power supply of the test bench through a three-phase 380V current.
3. Connection of PC1 to the multi Ethernet port connected to the Control Unit and Microbox PC respectively.
4. Connecting PC1 to the Arduino via USB port.
5. Connection of the PC2 via Ethernet cable to the interrogator to which the optical fibres with three different channels are connected through a specific connector, one for each optical fibre.

6. Connection of strain gauges to the acquisition unit.

8.3.2 Data Acquisition

The acquisition phase involves an initial check on the operation of the sensors and the subsequent execution of the command. It consists of the following points:

1. Evaluation through PC1 using the Arduino programme interface of the tension state of the springs. The springs in the loading phase of the test must be unloaded, i.e. the reading must be close to zero. If a non-zero tension state is read through the Arduino interface, the springs can be unloaded by moving the load module mover away from the gearbox. Unlike the unloading phase in which the springs must be tensioned due to the command imposed in the previous load phase.
2. Verification of the actual reading of all three optical fibres connected to the interrogator through the PC2 on which the SmatSoft interrogator reading software is installed.
3. Verification of the actual reading of the strain gauges connected to the measuring unit through an appropriate light signal.
4. Motor position reset through PC1. In order to set a new starting condition from which to start the command.
5. Implementation of the command to be carried out, on the Starter programme via PC1. At this stage, the command to be implemented is chosen by setting its characteristics. In our case, as it is a simple step command, only the step amplitude is set.
6. Resetting the strain gauge position. In order to consider the actual strain state as zero in order to measure the deformation change induced by the command to be carried out.
7. Start of strain gauge data acquisition.
8. Start acquisition of optical fibre data provided by the interrogator through PC2.

9. Starting the Matlab programme that acquires load cell data through PC1.
10. Verification of effective serial communication between PC1 and the Arduino.
11. Application of the command previously set on the Starter software through PC1.
12. Stop data acquisition by the strain gauge controller. Other acquisition systems independently stop acquisition after a set time.

8.4 Programmes used for testing

As listed in the test procedure, it is necessary to use different programmes in order to be able to carry out the acquisition correctly, in this sub-section we will analyse the main programmes used.

8.4.1 SmatSoft

Smartsoft is the programme for reading the data provided by the interrogator. Before starting with the data reading, it is necessary to select the number of channels to be used, which corresponds to the number of optical fibres, and the maximum number of Bragg gratings on a single optical fibre. In our case, three separate optical fibres were used, resulting in three channels and a maximum number of Bragg gratings on a single fibre of two. The programme allows the acquisition frequency to be chosen in a range from a minimum of 2.5 Hz to a maximum of 2500 Hz, in our case an acquisition frequency of 100 Hz was chosen, corresponding to a data every 0.01 seconds. Finally, the programme allows two different modes of acquisition, the first characterised by a single acquisition with a time set by the user and a second mode characterised by a series of acquisitions with a fixed time interspersed with a pause. In our case, since we had to carry out a test of short duration, we used the first method with an acquisition time of 60 seconds. The data is saved in a text file.

8.4.2 Matlab & Arduino

Matlab and Arduino were used in pairs to acquire the data from the load cells. The programme implemented in the Arduino reads the forces to which the load cells are subjected and via the serial port the data is sent to PC1. A Matlab programme is run on PC1 at the same time, which saves the data received from the Arduino in a structure, providing a data.mat file at the end of the test.

8.4.3 Catman

Catman is the programme installed in the strain gauge monitoring unit. It allows the data provided by the strain gauges to be read and saved. Through a graphic interface, it shows the strains read by the different sensors in real time. Unlike the other programmes used, it is not possible to select the duration time of the acquisition, which must be started and stopped manually. The file provided by the control unit at the end of the test is an Excel file.

Chapter 9

Load module validation

The post-processing of the results was carried out in Matlab. Regarding the validation of the load module, the acquisition system, as mentioned above, through the programme implemented in the Arduino reads the data provided by the load cells in response to the applied command. The data are sent to PC1 via serial communication with the Arduino. On the PC1, a Matlab programme saves the data obtained from the load cells in a Matlab structure. The data of interest for the validation of the load module are the recall forces generated by each individual spring in response to the step command performed. We go on to analyse a single set of tests consisting of six different steps.

9.1 Recall forces

The data obtained are noisy and show abnormal instantaneous peaks, which is due to the excessive length of the cables connecting the load cells with the Arduino board. To solve this problem, the signal was filtered by eliminating the peaks and reducing the noise through a moving average. The figures 9.1 and 9.2 show the responses of the individual springs to step commands of different magnitudes. A comparison of the corresponding graphs shows that the data for spring 2 is noisier than for spring 1. In addition, it can be seen that on actuation of the command, both springs have a transitional phase typical of the response of a step command, stabilising at a new equilibrium value. The transient phase has a longer

duration for the control with a greater delta of 30 deg, unlike all the other tests, the difference between the initial and final position corresponds to 10 deg. Finally, it can be observed that a greater deviation from the gearbox's equilibrium position generates a greater pullback force typical of a liner system characterised by springs.

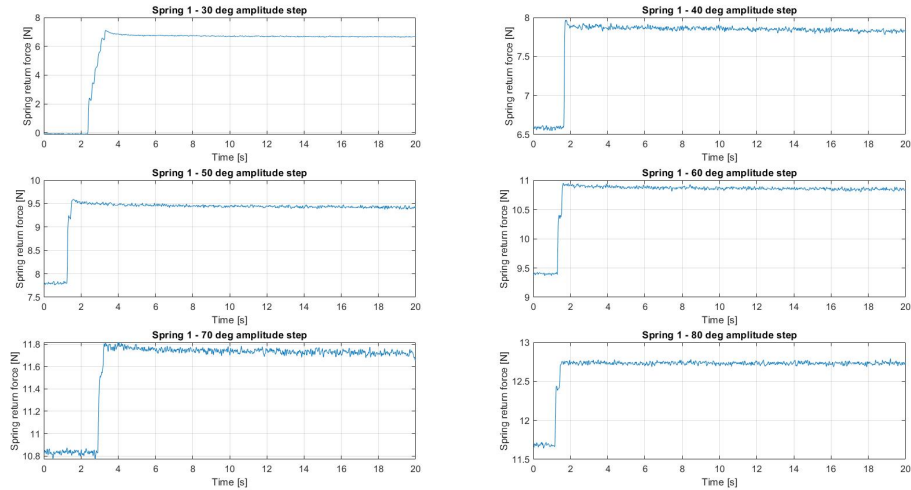


Figure 9.1. Response of spring 1 to step command

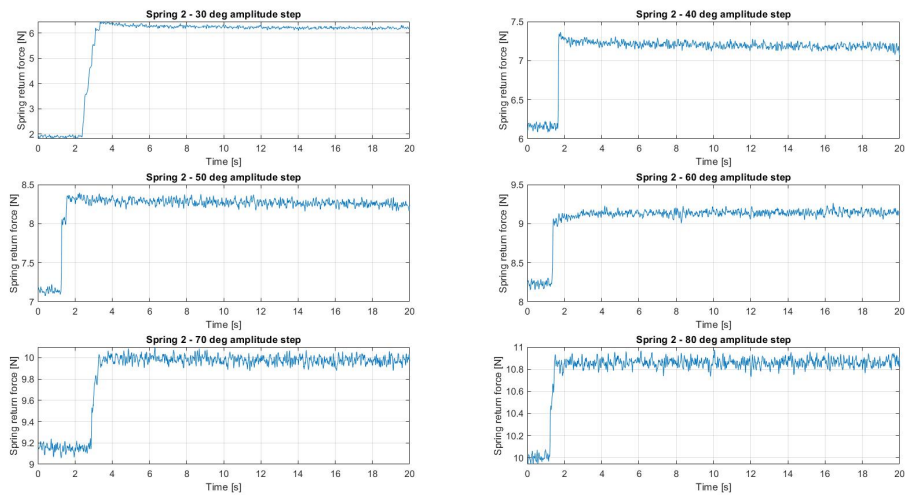


Figure 9.2. Response of spring 2 to step command

9.2 Applied torque

Considering the return forces generated by the two springs in response to the step command and the radius of the gear guide r equal to 0.08 m. The torque generated on the gearbox by the pair of forces is calculated using the following relationship:

$$C = (F_1 + F_2)r \quad (9.1)$$

The torque has the same trend as the spring return forces, presenting the typical step response. The data for the second spring also makes the data for torque C noisy. Since in order to validate the load modulus it is necessary to consider the torque reached at the end in each individual test, to reduce the effects due to signal noise, the average of the last 2 seconds was used as the value, making the measurement more accurate.

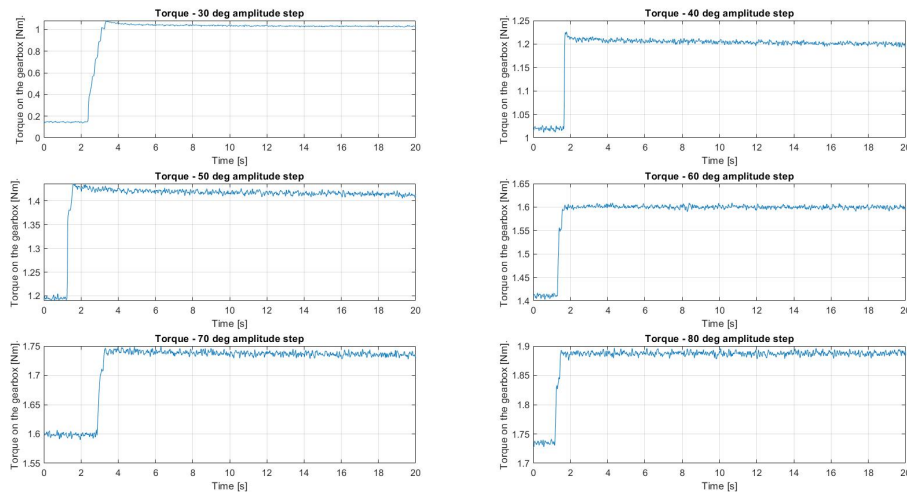


Figure 9.3. Torque generated by the two recall forces

The points obtained can be graphed as a function of spring elongation ΔL in order to check the actual correlation between the torque generated and the spring elongation determined by the rotation of the gearbox turn. Starting from the command imposed in degrees and knowing that the gearbox guide has a circular shape, it is possible to calculate the spring elongation from the following relationship:

$$\Delta L = \frac{\alpha \pi r}{180} \quad (9.2)$$

Where α corresponds to the command imposed in degrees and r to the radius of the gearbox guide. Representing the final torque generated on the gearbox as a function of the spring elongation obtained in the various tests, we obtain the graph shown in the figure 9.4. It can be seen that an increase in the intensity of the control with respect to the null position causes a greater rotation of the gearbox and a consequent elongation of the two springs which corresponds to the generation of a greater torque. The torque trend is linear, with each variation of 10 deg corresponding to an additional elongation of the springs ΔL of 0.014 m resulting in an increase in torque C of approximately 0.2 Nm. This behaviour is due to the linearity of the designed system, the springs being the heart of the system being a linear type component.

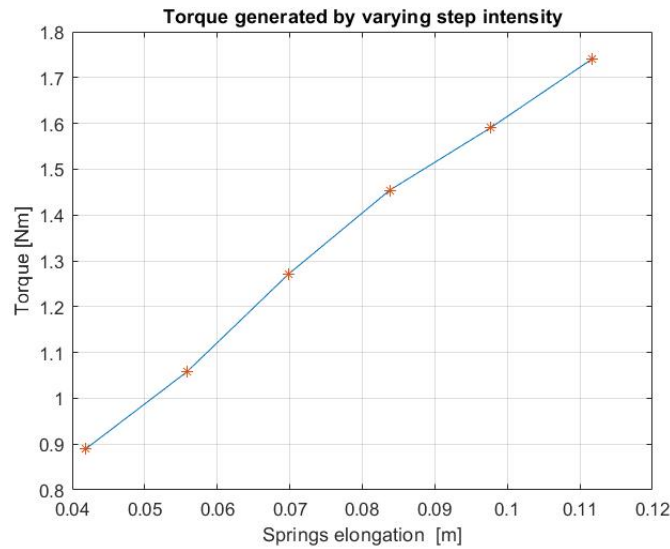


Figure 9.4. Torque applied to the gearbox as spring elongation

9.3 Comparison of different test series

In order to obtain a proportionality coefficient K which is able to relate the elongation of the spring to the torque generated on the gearbox, so as to predict how much the spring needs to be elongated in order to generate the desired torque, it is essential to have an adequate number of points, which is why the series of tests was repeated. The data for the second and third series of tests can be found in the appendices B.1 and B.2. By repeating the procedure just described for successive series of tests and superimposing the three curves which relate the generated torque C to the elongation of the springs, the graph in the figure 9.5 is obtained.

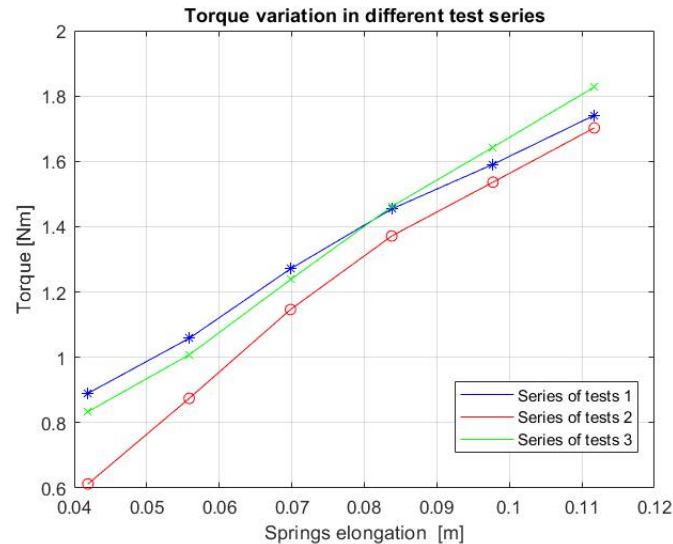


Figure 9.5. Torque applied for three different test series

The three curves obtained from the three series of tests show the same similar trend with similar slope but different modulus, this is due to the nonlinearities introduced by friction. The control puts the motor into operation, which induces the rotation of the gearbox, which, having reached the commanded position, will settle its motion reaching a new equilibrium point. The equilibrium point reached is influenced by the random phenomenon of friction preventing the system from generating the same torque at all times. The three curves tend to come closer together as spring elongation increases, which is due to the fact that

the effects of friction are less influential as spring elongation increases. In fact, the increase in the commanded position which results in greater spring elongation and consequently greater torque, which makes the effect of friction more negligible. It should be noted that in the various tests carried out, the maximum torque achieved is 1.82 Nm while the load module was designed to generate a maximum torque C_{max} of 12 Nm. It can therefore be assumed that as the elongation of the springs increases, the system error will tend to decrease.

9.4 Linearisation and evaluation of relative error

Considering the three curves obtained from the series of tests carried out to determine the proportionality coefficient K , the mean square deviation of the curve obtained from the average of the three torque C generated in the three tests with the same spring elongation is carried out. The figure 9.6 represents the straight line obtained with the least-squares deviation which gives a coefficient of proportionality K_{sys} equal to:

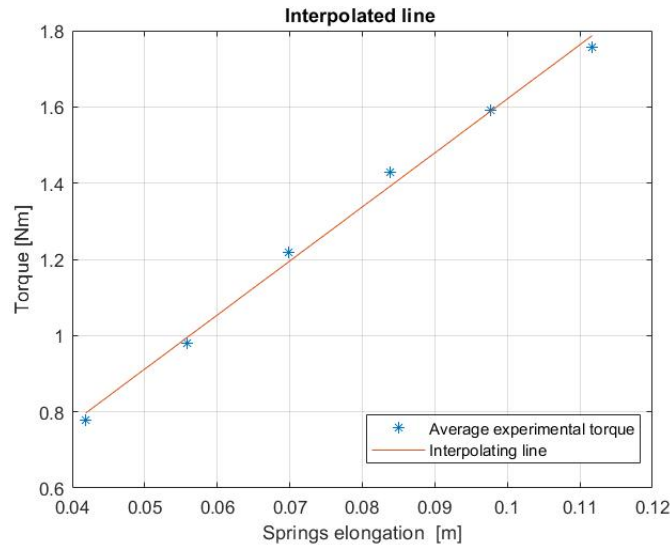


Figure 9.6. Linearised torque

$$K_{sys} = 14.18 \left[\frac{Nm}{m} \right] = 0.088 \left[\frac{N}{mm} \right] \quad (9.3)$$

The calculated coefficient of proportionality K_{sys} represents the coefficient of the entire load modulus and is different from the coefficient of resistance of the designed springs K_{design} calculated in the equation 4.3. If all components characterising the load modulus were idal and perfectly rigid and there were no friction-induced non-linearities, the two coefficients would be identical. But experimentally it is shown that this is not the case, this is due to the elasticity of the ropes, which are not perfectly rigid, and the friction present between the springs and the tubes and between the ropes and the pulleys resulting in a higher coefficient of proportionality. Having determined the coefficient of proportionality K_{sys} , the relative error is calculated using the following equation, results in the table 9.1.

$$e_{rell} = \frac{C_{exp} - C_{lin}}{C_{lin}} \quad (9.4)$$

Where C_{lin} is the torque calculated from the equation $C_{lin} = K_{sys}\Delta L$ while C_{exp} is the torque relative to the experimental data.

Error committed in each test			
	Test 1	Test 2	Test 3
30 deg	0.116	0.231	0.046
40 deg	0.063	0.121	0.012
50 deg	0.065	0.039	0.037
60 deg	0.045	0.014	0.050
70 deg	0.011	0.033	0.033
80 deg	0.026	0.047	0.022

Table 9.1. Relative error committed in each test

Representing the straight line with the uncertainty is the figure 9.7. From the table 9.1 and the figure 9.7, it can be seen that as the elongation of the springs increases, the relative error committed by using the straight line to approximate the torque generated on the gearbox tends to decrease. This behaviour can be traced back, as already observed in the figure 9.7, to the phenomenon of friction. Above a command of 60 deg or more, which corresponds to a spring elongation of 0.083 m, the relative error is always less than 5%. This is due to a lower contribution in the error from friction and rope elasticity, the residual error corresponds to the band in which the experimental point tends to stop due to the friction phenomenon

hence the name friction band. We can conclude that for small commands the error committed is very high and does not allow the straight line $C_{lin} = K_{sys}\Delta L$ to be used to accurately estimate the torque generated on the gearbox, but once a gearbox rotation of 60 deg has been reached the error committed is acceptable.

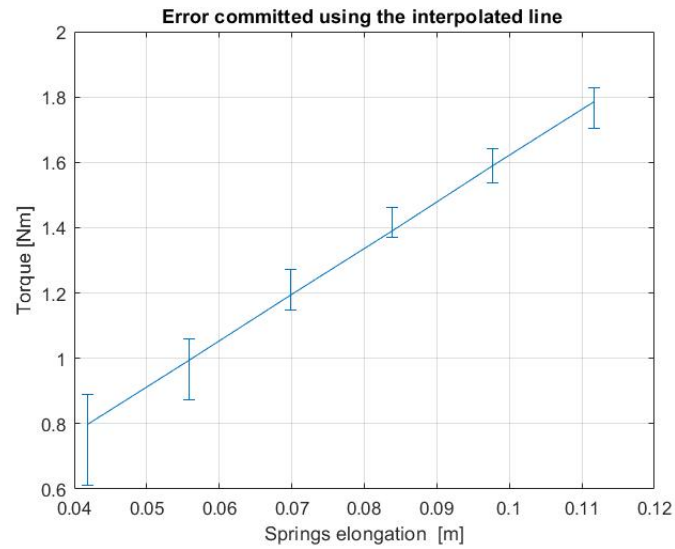


Figure 9.7. Uncertainty in torque calculation with the approximate straight line

Chapter 10

Evaluation of FBG as prognostic sensors

10.1 Optical fibre and strain gauge response to step command

As with the validation of the load module, the post-processing of the data for the evaluation of the use of the optical fibres with Bragg grating as sensors for the prognostic analysis was performed via Matlab. In this chapter, the single unloading phase of the test through a step command of 60 deg intensity will be analysed. All data for the other tests can be found in the appendices C.1, C.2, C.3, C.4 and C.5. It was decided to focus specifically on the unloading phase and not the loading phase, since in this phase the system always reaches the same equilibrium position. Unlike in the loading phase where, as noted in the previous chapter, the random effect of friction can lead to a greater error. The response provided by optical fibres with a Bragg grating and strain gauges will be analysed, and the relationship between the relative error of the optical fibre and the absolute error of the strain gauge will be evaluated by deriving a proportionality coefficient K . Finally, it will be observed how strain gauges and in particular optical fibres are able to measure commanded currents if these induce a deformation in the structure.

10.1.1 Optical fibre

Analysing the data from the text files generated by the Smart-Soft programme, which saves the wavelengths detected by the four Bragg gratings installed on the gearbox with a frequency sampling of 100 Hz, the graphs in the figure 10.1 are obtained for the four installed sensors.

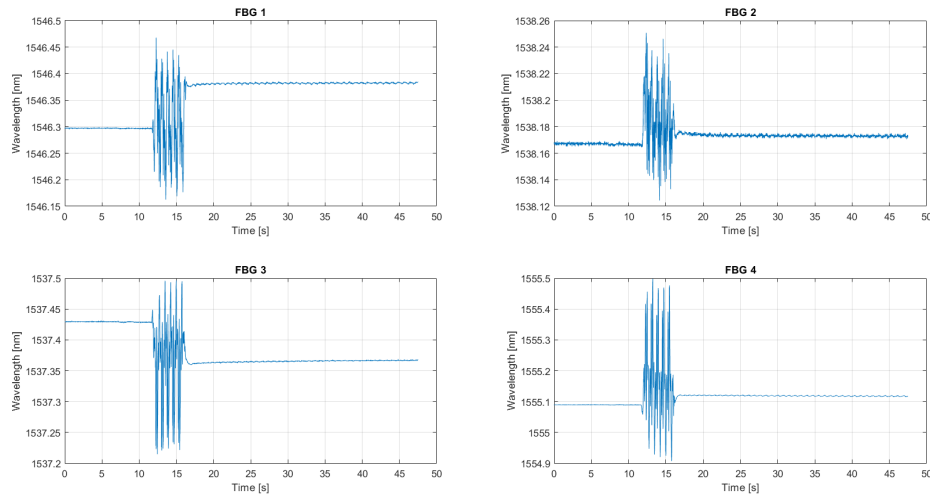


Figure 10.1. Optical fibre response to step command

All four FBG Bragg gratings initially exhibit a constant wavelength corresponding to the wavelength reached in the loading phase. At the moment when the step command is applied to unload the system, the transient phase characterised by a large number of oscillations and peaks begins, which end when the system reaches the commanded position, resulting in a new equilibrium point. This point corresponds to the null position of the system, in which the load module does not apply any torque to the gear as the springs are in the rest condition. Looking at the four Bragg gratings specifically, it can be seen that the first Bragg grating FBG 1 shows a wavelength reduction which corresponds to a decrease in tension. Due to the fact that the unloading phase is being considered, the measured tension decrease implies that FBG 1 has undergone a tensile deformation, induced by the torque applied by the load module on the gearbox, in the previous loading phase. The Bragg gratings FB2 and FB4 behave similarly, also exhibiting a decrease in

tension. In contrast, the Bragg grating FBG 3 presents an inverse trend to the others, characterised by an increase in wavelength, which determines how the grating underwent compressive deformation in the previous loading phase. Furthermore, it can be observed that the Bragg grating FBG 2 is noisier than the other three. This is due to the installation in the vicinity of the encoder, whose rotation induces an increase in noise. Finally, the Bragg grating FBG 4 exhibits a damped pattern. This is due to the cyanoacrylate glue used for the installation of the optical fibres, in particular for the Bragg grating FBG 4, which is completely embedded in the glue and thus suffers more from the damping effect.

10.1.2 Strain gauges

The data from the strain gauge acquisition unit were interpolated in order to obtain the same number of points as for the Bragg gratings. This was necessary because the strain gauge acquisition unit has a sampling rate half that of the interrogator.

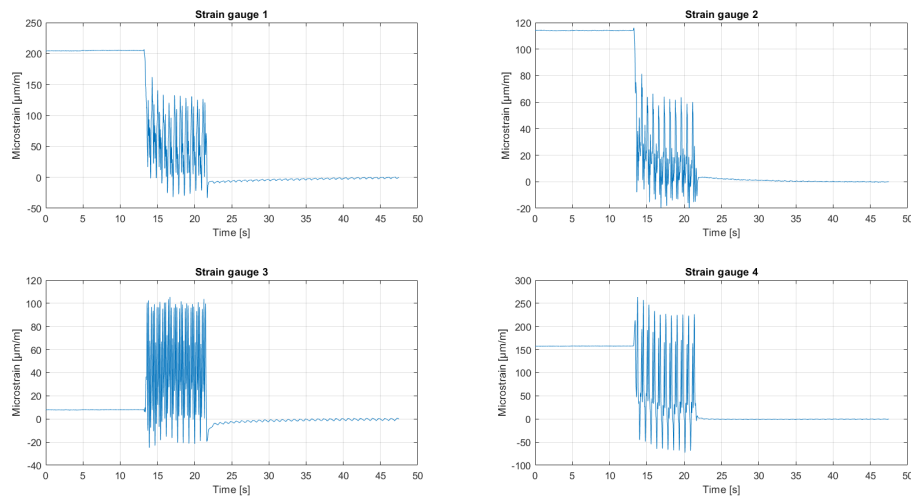


Figure 10.2. Strain gauge response to step command

The response to the command is similar to that observed in the optical fibre. In an initial equilibrium phase, the strain gauges measure the strains obtained in the previous loading phase. The start of the command determines the beginning of the transitional phase characterised by oscillations and peaks until a new equilibrium

condition corresponding to zero deformation is reached. Once the commanded position is reached, the system is completely unloaded. As in the previous case, the strain gauges corresponding to the Bragg gratings FBG 1, FBG 2 and FBG 4 are characterised by a reduction of the deformation from the tensile condition obtained in the loading phase to the condition of zero deformation reached during the test. Strain gage 3 exhibits a very small deformation at the start of the test, which may be due to the installation point of the sensor, which, as will be noted in the following section, does not result in a linear correlation between strain measured by the strain gauges and the relative error of the corresponding Bragg grating.

10.2 Synchronisation

From the procedure described in the chapter 8 , it can be seen that the acquisition of optical fibre and strain gauge data does not take place simultaneously. there is a time lag due to the seconds required to start the respective acquisition systems. The hardware difficulties do not make it possible to install a trigger to allow data synchronisation in a simple way. For these reasons, synchronisation was carried out in post-processing by analysing the peaks of the two signals, in particular by detecting the time instant of the last peak. The function developed involved filtering through a moving average of the signals in order to reduce the noise present in the data. The steady state signal, as previously observed, will be in constant average value, therefore, its value was calculated as the average of the last 5 seconds of the test. In the same interval, the noise band was calculated as the difference between the maximum and minimum value of the signal. By checking whether the difference between the value of the steady-state signal and the value of the signal at the i th instant is greater than the noise multiplied by a factor B , the instant at which the signal enters the transitional phase is determined. The B_{FBG} chosen for the optical fibre signal is 5, while the B_{SG} chosen for the strain gauge signal is 1.5. Having determined the starting point of the transient phase, the time instant of the last peak is determined by comparing the sign of the derivative of the signal at step i with the sign of the derivative at the next step. If the signs are discordant, the peak has been identified, otherwise the signs of the derivative

at the next step are compared. The difference of the time instant of the last peak of the optical fibres and the time instant of the last peak of the strain gauges gives the phase shift of the two signals. The figure 10.3 shows the synchronisation performed in the unloading phase of the 60 deg test.

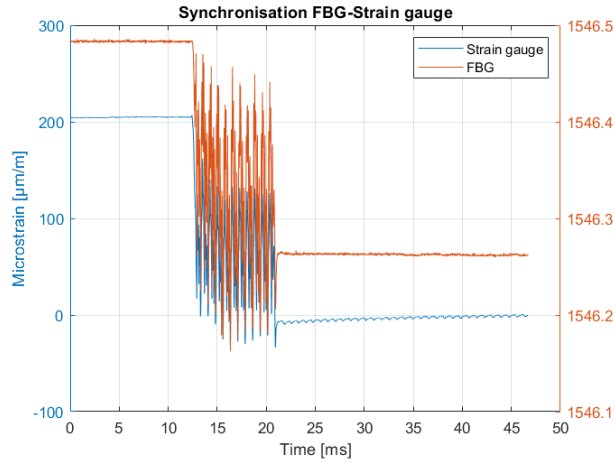


Figure 10.3. Synchronised strain gauge and optical fibre response to step command

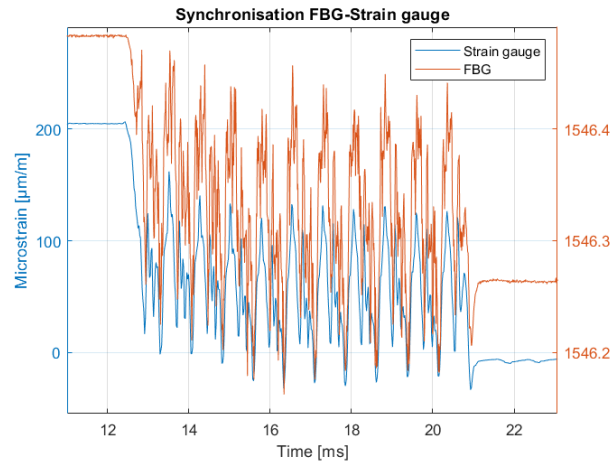


Figure 10.4. Focus on the transitional phase

The graph superimposes the two signals with two different scales in order to assess the time lag only. In blue is the deformation measured by the strain gauges and in orange the wavelength measured by the Bragg grating, the data are for the

sensors in position one. The two signals show the same quality trend, starting and ending the transient phase at the same time. Looking specifically at the transient phase, shown in the figure 10.4, it can be seen that every peak measured by the Bragg grating corresponds to a peak measured by the strain gauge, and the two signals show an almost identical pattern. This first result shows that the Bragg grating is able to measure the strain induced by the load modulus on the gear in a qualitatively similar way to strain gauges. The next step is to evaluate the modulus of the measured strain of the Bragg grating and to compare it with that of the strain gauges

10.3 Deformation-wavelength relationship

In order to verify the actual feasibility of using optical fibres with Bragg gratings as prognostic sensors, in this specific case to measure the strain on the gearbox induced by the load modulus, a linear relationship between the strain measured by the strain gauge and the measured wavelength of the optical fibres was searched for. In particular, a proportionality coefficient was determined through the straight line obtained with the least-squares deviation from the point correlation of the relative error of the FBG Bragg grating and the absolute error of the strain gauges. For strain gauges, the absolute error is used instead of the relative error, since the strain gauge must be reset for a better measurement during the acquisition phase. The relative error of the Bragg grating is given by the following relationship:

$$e_{rel} = \frac{\lambda_i - \lambda_B}{\lambda_B} \quad (10.1)$$

Where λ_i is the value of the wavelength averaged over the first 2 seconds of the unloading phase, in which the gear is deformed due to the load imposed by the load module. While λ_B is the value of the nominal wavelength of the Bragg grating considered. The straight line representing the mean square deviation from the correlation of the points, relative error of the optical fibres and absolute error of the strain gauges is as follows:

$$\frac{\lambda_i - \lambda_B}{\lambda_B} = K\epsilon \quad (10.2)$$

The equation expresses the percentage deviation between the measured wavelength and the nominal Bragg grating wavelength. This percentage difference is equal to the deformation the gearbox is subjected to at the point where the sensors are installed multiplied by a proportional coefficient K.

10.3.1 Sensors in position 1 and 4

The following figure shows the regression line for the sensor pair in position 1 and 4.

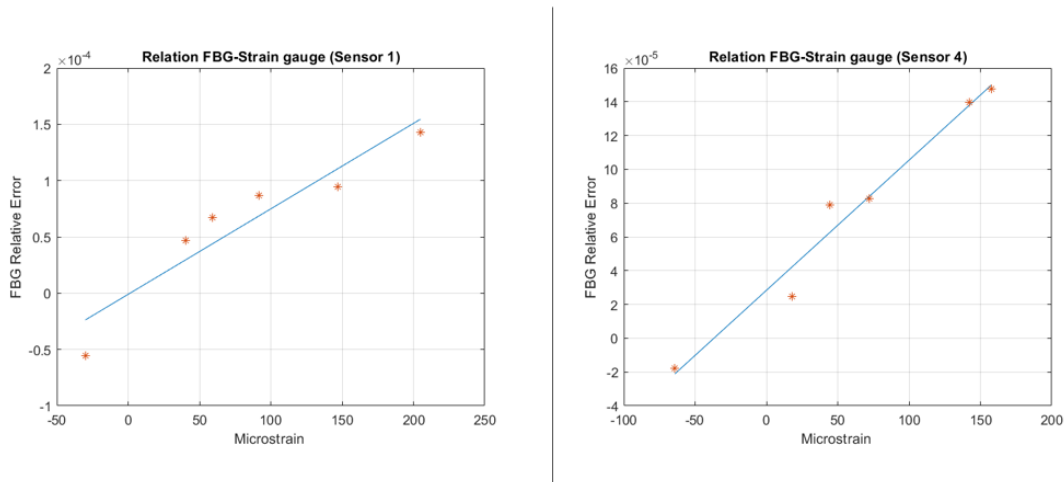


Figure 10.5. Sensor approximation lines in position 1 and 4

For both sensor pairs, the calculated K corresponds to:

- $K_1 = 7,59 * 10^{-7} [\frac{1}{\mu m}] = 0.759 [\frac{1}{m}]$
- $K_2 = 7.70 * 10^{-7} [\frac{1}{\mu m}] = 0.770 [\frac{1}{m}]$

The value obtained is approximately the same for both sensors and is perfectly in line with the values reported in the literature where the proportionality coefficient is $0.78 \frac{1}{m}$ [8]. From this it can be seen that the fibres relative to the sensors at position 1 and 4 can be used to calculate the deformations on the gearbox.

In the graphs shown in the figure 10.5, it can be seen that for both sensor pairs, the experimental points tend to approach the regression line as the measured strain

increases. This behaviour is due to the sensitivity of the two sensor types, which is greater when a specific strain value is exceeded. In fact, these sensors are normally used to measure higher deformations than those at which the gear has been placed for structural reasons. One might think that having obtained a proportionality coefficient K in line with the literature, all points must be on the regression line, experimentally this has proven not to be the case. In fact, the experimental points are positioned both above and below the regression line, but maintain an almost constant distance, which means that the error committed when using the regression line is approximately constant in modulus, but if the experimental point is above the line, an overestimation will occur, and if the experimental point is below, a underestimation will occur. This behaviour may depend on several factors:

1. The glue used in the installation phase can alter the optical properties of the optical fibre by causing a change in the refractive index of the grating.
2. The unconventional surface and the installation procedure of the sensors did not allow them to be placed in the same position. This would not have been a big problem if the material of the gearbox had been isotropic and homogeneous, but not having these characteristics the point and direction of force application can alter the results obtained.
3. Temperature can affect the wavelength measured by the Bragg grating. The different tests were carried out at different times resulting in a non-constancy in the laboratory temperature. Such variations may have slightly altered the results.

10.3.2 Sensors in position 2 and 3

The figure 10.6 shows the regression line of the sensor pair in position 2 and 3. In this case, the proportionality coefficients K are not acceptable as they are highly discordant from those reported in the literature [8]. This inconsistency can be due to two causes:

- $K_1 = 2.99 * 10^{-7} [\frac{1}{\mu m}] = 0.299 [\frac{1}{m}]$
- $K_2 = -3.96 * 10^{-7} [\frac{1}{\mu m}] = -0.396 [\frac{1}{m}]$

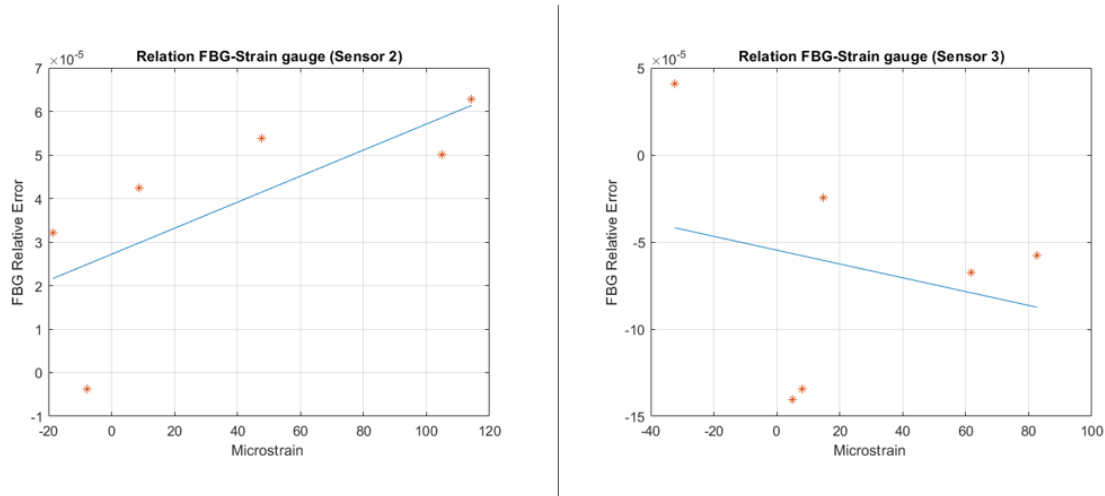


Figure 10.6. Sensor approximation lines in position 2 and 3

- **Installation of the sensors**

As already analysed in the chapters on the installation of the optical fibres and the strain gauges, the pair of sensors in position 2 and 3 suffered problems during installation due to the encumbrance of the braking module on the test bench which complicated the installation procedure. In particular, sensor pair 2 was not installed on the same transverse axis, while the sensor pair in position 3 due to a poorly installed optical fibre did not allow the strain gauge to be installed in the correct position, forcing it to be installed close to the gearbox support screw. For these reasons and due to the structure of the gearbox, which is neither isotropic nor homogeneous, the results are compromised.

- **The magnitude of the strains**

When comparing the strains measured by strain gauges 1 and 4 with those measured by strain gauges 2 and 3, it can be seen that the latter are significantly lower, with a maximum strain of $120 \mu m$ for strain gauge 2 and $80 \mu m$ for strain gauge 3. The strains are approximately half as high. As mentioned above, the sensitivity of strain gauges tends to increase with increasing strain. With strains such as those measured by the sensors in position 2 and 3, the

sensitivity will be low and consequently the error higher.

10.4 Deformation reconstruction with FBG

The study will be continued with the sensors in position 1 and 4 only, excluding the sensors in position 2 and 3 for the reasons stated above. From the equation 10.2, it is possible, through the inverse formula, to derive the deformation through the relative error of the optical fibre with Bragg grating. The relationship is as follows:

$$\epsilon = \frac{1}{K} \frac{\lambda_n - \lambda_B}{\lambda_B} \quad (10.3)$$

Where λ_n corresponds to the wavelength detected by the Bragg grating at the n th instant, λ_B is the nominal wavelength of the Bragg grating. The figure 10.7 shows for the sensor pair at position 1 and 4, in blue the deformation actually measured by the strain gauge and in orange the deformation reconstructed through the equation:

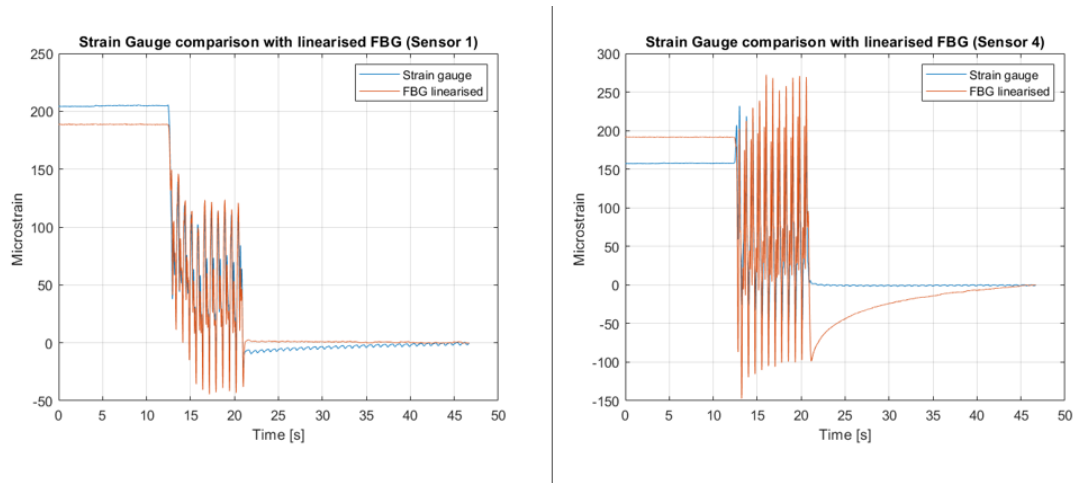


Figure 10.7. Comparison of deformation measured by strain gauges and optical fibres at position 1 and 4

The strain obtained by means of the regression line for sensor pair 1 and 4 shows a very similar trend to that of the strain gauge, roughly reproducing the deformation. The only exception is a slight deviation upwards or downwards, due to the positioning of the experimental point in relation to the regression line. In

fact, the experimental point not being exactly on the regression line but higher or lower generates a positive or negative error respectively.

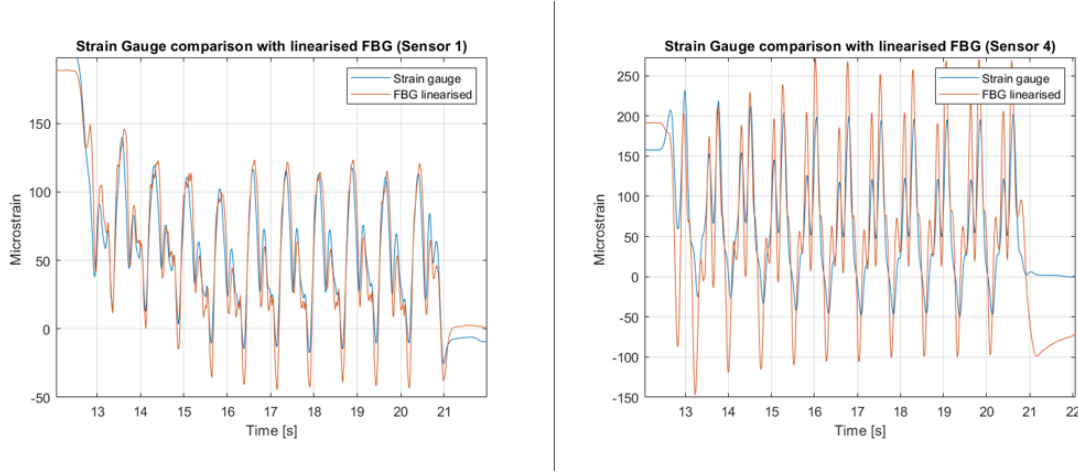


Figure 10.8. Zooming in during the transitional phase Zooming in during the transitional phase

The figure 10.8 shows an enlargement on the transient part, it can be seen that the strain reconstructed from the regression line follows the deformation measured by the strain gauge almost perfectly. The trend and the number of peaks are very similar, not only in time as already seen in the synchronisation sub-section, but the modulus also shows a certain similarity with the exception of the error already present in the transitional phase.

10.4.1 Pearson correlation

In order to determine the correlation between the strain signal measured by the strain gauges and the signal reconstructed using the proportionality coefficient relative to the regression line, a statistical index called the Pearson index [6] was used. Pearson's index is a linear correlation index which takes two statistical variables and expresses their linear correlation. In particular, taken two statistical variables A and B, the Pearson index is expressed as follows:

$$\rho_{AB} = \frac{\sigma_{AB}}{\sigma_A \sigma_B} \quad (10.4)$$

Where σ_{AB} is the covariance between A and B and σ_A and σ_B are the standard deviations of the two variables. The index is always between -1 and 1, depending on its value, three different cases can be distinguished:

- $\rho_{AB} > 0$: Variables A and B are said to be directly correlated; an increase in one corresponds to an increase in the other variable. In particular, if $\rho_{AB} = 1$ the variables A and B are perfectly correlated.
- $\rho_{AB} < 0$: variables A and B are said to be inversely correlated, as one variable increases, the second variable decreases. In particular, if $\rho_{AB} = -1$ the variables A and B are perfectly inversely correlated.
- $\rho_{AB} = 0$: variables A and B have no correlation.

Looking at the modulus of the Pearson index, three different cases can be distinguished:

- $0 < \rho_{AB} < 0.3$ there is a weak correlation.
- $0.3 < \rho_{AB} < 0.7$ there is a moderate correlation.
- $0.7 < \rho_{AB} < 1$ there is a strong correlation.

The Pearson index was calculated on the sensor pair at position 1, the choice of points of the 28 points used in the correlation is shown in the figure 10.9.

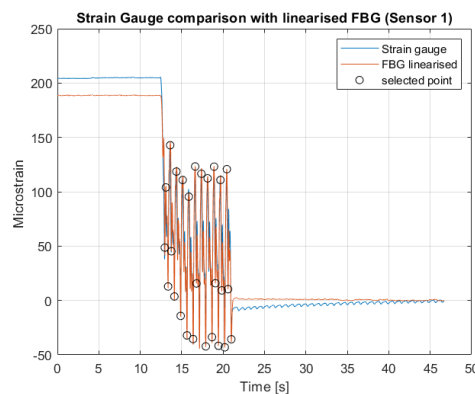


Figure 10.9. Pearson index choice points

The points were chosen by setting a time instant corresponding to the peak detected by the strain gauge and evaluating the deformation value reconstructed through the optical fibre at the same instant. The evaluation of the index resulted in a value of 0.9497, which corresponds to a strong correlation as already observed in the figures. By plotting the strain measured by the strain gauges on the y-axis and the measured strain of the optical fibre with Bragg grating on the x-axis, the graph in the figure 10.10 is obtained.

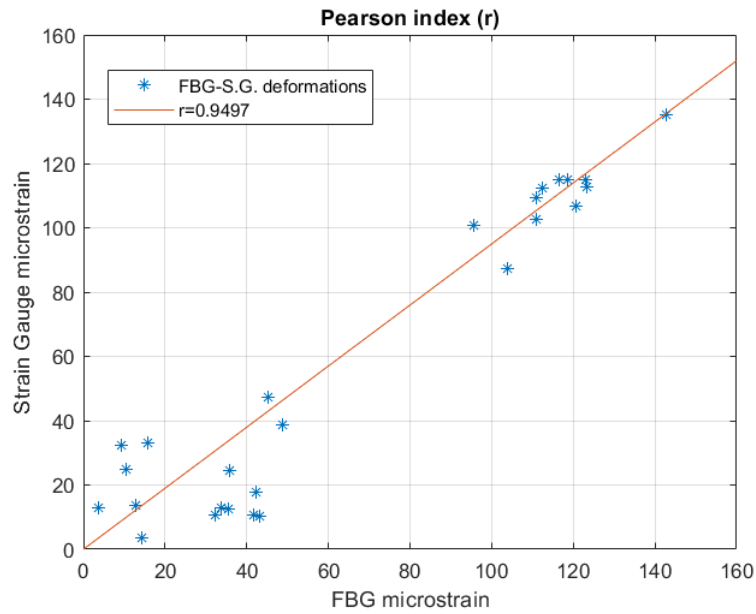


Figure 10.10. Comparison of strain measured by strain gauges and fibre optics at selected points for Pearson's index

The line corresponds to the correlation found by Pearson's index of 0.9497 while the points represent the deformation value experimentally measured at the same instant by the strain gauge and the optical fibre. The experimental points are the same as those used for calculating the index. It can be seen that the distribution of the points is more random for small strains, presenting a lower correlation and consequently a greater error; this is due to the low sensitivity of the sensors for small strains. In fact, as the strain increases, the correlation is higher resulting in a smaller discrepancy between what is measured by the strain gauge and what is measured by the optical fibre.

Chapter 11

Driven current detection

Analysing the response of the two sensors in position 1 and 4, in particular for the 30 deg and 80 deg tests, it can be seen that the signal at steady state shows constant oscillations. The figure 11.1 shows the response for the 30 deg test.

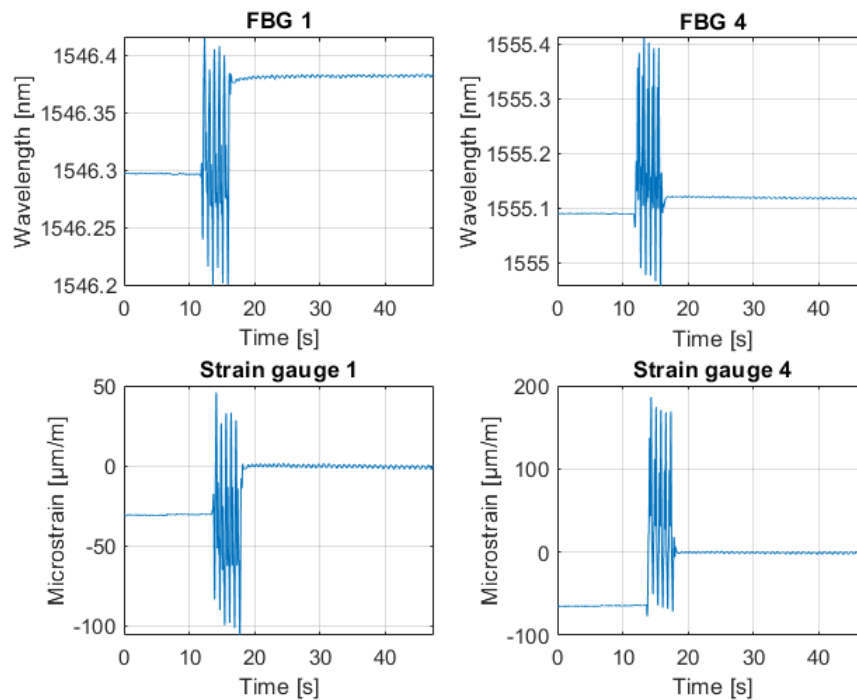


Figure 11.1. Response of sensors 1 and 4 to 30 deg step command

These oscillations around zero represent a continuous transition from a state of tension to a state of compression. This is due to the fact that the exact position commanded is not reached due to the backlash between the teeth, which leads to oscillation around this position. As the gearbox components are manufactured using the Fused Deposition Modelling (FDM) technique, they do not have a perfect shape, which means that there is backlash between the teeth that prevents them from reaching the exact commanded position. The following figure 11.2 an enlargement of the driven current, fibre optic Bragg grating and strain gauge response.

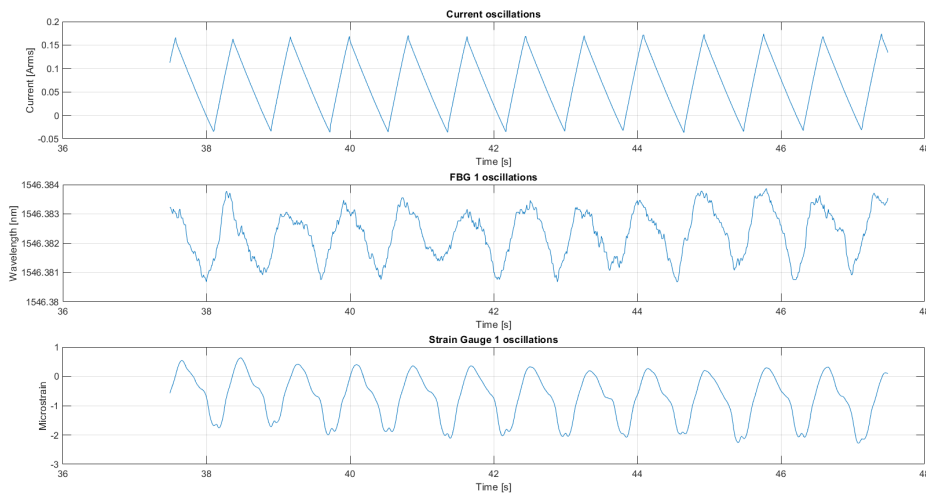


Figure 11.2. Trend of commanded current, wavelength and strain in the last test instants

It can be seen that all three signals show a similar pattern characterised by oscillations with a period of 0.8 seconds. The commanded current has a sawtooth oscillation, which is reproduced by the wavelength variation in the optical fibre with Bragg grating and through the strain gauges. In order to verify whether the oscillations measured by the sensors at position 1 are actually due to the change in the commanded current, a Fast Fourier Transform FFT [9] was carried out on the three signals. The FFT is based on the operating principle of the discrete Fourier transform DFT but reduces the computational cost. The signal is sampled and converted into a numerical form originating a sequence of N finite points, applying

the DFT results in a sampled version of the signal spectrum. The DFT returns the signal spectrum in terms of modulus and phase for given equispaced frequencies, allowing the power spectrum of the signal to be evaluated by discretising it as a function of frequency and determining the frequency that provides the greatest power contribution. The figure 11.3 shows the FFT analysis performed on the three signals.

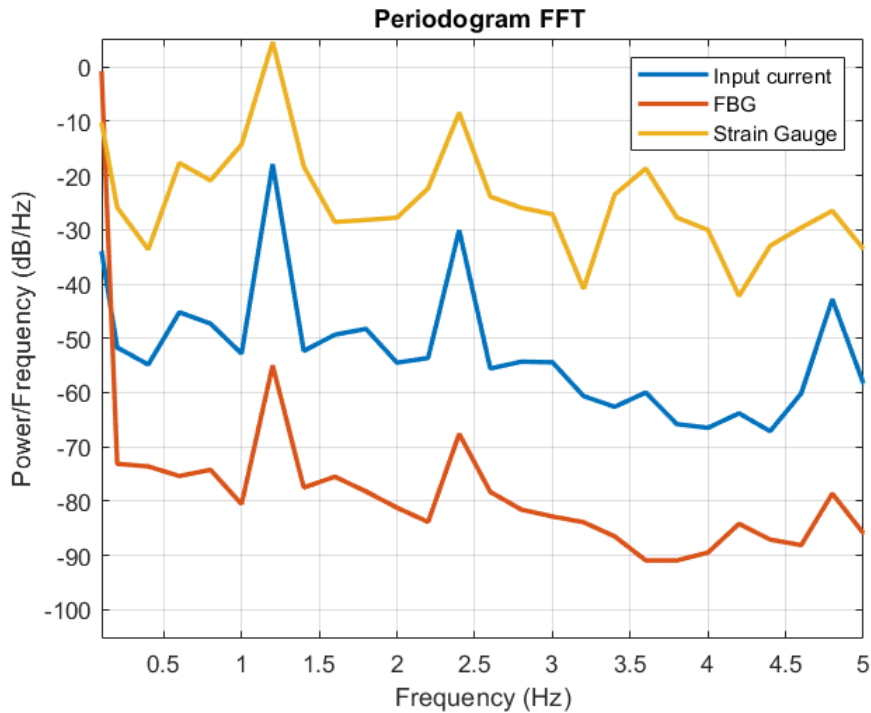


Figure 11.3. FFT of commanded current signals, wavelength and deformation

The three curves show the same trend with the maximum peak at 1.2 Hz, which corresponds to 0.8 seconds corresponding to the switching period of the current due to the clearance between the gear teeth. It can be concluded that both strain gauges and optical fibres with Bragg gratings are able to measure very small variations in the driven current. Therefore, it is possible to trace the current commanded by the control unit from the wavelength variation measured by the optical fibres.

Chapter 12

Future analyses

The results obtained for the validation of the load module show that the system created is able to generate a torque proportional to the rotation of the gearbox. Furthermore, it is possible to predict the intensity of the torque with an error of approximately 5% using the regression line obtained from the minimum-squares deviation. In future analyses, it would be possible to observe the behaviour of the relative error as the step intensity increases, to check whether the relative error continues to decrease as spring elongation increases. Finally, one could observe the behaviour of the system not for small steps as carried out in the tests presented in this thesis but with step commands of intensities greater than 30 deg, in order to observe the behaviour of friction, the greatest source of error in the system.

With regard to the results for fibre-optic sensors used as sensors for prognostic analysis, it can be concluded that the sensors installed at position 1 and 4 can be used for strain calculations. Indeed, the proportionality coefficient is in line with the literature data, as demonstrated in the previous sections. In fact, the strain measured by the strain gauge, an established sensor for strain measurement, is not very different from the strain reconstructed via the regression line using the optical fibres. Furthermore, from a prognostic point of view, the fibres were found to be able to detect oscillations in the driven current.

Bibliography

- [1] En 10270-1 physical properties and chemical composition. www.mollificiomodenese.it/glossario/acciaio-uni-en-10270-1-sm-sh-dh/.
- [2] Incremental optical encoders. www.italsensor.com/tsw58/.
- [3] Interrogator measurement, processing, mechanical, environmental and electrical. www.smartfibres.com/files/pdf/SmartScan.pdf.
- [4] *Slide of the "Manutenzione aeronautica e PCM" course*. Università degli Studi di Enna "Kore", 2014.
- [5] Vepa Atamuradov, Kamal Medjaher, Pierre Dersin, Benjamin Lamoureux, and Noureddine Zerhouni. Prognostics and health management for maintenance practitioners-review, implementation and tools evaluation. *International Journal of Prognostics and Health Management*, 8(3):1–31, 2017.
- [6] Jacob Benesty, Jingdong Chen, Yiteng Huang, and Israel Cohen. Pearson correlation coefficient. In *Noise reduction in speech processing*, pages 1–4. Springer, 2009.
- [7] Pier Carlo Berri, Matteo DL Dalla Vedova, Paolo Maggiore, and Guido Riva. Design and development of a planetary gearbox for electromechanical actuator test bench through additive manufacturing. In *Actuators*, volume 9, page 35. MDPI, 2020.
- [8] P Boccaccio, R Donà, and A Zoccoli. Calibration of a fiber bragg grating as ultra-sensitive strain gauge. In *LNL Annual Report, Appl. Gen. and Interdisc. Phys. Instrumentation*, pages 191–192. 2010.

- [9] Paul Heckbert. Fourier transforms and the fast fourier transform (fft) algorithm. *Computer Graphics*, 2:15–463, 1995.
- [10] Raman Kashyap. Theory of fiber bragg gratings. *Fiber Bragg Gratings*, 2010.
- [11] Paolo Maggiore. *Slide of the "Sistemi di bordo aerospaziali" course*. Politecnico di Torino, 2019.
- [12] Paolo Maggiore and Matteo Davide Lorenzo Dalla Vedova. *Slide of the "Modelazione, simulazione e sperimentazione dei sistemi aerospaziali" course*. Politecnico di Torino, 2021.
- [13] Paolo Mazzoldi, Massimo Nigro, and Cesare Voci. *Fisica. Volume 2: Elettromagnetismo-Onde*. EdiSES, 1998.
- [14] De Rossi Quaresimin. *INTRODUZIONE ALL'ESTENSIMETRIA*. Universtà di Padova, 1998.
- [15] Nicole Viola Sabrina Corpino. *Slide of the "Sistemi aerospaziali" course*. Politecnico di Torino, 2020.
- [16] Siemens. *SIMOTICS Synchronous motors SIMOTICS S-1FK7 Generation 2, For SINAMICS S120, Configuration Manual*. 2018.
- [17] Siemens. *Data sheet SIMATIC IPC427E Microbox PC*. 2022.
- [18] Siemens. *Data sheet SINAMICS Power module PM240-2*. 2022.
- [19] PS Valsange. Design of helical coil compression spring: a review. *International Journal of Engineering Research and Applications*, 2(6), 2012.

Appendix A

CAD

A.1 Pulley system components

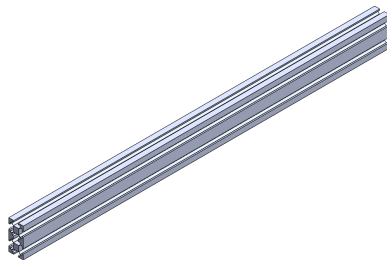


Figure A.1. Aluminium profile

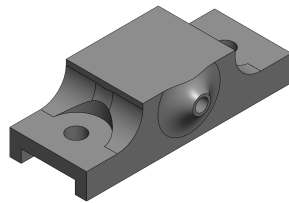


Figure A.2. Single pulley support

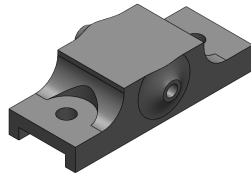


Figure A.3. Support for pair of pulleys

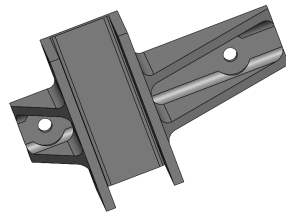


Figure A.4. Support for the aluminium profile



Figure A.5. Pulley

A.2 Mover components

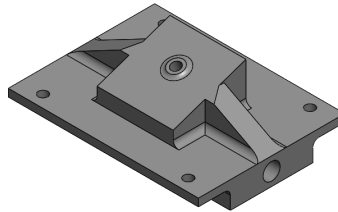


Figure A.6. Support for pair of pulleys

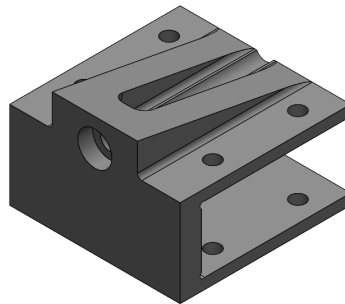


Figure A.7. Support for the aluminium profile

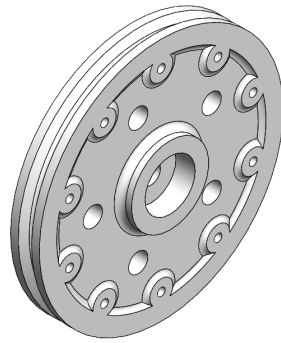
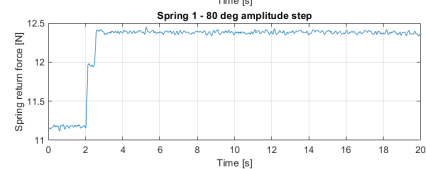
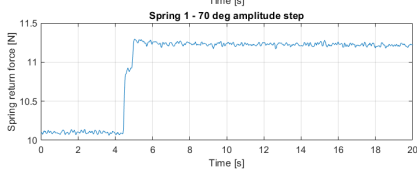
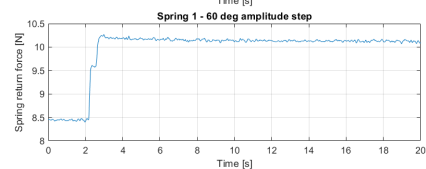
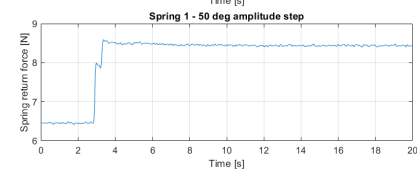
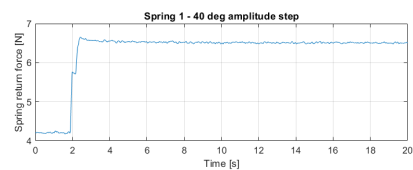
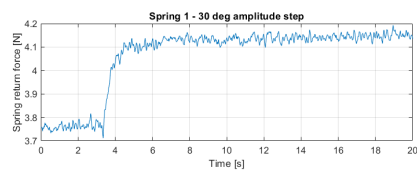


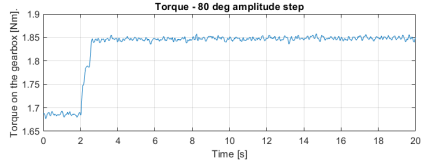
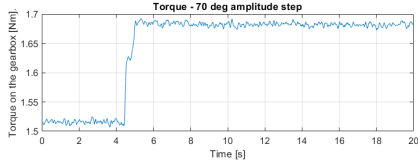
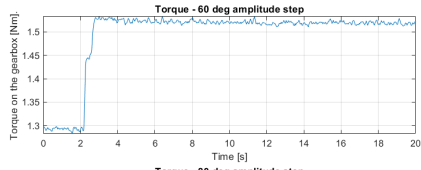
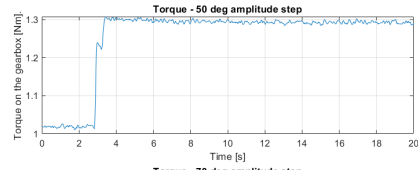
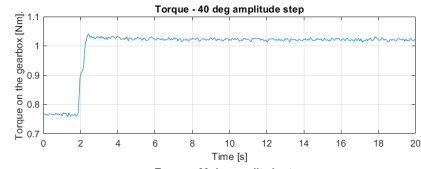
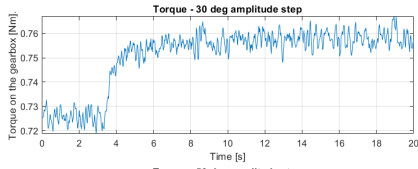
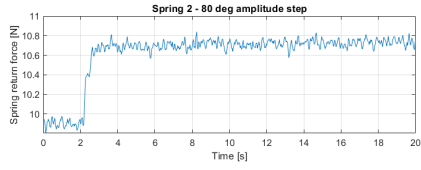
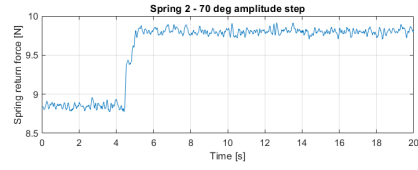
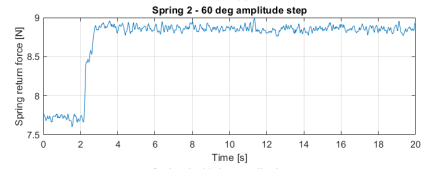
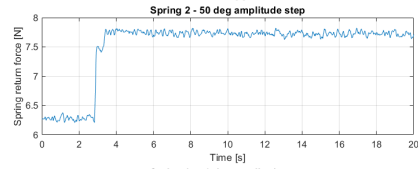
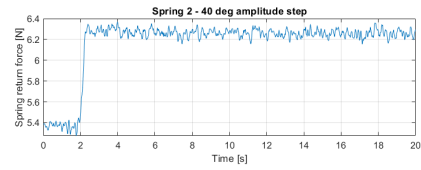
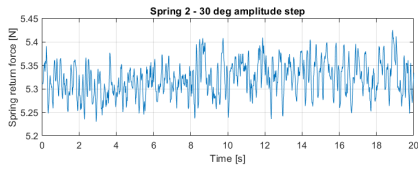
Figure A.8. Pulley

Appendix B

Load module test

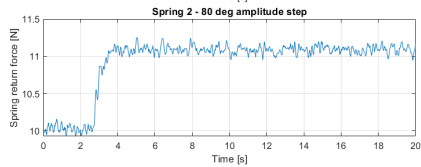
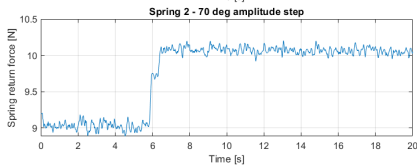
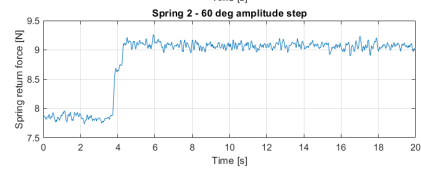
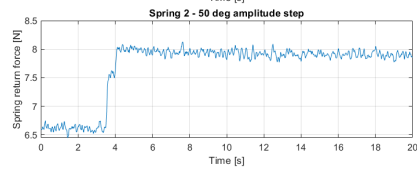
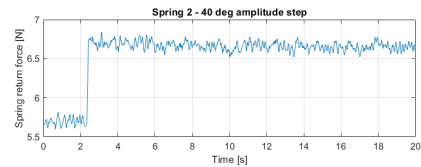
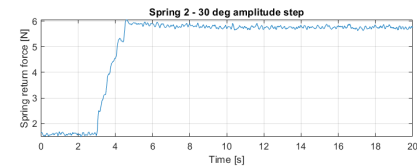
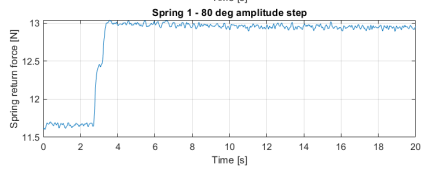
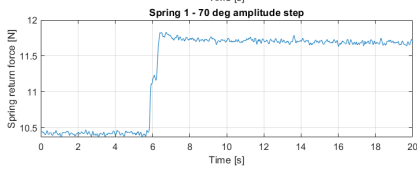
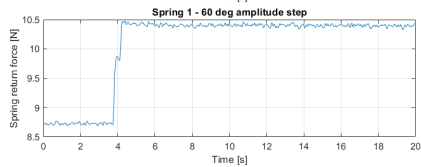
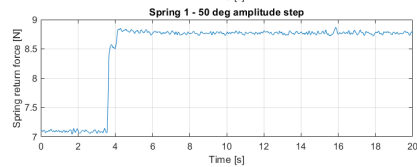
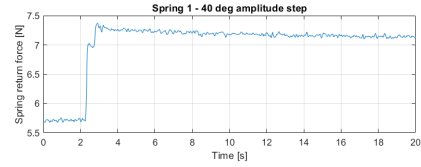
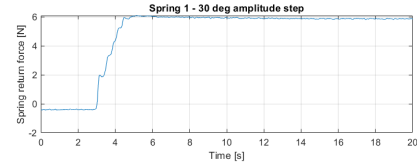
B.1 Second series of tests

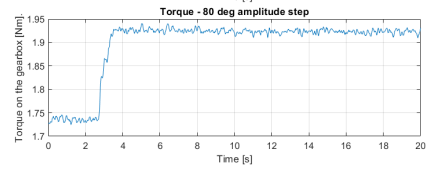
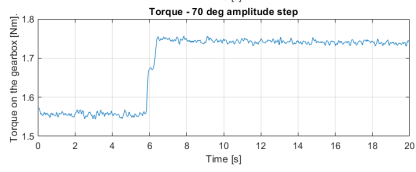
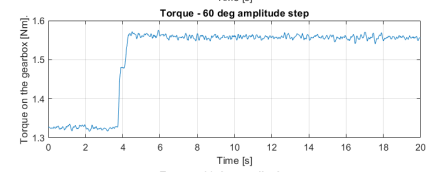
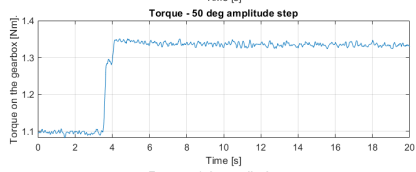
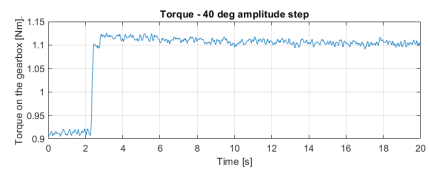
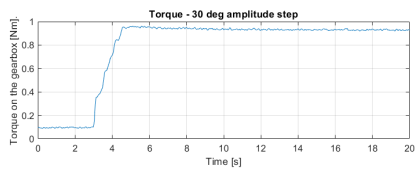




B.2 Third series of tests

Load module test

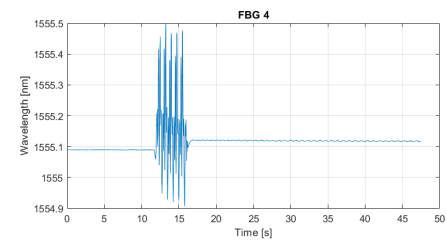
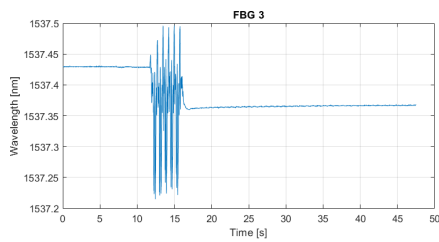
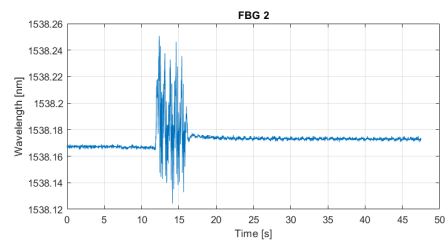
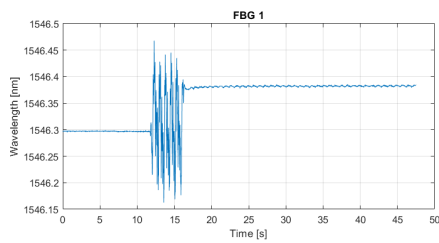




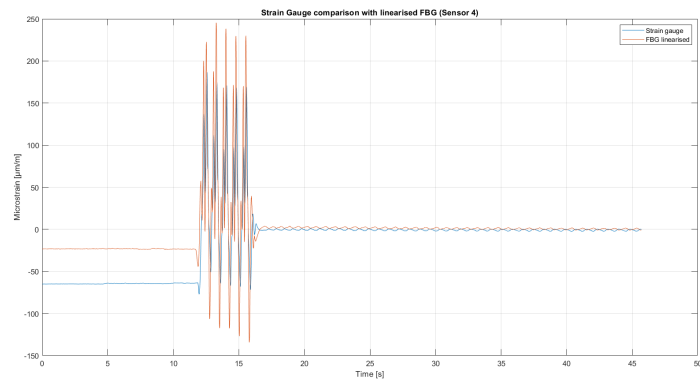
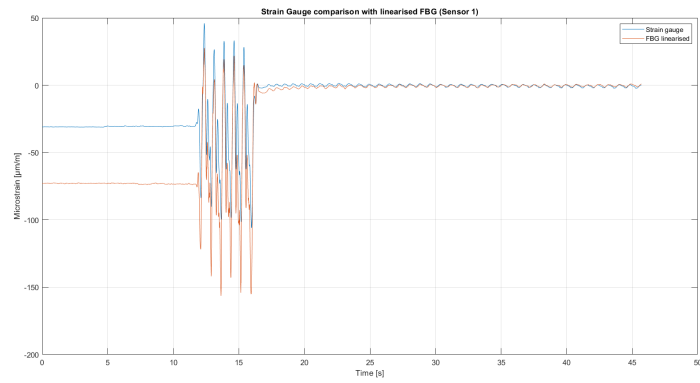
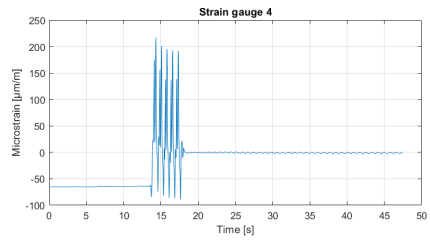
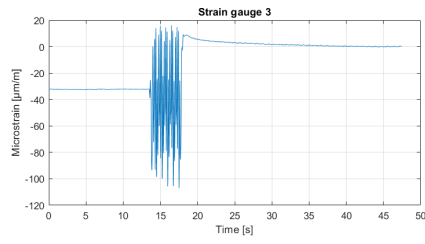
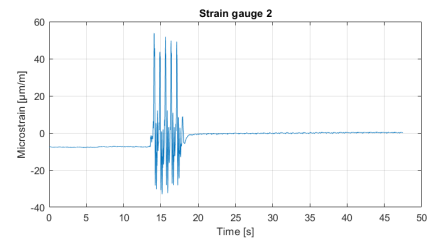
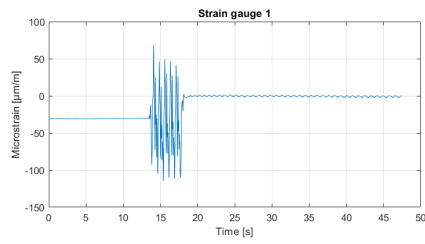
Appendix C

FBG and SG test

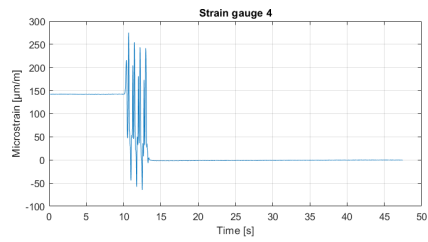
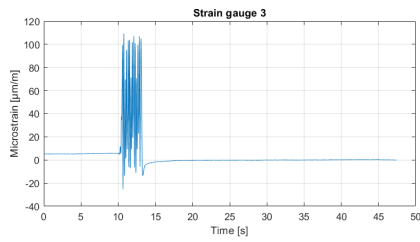
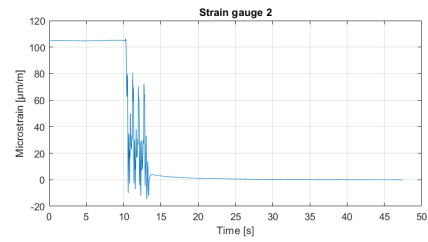
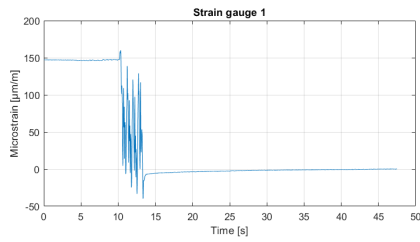
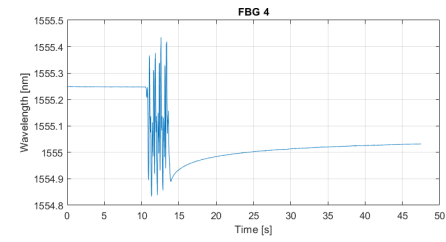
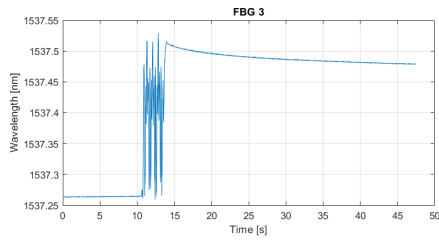
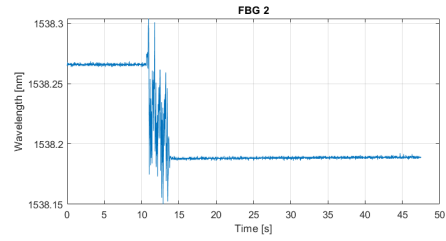
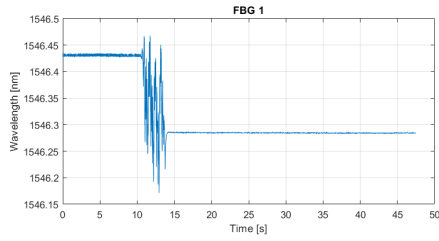
C.1 30 deg intensity step control

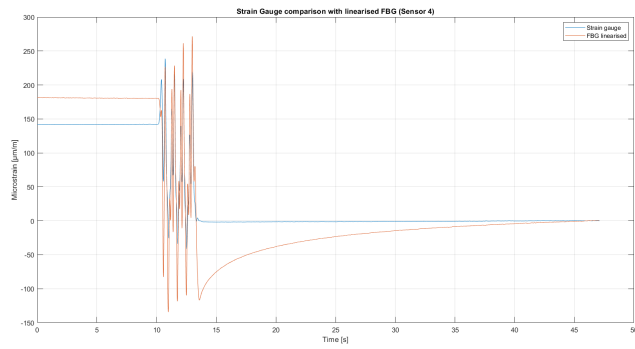
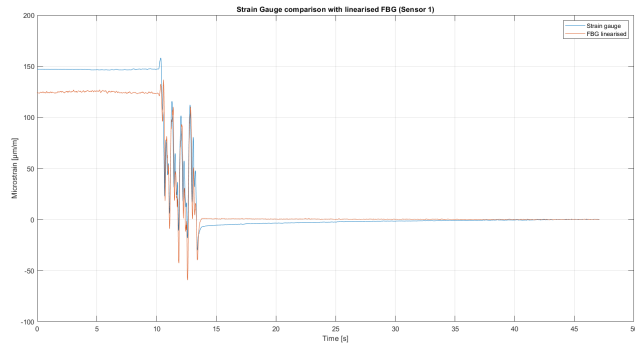


FBG and SG test

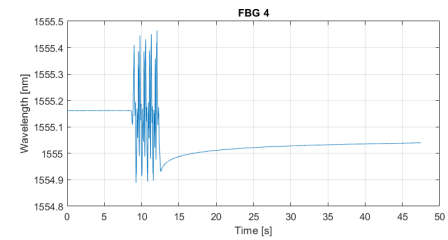
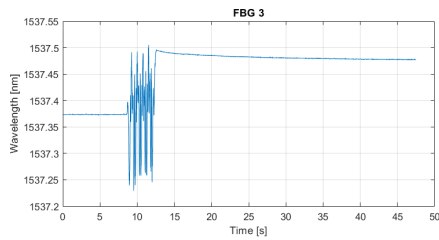
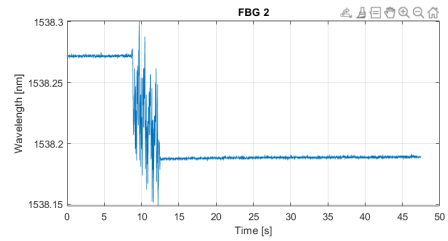
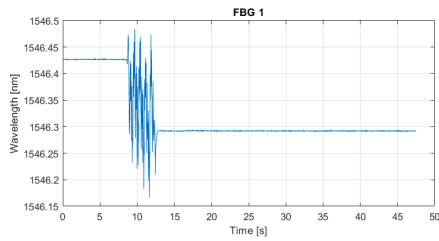


C.2 40 deg intensity step control

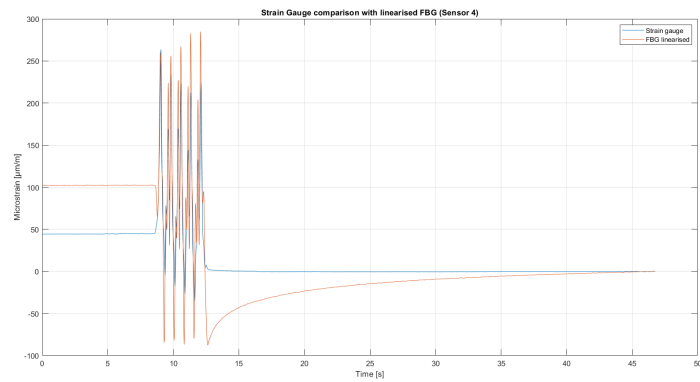
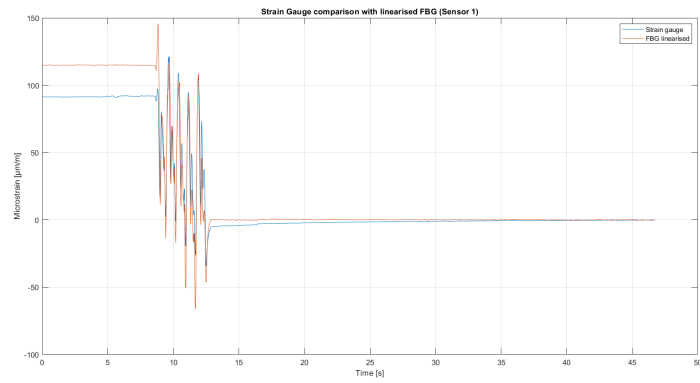
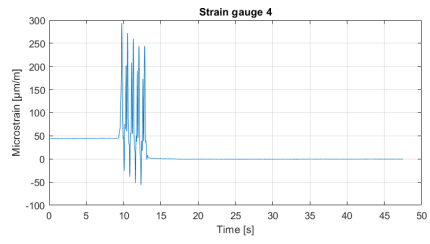
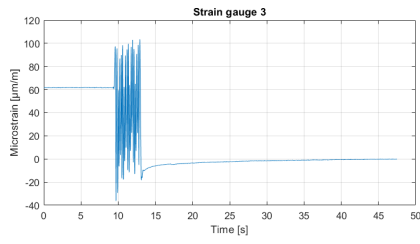
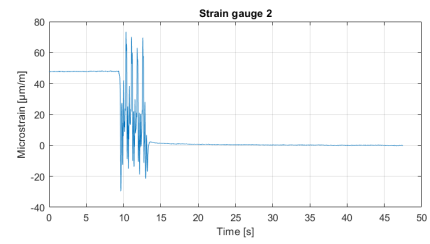
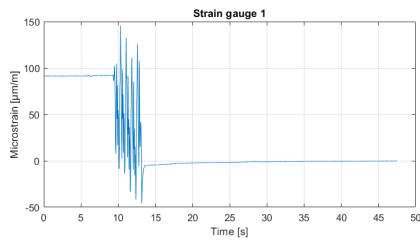




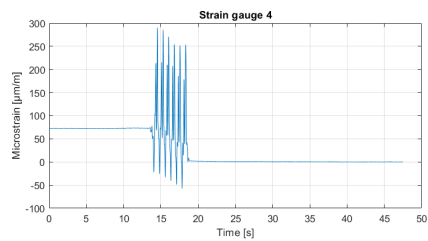
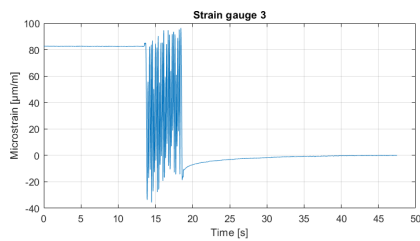
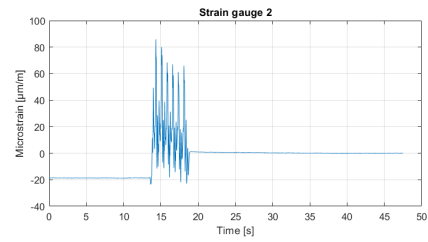
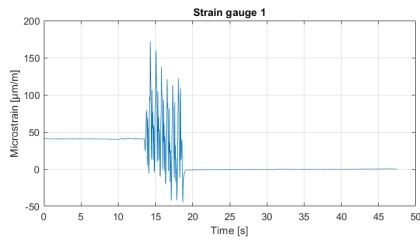
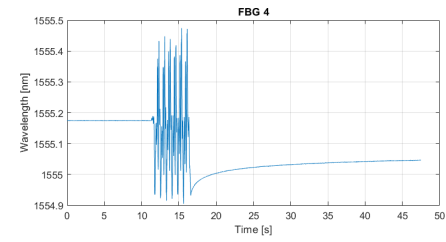
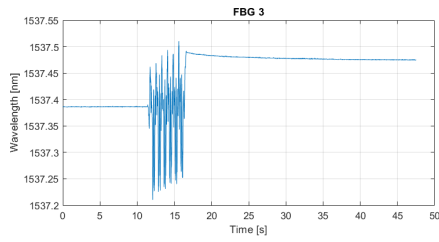
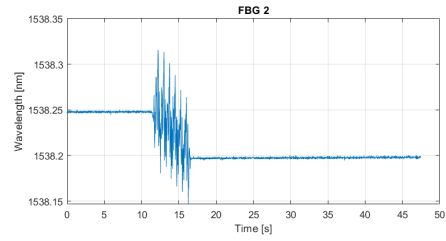
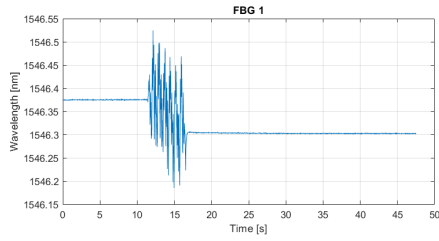
C.3 50 deg intensity step control

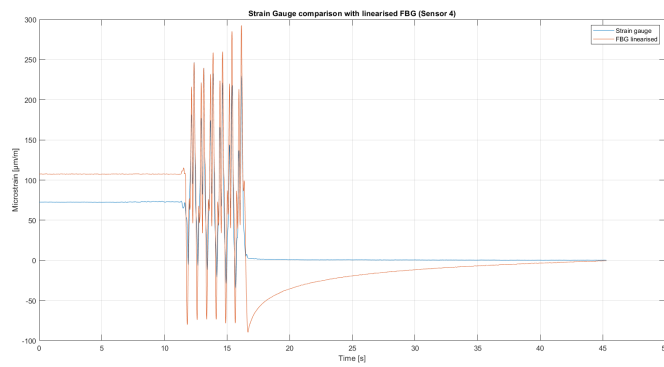
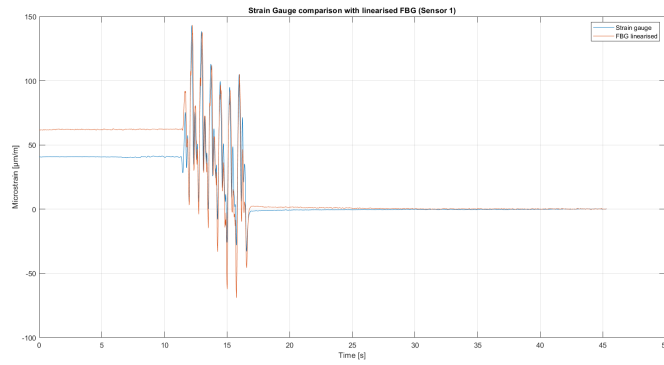


FBG and SG test

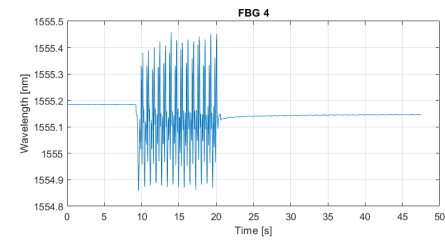
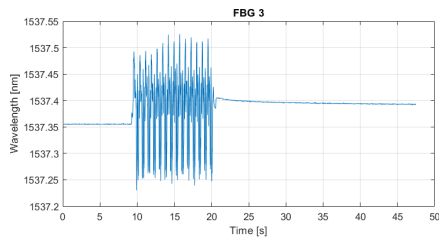
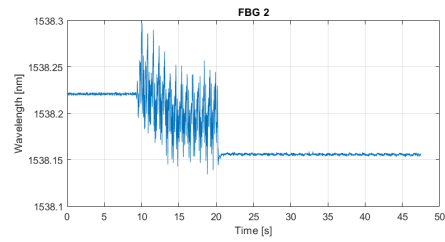
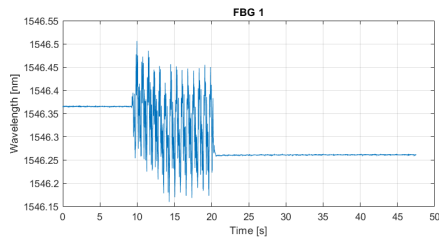


C.4 70 deg intensity step control





C.5 80 deg intensity step control



FBG and SG test

